

Microscopic Swimming in Biological Fluids

Thomas D. Montenegro-Johnson

A thesis submitted to
The University of Birmingham
for the degree of
Doctor of Philosophy

School of Mathematics
The University of Birmingham
January 2013

UNIVERSITY OF
BIRMINGHAM

University of Birmingham Research Archive

e-theses repository

This unpublished thesis/dissertation is copyright of the author and/or third parties. The intellectual property rights of the author or third parties in respect of this work are as defined by The Copyright Designs and Patents Act 1988 or as modified by any successor legislation.

Any use made of information contained in this thesis/dissertation must be in accordance with that legislation and must be properly acknowledged. Further distribution or reproduction in any format is prohibited without the permission of the copyright holder.

Abstract

Fluid interactions are ubiquitous in the natural world; all organisms must find strategies to generate, utilise or resist flow in order to be successful. A process fundamental to all life on earth is reproduction, which in many cases entails the swimming of sperm cells. Cell swimming arises from coupled interactions between physical and biological processes. We will focus on the effects of changing fluid rheology on microscopic swimmers, with a particular application to the study of internal mammalian fertilisation.

To reach the egg, mammalian sperm must navigate the convoluted geometry of the female reproductive tract, actively bending their flagella in order to propel themselves through cervical mucus: a suspension of polymer chains that twist, tangle and align with flow, giving it complex properties. Whilst recent work has examined the effects of fluid viscoelasticity on sperm-like swimmers, relatively less attention has been given to the shear-thinning property. We develop a new finite element technique to simulate free swimmers with prescribed beat kinematics in shear-thinning fluids with nonlinear governing equations. This technique is then applied to three qualitatively different viscous swimmers in order to examine the different phenomena that arise from swimmer interactions with of shear-thinning fluid.

Acknowledgements

I would like to thank my supervisors Prof. John Blake and Dr David Smith, for their guidance, support and insight. Without them, I would not have been inspired to endeavour a career in academia. I am greatly indebted to Dr Daniel Loghin, for advice, expertise and competitive weekly squash matches. I would also like to thank my fellow Ph.D. student Andrew Smith for the work we carried out together for the paper (Smith et al., 2012), which has been summarised in the appendix, along with other work that has been published or submitted. Additionally, I would like to thank Dr Marco Polin and Prof. Ray Goldstein for their supervision of the image analysis work undertaken during my three month placement as a Crighton Fellow in DAMTP, Cambridge. Finally, I would like to thank my wife, Angela, for more than my words can express. The work in this thesis was funded by an EPSRC Doctoral Training Award.

Contents

1	Introduction	11
1.1	Flagellar and ciliary propulsion	11
1.1.1	Internal mechanics of flagellar propulsion	13
1.1.2	Ultrastructure of human sperm flagella	14
1.1.3	The composition of human cervical mucus	16
1.2	The fluid mechanics of microscopic swimming	18
1.2.1	Swimming in Newtonian fluid: Stokes flow	20
1.2.2	Swimming in non-Newtonian fluids: shear dependent viscosity	27
1.3	Studies of microscopic swimming	33
1.3.1	Singularity-based approaches	34
1.3.2	Filament mechanics	38
1.3.3	The Immersed Boundary Method	43
1.3.4	Non-Newtonian micro-swimming studies	46
1.3.5	Overview of this thesis	48
2	Developing the method of femlets to model microscopic swimmers	50
2.1	Finite element method stokeslets: femlets	50
2.1.1	Further details of the numerical implementation	61
2.2	Testing the method of femlets	67
2.2.1	Validating the generalised Stokes flow solver: channel flow	67
2.2.2	The choice of cut-off function	73
2.2.3	Accuracy of the time stepping procedure	83
3	Does shear dependent viscosity aid microscopic swimming?	85
3.1	Introduction	85
3.2	Najafi-Golestani swimmers	86
3.2.1	Results, further analysis and discussion	87
3.2.2	Generalisation to N spheres	92
3.3	Two dimensional squirmers	98
3.3.1	Results and discussion	99
3.4	A two dimensional sperm-like swimmer	107
3.4.1	Results and discussion	109

3.4.2	Effects of changing morphology and kinematics	116
4	Conclusions and Future Work	124
4.1	Summary of methodology	124
4.2	Summary of findings	126
	A Summary of published and submitted work	130
A.1	Published work	130
A.2	Unpublished work	131

List of Figures

1.1	Environmental factors that affect cell motility. (a) Sea urchin sperm demonstrating (top to bottom) planar beating in normal artificial sea water (ASW), helical beating in artificial in ASW with viscosity $1.5 \text{ Pa} \cdot \text{s}$ and planar, meandering beating in ASW of viscosity $4 \text{ Pa} \cdot \text{s}$, showing the sensitivity of the emergent waveform to the surrounding fluid, adapted with permission of the Journal of Experimental Biology from Woolley and Vernon (2001). (b) A cross-section of human fallopian tubing, showing its convoluted geometry, taken by Ed Uthman, MD and printed under a CC BY-SA 2.0 license.	13
1.2	A schematic cross-section of the “9 + 2” axoneme, redrawn from Fawcett (1975). To provide passive stiffening of the structure and maintain its integrity (Nicastro et al., 2006), peripheral nexin links connect each doublet to its two neighbours, and a radial nexin spoke links the doublet to a helical sheath that wraps around the central doublet pair.	15
1.3	A schematic of doublet microtubules in the axoneme. Each doublet consists of a complete microtubule, subfibre A, together with an attached C-shaped section, subfibre B (Fawcett, 1975). The microtubules are constructed from protofilaments of the protein tubulin. Attached to subfibre A are dynein arms that extend toward the neighbouring doublet.	15
1.4	The complex ultrastructure of human spermatozoa, redrawn from (Fawcett, 1975). (a) The lengths of different regions of the cell, highlighting the connecting piece that joins the flagellum to the head. It has been suggested that the connecting piece is responsible for bend initiation and alternation (Vernon and Woolley, 2004) in the flagellum. For each portion of the tail, a cross-section is detailed to its right, showing (b) the midpiece, detailing 9 outer dense fibres and the mitochondrial sheath where energy is produced (c) the principal piece, detailing the outer dense fibres and the fibrous sheath with its two longitudinal columns and (d) the endpiece.	17

1.5	Characteristic Reynolds numbers for a variety biological systems, redrawn from Hosoi and Lauga (2010). The image of human sperm is printed with permission of Dr David Smith, the image of the Apollo butterfly was taken by Oskar Jäckel and is printed under a CC BY-SA 3.0 license and the remaining images are public domain.	19
1.6	A schematic of a homogeneous, unidirectional shear flow in a two dimensional channel of height h . The velocity field $\mathbf{u} = (Uy/h, 0, 0)$ is generated by the upper boundary, which moves with speed U . In this case, the shear rate $\dot{\gamma}$ is given by $\partial\mathbf{u}_1/\partial y = U/h$	21
1.7	Two examples of simple viscous swimmers. (a) Purcell's three-link swimmer, showing the configuration $S_1 \dots S_5$ of its swimming arms relative to its body at 5 key points during its periodic beat cycle and (b) a complete beat cycle of the Najafi-Golestanian swimmer showing the position of the outer spheres relative to the central sphere, the direction in which they move and the direction of swimming.	24
1.8	The flow generated by a singular force, and a demonstration of the 2:1 drag anisotropy that enables flagellar and ciliary propulsion, redrawn from Blake and Sleight (1974).	25
1.9	An approximate singularity representation of the flow field surrounding a human sperm, redrawn from Smith and Blake (Smith and Blake, 2009). The quadrupole representation was suggested after calculation of the force distribution in the tail with slender body theory.	26
1.10	Stress - shear rate graphs of (a) power law fluids with $\mu_0 = 1$ and differing values of the exponent n and (b) a Papanastasiou fluid with $\mu_p = 1$ and $\tau_y = 2$, gradually approaching the Bingham law as the stress growth exponent m increases.	30
1.11	The effective viscosity of Carreau and Papanastasiou fluids as a function of shear rate $\dot{\gamma}$ for $\mu_0 = 1, \mu_\infty = 0.5, m = 0.3, \lambda = 1$ and $n = 0.5$ showing their rheological similarity.	31
1.12	The shear angle ψ as a function of arclength along the flagellum for a swimmer resembling a human sperm.	39
1.13	View of the beat plane of a two dimensional model axoneme, redrawn from Riedel-Kruse et al. (2007), with sliding displacement $\Delta(s)$, internal shear force density $f(s)$ due to the active dyneins (blue), and the passive nexin links (red). There is some sliding allowed at the basal body (grey), represented by springs and dashpots.	40
1.14	A healthy, motile human sperm, swimming in circles through a solution of methylcellulose with a viscosity comparable to the of human cervical mucus. Before the onset of the buckling instability which led to this behaviour, the cell had migrated 2 cm, which is approximately 400 times its body length. Reprinted with permission from Gadélha et al. (2010), figure 1(b).	43

1.15	Schematic of an immersed boundary with Lagrangian points marked overlaying a Cartesian grid on which the fluid equations are to be solved. Redrawn from Mittal and Iaccarino (2005)	44
2.1	An example domain D containing a model human sperm ∂D_{swim} , showing no-slip channel walls ∂D_{dir} and open boundaries ∂D_{neu} . The relationship between the lab frame, (x, y) and the body frame, (x', y') is also shown. Femlets will be distributed along the boundary ∂D_{swim}	52
2.2	(a) The cut-off function g^ϵ , given by equation (2.6) with $\sigma_x = 0.0016$ and $\sigma_y = 0.008$, for a single femlet centered on $\mathbf{x}_k = (0.09, 1)$ and aligned at an angle of $\pi/3$ rad, showing the local frame $(x_k^{\text{loc}}, y_k^{\text{loc}})$. (b) A plot showing the smooth force distribution envelope generated by a sum of such g^ϵ when projected on a finite element mesh, for femlets at the marked locations representing a flagellum.	55
2.3	An example of a two node patch where the left-hand, non-Delaunay triangulation has undergone an edge-flipping routine to create the right-hand Delaunay triangulation.	63
2.4	Two methods of locally refining the mesh corresponding to selecting an edge (left) and an element (right), where the new mesh edges arising from the refinement have been shown in red. We employ element selection in our refinement algorithm.	64
2.5	A linear triangular element with anticlockwise local node numbering.	65
2.6	A linear shape function (red) plotted over a single element (left) together with the associated linear hat function (red) plotted over the patch of neighbouring elements (right).	65
2.7	(a) A quadratic triangle, with anticlockwise node numbering. Note that since we wish to model fluid pressure with linear elements and the velocity with quadratic elements, the first three quadratic nodes coincide with the linear triangle. (b) The Canonical Triangle.	65
2.8	The conditions under which analytic solutions of flow down an infinite channel are derived.	68
2.9	(a) The numerical (red) and analytic (blue) solutions for shear thinning power law flow down a pipe evaluated at 50 evenly spaced points for a mesh with 19702 degrees of freedom and (b) the relative error of the numerical solution. The power law index $n = 0.7$	71
2.10	Approximations to the square wave on the interval $[0, 0.5]$ formed by superposing 10 (red) 20 (green) and 40 (blue) hat functions (a) and Gaussians (b).	76
2.11	(a) Interpolation of the function $y = -x(x - 0.5)$ on the interval $[0, 1]$ by 40 Gaussian (blue, solid) and Hat (red, dashed) femlets and (b) the relative error associated with these interpolations within the region where Gaussian femlets have the interpolation property.	77

2.12	(a) The interpolation of the function $y = -x(x - 0.5)$ if a single femlet is shifted by approximately 8% of the optimal spacing, showing sharp gradients in the interpolation by Hat femlets (red) and little change in the interpolation by Gaussian femlets (blue). (b) The ‘end errors’ associated with interpolating a function that is non-zero at the edge of the femlets, showing errors for the Gaussian propagating further into the interpolation.	77
2.13	(a) Stokes flow in a two dimensional enclosed cavity driven by a regularised moving lid. Arrow lengths and colour denote the fluid speed. (b) Plot showing the x -component of the flow velocity on the slice $x = 0.5$ near the moving lid, showing convergence onto the Dirichlet solution (red) as σ_y is decreased from $\sigma_y = 0.01$ (green) to $\sigma_y = 0.05$ (blue) for Gaussian femlets. Note that the effective radius of the femlets is given by an average in the near-field of the distances at which the femlet velocity is equal to the Dirichlet. Shifting the femlets upwards by the effective radius causes these lines to essentially overlap.	80
2.14	(a) The effective radius of Hat femlets modelling a driven cavity as a function of the power law index n and (b) the speed of fluid driven by a beating filament as given by equation (2.39)	81
2.15	(a) The relative error in the y -component of the fluid velocity along the centreline of the flagellum as a function of arclength, s , for Gaussian (red) and Hat (blue) femlets. (b) The error in the y -component of the velocity on the lower ‘surface’ of the filament, taken at the femlets effective radius, for Gaussian (red) and Hat (blue) femlets, showing good qualitative representation of a finite width filament by femlets, with Gaussian femlets providing greater accuracy.	84
3.1	Simulation results for the smooth time Najafi-Golestani swimmer given by equation (3.1) (a) The global position of the central sphere moving through Newtonian fluid over the course of a single beat cycle, showing the progress as the distance between the two dashed lines. The swimmer’s progress over a single beat cycle as a function of (b) the power law index n with $\mu_0/\mu_\infty = 2$ and $De = 1$, (c) the viscosity ratio μ_0/μ_∞ with $n = 0.5$ and $De = 1$ and (d) the Deborah number De with $n = 0.5$ and $\mu_0/\mu_\infty = 2$. In panels (b,c,d), the case corresponding to Stokes flow has been marked in orange	89
3.2	The shear-thinning results of figure 3.1c plotted on a logarithmic scale, showing a near perfect linear relationship.	90

3.3	(a) The progress of the three-sphere swimmer defined by equation (3.3) as a function of the gradient along the swimmer in the direction of travel, obtained by varying the power law index (red), the viscosity ratio (green) and the Deborah number (blue) independently between the extremal values $n = [0.5, 1]$, $\mu_0/\mu_\infty = [1, 2]$ and $De = [0, 1]$. (b) The decrease in leftward progress during the effective strokes 1 (solid) and 2 (dashed) of the swimmer described in table 3.1 as a function of increasing power law index n and (c) the greater absolute decrease in rightward progress during the recovery strokes 3 (solid) and 4 (dashed). This leads to an overall increase in leftward progress with shear thinning rheology (d).	93
3.4	The viscosity field of fluid surrounding the three-sphere swimmer defined by equation (3.3), with $n = 0.5$, $\mu_0/\mu_\infty = 2$ and $De =$ (a) 0.4, (b) 0.8, and (c) 1.6, showing that although the minimum viscosity decreases with De , the viscosity difference across the swimmer is non-monotonic.	94
3.5	A schematic demonstration of the effects of shear-thinning rheology on the original Najafi-Golestani swimmer over the effective and recovery parts of its stroke, showing the location of thick and thin fluid around it, and the direction of travel.	95
3.6	(a) The locus of the swimming spheres for the generalised Najafi-Golestani swimmer with $N = 5$ over the course of a beat cycle. The streaks show the distance and direction, in the body frame, of sphere travel over one tenth of a beat. (b) For $N = 5$, the global position of the N -sphere swimmer as it moves through Stokes flow over the course of a single beat cycle, showing the progress as the distance between the two dashed lines. (c) The five-sphere swimmer's progress over a single beat cycle as a function of the power law index n with $\mu_0/\mu_\infty = 2$ and $De = 1$, with the case corresponding to Stokes flow marked in orange.	96
3.7	(a) A schematic of the two dimensional treadmilling squirmer, along with (b) a micrograph of a <i>Volvox Carteri</i> colony, showing surface cilia that beat in a coordinated fashion to propel the colony forwards. This cell also shows a number of characteristic 'daughter' colonies within it. Image taken by Prof. Ray Goldstein and reprinted with his permission.	99
3.8	The velocity of the treadmilling squirmer with slip velocity given by equation (3.7) as a function of (a) the viscosity ratio μ_0/μ_∞ with $n = 0.5$ and $Sh = 1$, (b) the shear index Sh with $n = 0.5$ and $\mu_0/\mu_\infty = 2$ and (c) the power-law index n with $\mu_0/\mu_\infty = 2$ and $Sh = 1$. In each panel, the case corresponding to Newtonian fluid is marked in orange.	100
3.9	The effective viscosity of Carreau fluid, normalised to $\mu_0 = 1$, surrounding the treadmilling squirmer for $\mu_0/\mu_\infty = 2$, $n = 0.5$ and $Sh = 0.5$. These parameter values are the extremal values used for the data in figures 3.10 and 3.11. Away from the swimmer surface, contours of equi-viscosity are approximately circular. On the surface, fluid is relatively thicker surrounding the propulsive portions of the swimmer.	101

3.10	The effective viscosity of the fluid envelope surrounding the treadmilling squirmer. (a) Changes in the viscosity field as a function of the radial coordinate r for different values of the power-law index n . The swimmer surface is given by $r = 0.5$. (b) For fixed values of r , the effective viscosity exhibits a near linear dependence upon the power-law index n	102
3.11	The velocity relative to the Newtonian case of the treadmilling squirmer as a function of (a) the effective viscosity on the contour $r = 0.52$ and (b) the rate of decay α of the velocity from the surface of the squirmer relative to the Newtonian case α_{newt} . The velocity has been calculated while varying the three rheological parameters of Carreau flow for $n = 0.5, \mu_0/\mu_\infty \in [1, 2], \text{Sh} = 0.5$ (red), $n = 0.5, \mu_0/\mu_\infty = 2, \text{Sh} \in [0, 0.5]$ (green) and $n \in [0.5, 1], \mu_0/\mu_\infty = 2, \text{Sh} = 0.5$ (blue). This figure demonstrates a striking proportionality between the velocity and the decay rate of the fluid.	104
3.12	(a) The global position of the squirmer with slip velocity (3.10) over the course of a single beat with $\hat{A} = 1$ and $\hat{B} = 0.5$, and (b) the swimmer's progress over a single beat cycle as a function of the power law index n with $\mu_0/\mu_\infty = 2$ and $\text{De} = 1$. In panel (b), the case corresponding to Stokes flow has been marked in orange.	106
3.13	A schematic demonstrating how our swimming parameters are calculated for the trajectory (blue) of a swimmer moving from right to left over one beat-cycle of period T . The progress is the distance between start and end points, VSL is progress divided by the beat period T , ALH is the total side-to-side motion and the instantaneous velocity VCL is the derivative of the arclength along the trajectory s with respect to time.	108
3.14	(a) The flagellar waveform generated by shear angle (3.12) and (b) a micrograph of a human sperm in methylcellulose, a fluid with comparable viscosity to that of cervical mucus.	110
3.15	The impact of varying $\text{De} = \lambda\omega$ on the effective viscosity μ_{eff} of Carreau fluid surrounding a two dimensional sperm-like swimmer at (a) $\text{De} = 0.2$, (b) $\text{De} = 0.8$, (c) $\text{De} = 1.5$ and (d) $\text{De} = 3$ with $\mu_0/\mu_\infty = 2$ and $n = 0.5$. Here, $k = 2.5$ and $A = 0.45\pi$	113
3.16	(a) Trajectories of a two dimensional sperm-like swimmer in Carreau flow for different values of the viscosity ratio μ_0/μ_∞ , showing an increase in progress and a decrease in ALH as μ_0/μ_∞ increases. (b) The force generated by the flagellum on Newtonian fluid at time $t = 0$ (above) and Carreau fluid with $\mu_0/\mu_\infty = 2, n = 0.5$ and $\text{De} = 0.8$, corresponding to figure 3.15b (below). Arrow lengths are normalised to the largest force at the distal end of the flagellum. (c) A time series of the magnitude of the force profile along the flagellum for Stokes flow, showing the progression of the of the travelling bending wave from proximal to distal end and (d) the magnitude of the force profile of the flagella shown in (b), colours matching, showing a redistribution of force to the distal portion of the flagellum in the case of shear-thinning flow. Force is greatest at the tip of the flagellum.	114

3.17	Simulation results for the two dimensional sperm like swimmer in Carreau fluid with shear angle prescribed by equation (3.12) for $k = 2.5$ and $A = 0.45\pi$.(a) The progress and (b) the ALH of a two dimensional sperm-like swimmer as a function of the viscosity ratio μ_0/μ_∞ , for $n = 0.5$ and $De = 1$, (c) \overline{VCL} and (d) the ratio of the forces in the proximal and distal portions of the tail at the instant $t = 0$ as a function of μ_0/μ_∞ and (e) \overline{VCL} and (f) the ratio of the forces in the proximal and distal portions of the tail at the instant $t = 0$ as a function of the Deborah number, De with $\mu_0/\mu_\infty = 2$ and $n = 0.5$. Stokes flow corresponds to the cases $\mu_0/\mu_\infty = 1$ and $De = 1$	115
3.18	(a) The head morphologies listed in table 3.2. Throughout this figure, data are colour matched to correspond with these morphologies, with the case corresponding to the sperm-like swimmer we first considered given by the dashed line. (b) Trajectories of cells with varying head eccentricity through Stokes flow, plotted with equal axis scaling. For $n = 0.5$ and $De = 1$, the effect of varying the viscosity ratio μ_0/μ_∞ on (c) the swimmers' progress, (d) the amplitude of the swimmers' lateral head displacement, (e) the path length of the swimmers' trajectories and (f) the swimmers' path straightness.	118
3.19	(a) Trajectories of the cells with head morphologies given in table 3.3, swimming in Stokes flow with $n = 0.5$, $\mu_0/\mu_\infty = 4$ and $De = 1$. For $n = 0.5$ and $De = 1$, the effect of varying the viscosity ratio μ_0/μ_∞ on (b) the swimmers' progress, (c) the amplitude of the swimmers' lateral head displacement, (d) the path length of the swimmers' trajectories and (e) the swimmers' path straightness. The case corresponding to the sperm-like swimmer we first considered is given by the dashed line.	120
3.20	(a) Colour matched trajectories of the cells with waveforms shown in table 3.4, swimming in Carreau flow with $n = 0.5$, $\mu_0/\mu_\infty = 4$ and $De = 1$. For $n = 0.5$ and $De = 1$, the effect of varying the viscosity ratio μ_0/μ_∞ on (b) the swimmers' progress, (c) the amplitude of the swimmers' lateral head displacement, (d) the path length of the swimmers' trajectories and (e) the swimmers' path straightness. The case corresponding to the sperm-like swimmer we first considered is given by the dashed line.	123

List of Tables

2.1	The error in calculated flow and pressure solutions for Papanastasiou flow down a channel as a function of the number of degrees of freedom solved for and the difference between solutions of Carreau flow down a channel for successive refinements of the mesh, where $h = 1$ corresponds to the difference between the solution for 1268 D.o.F. and 840 D.o.F., $h = 2$ the difference between 2270 D.o.F. and 1268 D.o.F. etc.	72
2.2	(a) Errors in the no-slip condition on the upper wall of a regularised driven cavity when that wall is modelled as a line distribution of varying numbers of Gaussian and Hat femlets with $\sigma_y = 0.01$. (b) Errors along the line $x = 0.5$ in the calculated flow in a regularised driven cavity where the upper wall is modelled as a line distribution of 40 femlets of increasing sharpness.	80
3.1	The positions of the three spheres of the original Najafi-Golestanian swimmers over each portion of its beat cycle.	95
3.2	Elliptical head morphologies of constant area but different eccentricity, corresponding to the data in figure 3.18. The case corresponding to the sperm-like swimmer we first considered is second from the top. These morphologies from top to bottom correspond with dark to light plots.	116
3.3	Elliptical head morphologies of constant eccentricity, but different area, corresponding to the data in figure 3.19. The case corresponding to the sperm-like swimmer we first considered is given by the middle entry. These morphologies, from top to bottom correspond with dark to light plots.	119
3.4	The wavenumbers and their corresponding beat patterns used to examine the robustness of the effects of shear-thinning to cell kinematics. Data in figure 3.20 are colour matched to their corresponding waveform, with the sperm-like swimmer we first considered, $k = 2.5$, here marked in red, given by the dashed lines. The waveforms are shown in a time-lapse fashion over the same period.	121

Chapter 1

Introduction

1.1 Flagellar and ciliary propulsion

Microscopic swimmers pervade the natural world, from bacteria and algae to the sperm cells of vertebrates, and the study of their swimming is pertinent to numerous problems in medicine and industry, for example in reproductive medicine and biofuel production. Microscale fluid propulsion is usually achieved in nature through the beating of cilia and flagella: slender, hair-like organelles that perform a range of functions from locomotion and food gathering to behavioral responses (Dentler, 1987).

Cilia and flagella play a vital rôle in many stages of development (Fauci and Dillon, 2006). In humans, flagella propel sperm cells during reproduction, allowing sperm and egg to meet. Cilia then transfer the fertilised embryo from the ampulla to the uterus. In the early stages of embryonic development, cilia are responsible for the production of a directional fluid flow which breaks left-right symmetry in vertebrates (Nonaka et al., 1998), and mucociliary clearance in the lung removes microorganisms and solid particles from the airway (Sleigh et al., 1988).

Sperm swim by beating a single flagellum which pushes the cell body, and so are often referred to as monoflagellate pushers. The flagellum coordinates the generation of active bending moments along its length, producing a bending wave that propagates from neck to tip. This

pushes the cell through the fluid towards the egg.

For mammalian sperm, this fluid is mucus - a highly viscous polymer suspension with complicated flow properties that affect swimming. To reach the egg, they must navigate the convoluted geometry of the fallopian tubes (figure 1.1b). The flagellar waveform emerges from the interaction between the active elastic flagellum, convoluted geometry and rheologically complex fluid. This system is highly coupled; changing any aspect of the physics, such as the fluid viscosity, can result in sharp nonlinear transitions of the waveform as shown in figure 1.1a. Thus, biologically realistic fluid mechanics modelling is vital to develop accurate models of internal fertilisation.

In this thesis we will develop computational techniques to simulate microscopic swimming in rheologically complex fluids, allowing more accurate calculation of the energetics and force generation in the flagellum during fertilisation. We will also discuss the physical mechanisms underlying rheological interactions with viscous swimmers.

Birth rates in developed countries are falling, with around 1 in 6 couples being subfertile. Sperm factors are present in around half of these cases (Human Fertilisation and Embryology Authority, 2011), and better understanding of the mechanics of sperm swimming might inform the development of novel diagnostic tools allowing clinical differentiation between 'good' and 'bad' cells. For instance, it might aid in the design of microfluidic sorting devices, which may improve IVF by, for example, enabling cells from men with low motile sperm counts to be more highly concentrated (Denissenko et al., 2012). Detailed mechanical modelling is also vital for understanding the energetic basis for motility (Ford, 2006), and the modulation of flagellar beating by hormones and potential new drugs (Gaffney et al., 2011). As a potential application of the work in this thesis, high-speed images of live cells from a particular patient might be used to prescribe the flagellar waveform, and information about flagellar mechanics extracted.

However, before introducing the fluid mechanics modelling which will form the focus of this work, we will first outline the complex internal structure of human sperm flagella. This

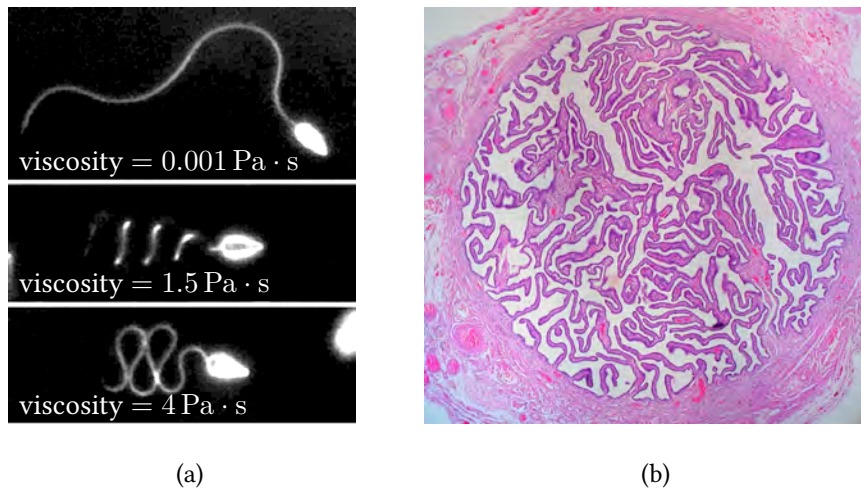


Figure 1.1: Environmental factors that affect cell motility. (a) Sea urchin sperm demonstrating (top to bottom) planar beating in normal artificial sea water (ASW), helical beating in artificial ASW with viscosity $1.5 \text{ Pa} \cdot \text{s}$ and planar, meandering beating in ASW of viscosity $4 \text{ Pa} \cdot \text{s}$, showing the sensitivity of the emergent waveform to the surrounding fluid, adapted with permission of the Journal of Experimental Biology from Woolley and Vernon (2001). (b) A cross-section of human fallopian tubing, showing its convoluted geometry, taken by Ed Uthman, MD and printed under a CC BY-SA 2.0 license.

structure enables active bending of the flagellum, which in turn gives rise to cell swimming. We will then give a brief description of the composition of human cervical mucus.

1.1.1 Internal mechanics of flagellar propulsion

In eukaryotic cells, cilia and flagella induce active bending along their length (Machin, 1958). This was hypothesised as early as 1835 by Sharpey, who argued that contractile material distributed throughout cilia was responsible for generating the observed beating. Later, Ballowitz (1888) was able to observe that sperm flagella contain an internal structure of around 9 – 11 microtubules, continuous along the flagellum length (Gibbons, 1981). However it was not until the advent of electron microscopy that the existence of this internal structure, the axoneme, was confirmed (Manton and Clarke, 1952; Fawcett, 1954; Afzelius, 1959).

The axoneme is remarkably phylogenetically conserved (Fawcett, 1975). It is almost iden-

tical, with rare exceptions (Phillips, 1970), in all species that possess it; from human lung cilia and sperm to unicellular green algae and Protozoa such as *Paramecium*. The axoneme, shown in figure 1.2, comprises 9 inextensible outer microtubule doublets, detailed in figure 1.3, and passive linking elements which stiffen the assembly. In contrast to the contraction hypothesis of Sharpey (1835), it is now thought that the combination of relative, localised microtubule sliding, inextensibility and the restraining effects of linking structures, generates bending. This is the ‘sliding filament theory’ proposed by Satir (1965). For human sperm, as with the majority of motile cilia, a central pair of microtubules runs along the length of the axoneme. This configuration is referred to as the “9 + 2” axoneme.

The relative sliding of microtubule doublets (figure 1.3) is driven by dynein arms which extend, bind and detach from the neighbouring doublet. The dynein arms are molecular motors, converting chemical energy into mechanical movement through ATP-ase activity, though the mechanisms controlling the coordinated activation of these dyneins are still unknown (Lindemann, 2009).

1.1.2 Ultrastructure of human sperm flagella

Human sperm have had to evolve to meet the challenges associated with internal fertilisation, in particular the need to swim through cervical mucus which can be around 100 times more viscous than water (Gaffney et al., 2011). In order to cope with these challenges, human sperm have evolved a complicated ultrastructure surrounding the axoneme, as shown in figure 1.4. An important difference between marine spermatozoa (figure 1.1a), which swim through sea water, and human species are accessory passive stiffening elements. These take the form of 9 outer dense fibres attached to the doublet microtubules in the axoneme, and a fibrous sheath comprised of two longitudinal columns in the same plane as the central pair. These passive structures are not found in marine sperm whose locomotion, in contrast with human sperm,

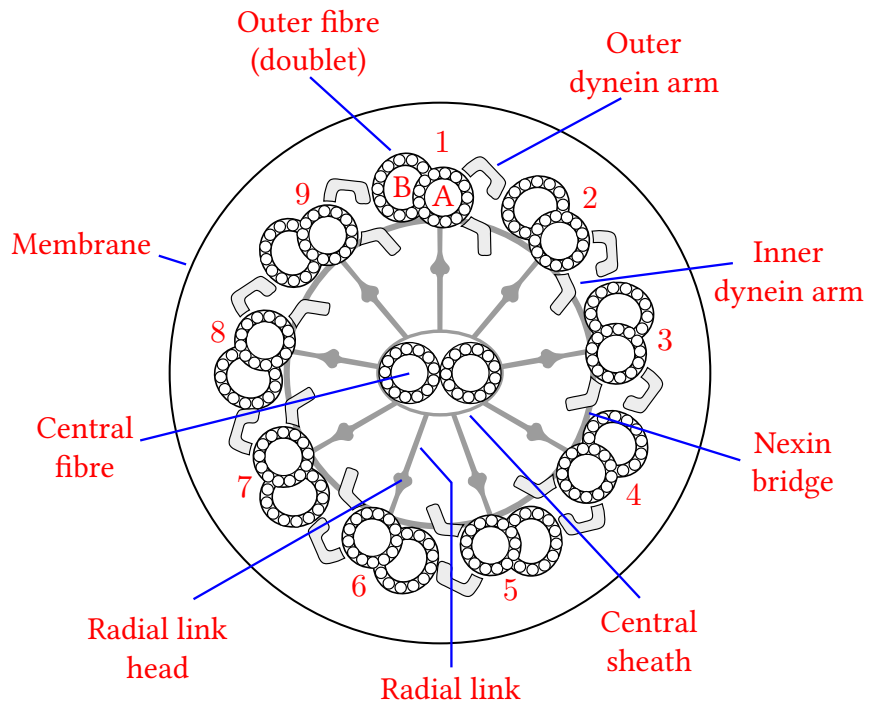


Figure 1.2: A schematic cross-section of the “9 + 2” axoneme, redrawn from Fawcett (1975). To provide passive stiffening of the structure and maintain its integrity (Nicastro et al., 2006), peripheral nexin links connect each doublet to its two neighbours, and a radial nexin spoke links the doublet to a helical sheath that wraps around the central doublet pair.

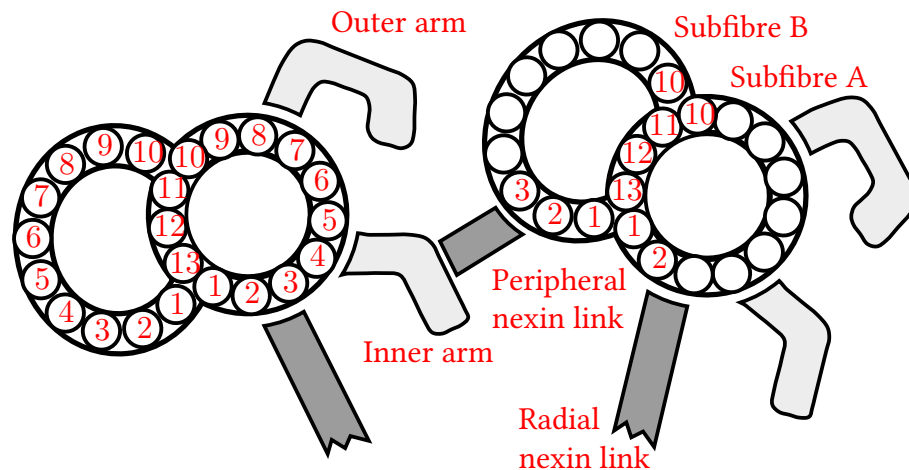


Figure 1.3: A schematic of doublet microtubules in the axoneme. Each doublet consists of a complete microtubule, subfibre A, together with an attached C-shaped section, subfibre B (Fawcett, 1975). The microtubules are constructed from proto-filaments of the protein tubulin. Attached to subfibre A are dynein arms that extend toward the neighbouring doublet.

is severely inhibited by highly viscous fluids (Brokaw, 1966; Woolley and Vernon, 2001).

1.1.3 The composition of human cervical mucus

Human cervical mucus is a suspension of polymer chains, called mucins, entangled in a fibre mesh (Lai et al., 2009). At the scale of the interfibre spacing, roughly 100 nm (Olmsted et al., 2001), a particle diffusing in mucus would experience an environment similar to water. As particles increase in size, the drag they experience increases as they are hindered by the fibre mesh, which is apparent for particles of diameter 1 μm or greater (Lai et al., 2009). For human sperm, which are around 50 μm in length, the entangled polymer chains present a significant obstacle to progression. Cervical mucus and human sperm have had to coevolve so that sperm can penetrate this fibre mesh, while foreign pathogens such as *Treponema pallidum*, the spirochete bacterium that causes syphilis, cannot. The ultrastructure of human sperm allows flagella waveforms that enable this. In women with bacterial vaginosis, cervical mucus is thinned significantly, which is a possible cause for increased risk of HIV and Gonorrhoea (Olmsted et al., 2003).

While some research that considers the reaction of individual mucin fibres to a free swimmer is beginning to be undertaken, we will take an approach where the heterogeneity of the fibre mesh has been averaged into bulk rheological properties, motivated by the small scale of mucus interfibre spacing relative to the length of sperm. The bulk properties that characterise mucus are its viscosity, a measure of its resistance to flow, and elasticity, its readiness to return to an undeformed state following a deformation. As such, mucus is often referred to as a ‘viscoelastic’ fluid.

The effects of fluid elasticity on microscopic swimmers has received much recent study (Lauga, 2007b; Fu et al., 2009; Teran et al., 2010; Pak and Lauga, 2011; Shen and Arratia, 2011; Zhu et al., 2012). However, another property of mucus is shear-thinning (Lai et al., 2007), arising from the tendency of the entangled polymers to be teased out and aligned with flow.

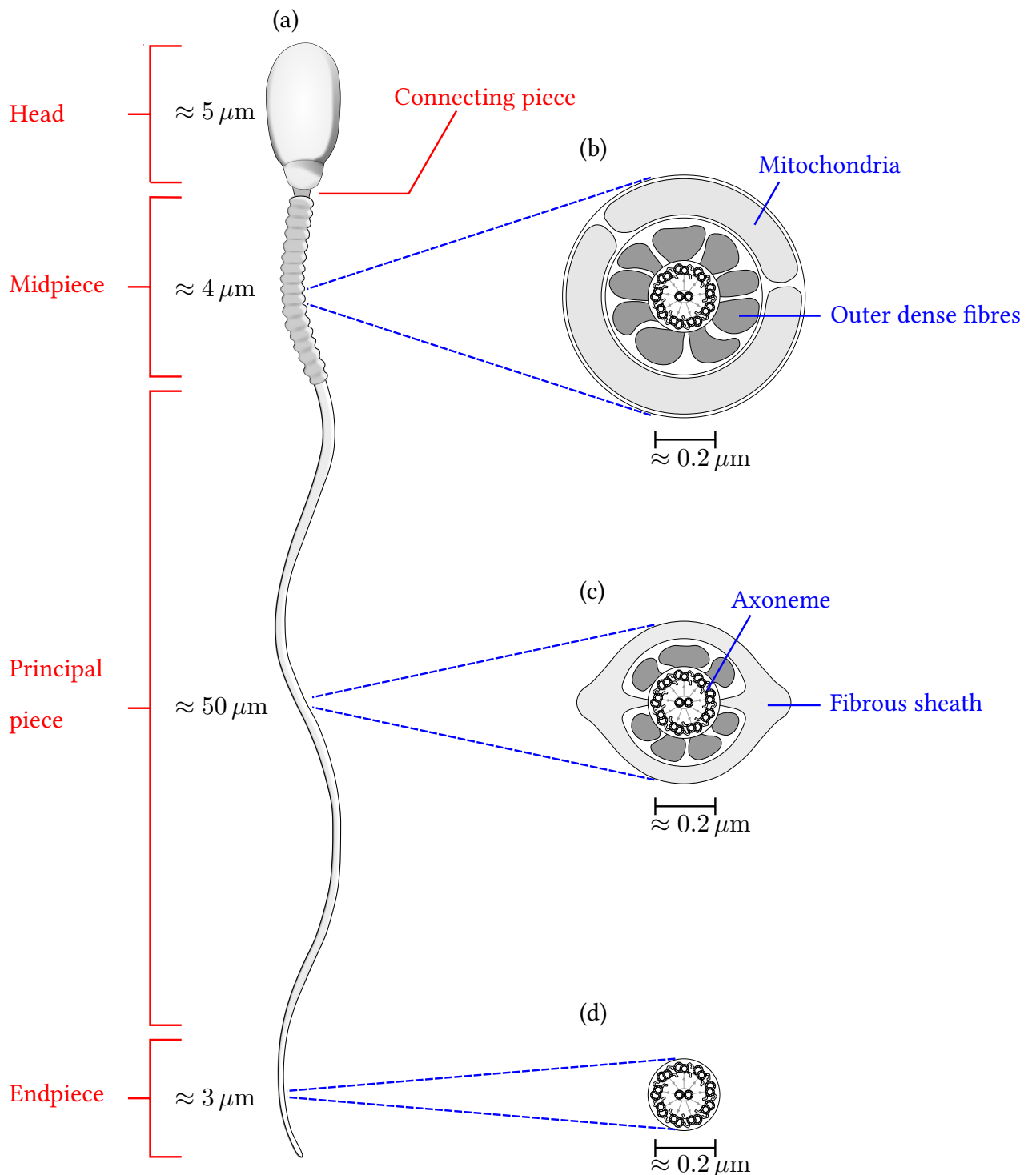


Figure 1.4: The complex ultrastructure of human spermatozoa, redrawn from (Fawcett, 1975). (a) The lengths of different regions of the cell, highlighting the connecting piece that joins the flagellum to the head. It has been suggested that the connecting piece is responsible for bend initiation and alternation (Vernon and Woolley, 2004) in the flagellum. For each portion of the tail, a cross-section is detailed to its right, showing (b) the midpiece, detailing 9 outer dense fibres and the mitochondrial sheath where energy is produced (c) the principal piece, detailing the outer dense fibres and the fibrous sheath with its two longitudinal columns and (d) the endpiece.

Relatively less study (Balmforth et al., 2010; Shen et al., 2012) has been given to understanding the the impact of shear dependent viscosity on microscopic swimming. It is on this property of cervical mucus that we will focus. A discussion of the modelling of these fluids, and the equations governing their dynamics, now follows.

1.2 The fluid mechanics of microscopic swimming

The motion of any continuous medium (Batchelor, 1967), fluid or solid, is governed by the Cauchy equations

$$\rho \frac{\mathcal{D}\mathbf{u}}{\mathcal{D}t} = \nabla \cdot \boldsymbol{\sigma} + \mathbf{F}, \quad (1.1a)$$

$$\frac{\partial \rho}{\partial t} + \nabla \cdot (\rho \mathbf{u}) = 0, \quad (1.1b)$$

where the material derivative is given by

$$\frac{\mathcal{D}\mathbf{u}}{\mathcal{D}t} = \frac{\partial \mathbf{u}}{\partial t} + (\mathbf{u} \cdot \nabla) \mathbf{u}. \quad (1.2)$$

Here, \mathbf{F} is the body force acting on the fluid, such as gravity, ρ is the fluid density and \mathbf{u} is the fluid velocity in a fixed frame of reference. The stress tensor $\boldsymbol{\sigma}$ incorporates the forces acting over the surface of an arbitrary parcel of fluid, such as pressure and internal friction. Its form is given by the constitutive equation of the type of fluid being modelled.

Equation (1.1a) represents conservation of momentum and arises as a result of applying Newton's Second Law to a small arbitrary parcel of fluid, while equation (1.1b) corresponds to conservation of mass. Throughout this work we will consider only fluids for which the density is constant throughout the problem domain, so that (1.1b) reduces to

$$\nabla \cdot \mathbf{u} = 0. \quad (1.3)$$

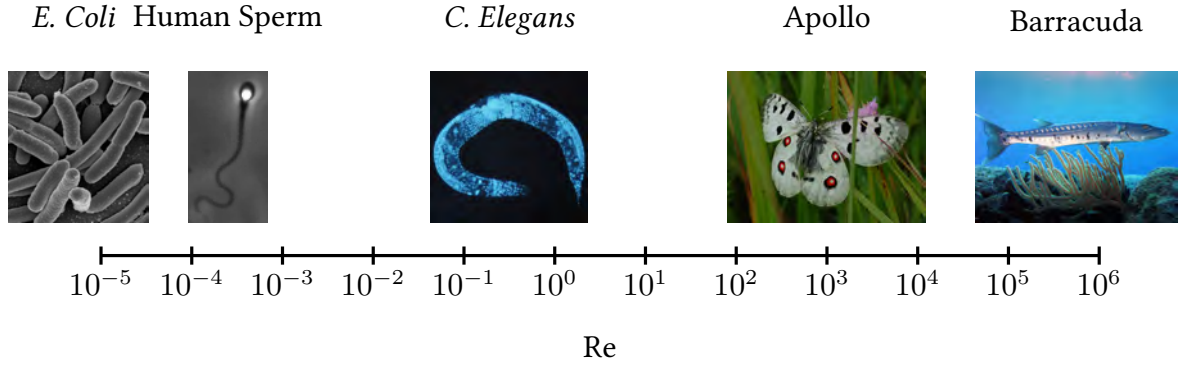


Figure 1.5: Characteristic Reynolds numbers for a variety biological systems, redrawn from Hosoi and Lauga (2010). The image of human sperm is printed with permission of Dr David Smith, the image of the Apollo butterfly was taken by Oskar Jäckel and is printed under a CC BY-SA 3.0 license and the remaining images are public domain.

Upon consideration of the relative importance of terms in (1.1a), we may non-dimensionalise the momentum equation to give

$$\text{Re} \cdot \frac{D\mathbf{u}}{Dt} = \nabla \cdot \boldsymbol{\sigma} + \mathbf{F}, \quad \text{Re} = \frac{\rho U^2 L^2}{\mu UL} = \frac{\text{inertial force}}{\text{viscous force}}, \quad (1.4)$$

where μ is the fluid viscosity, U is the typical velocity of the flow and L is a typical length-scale, given in our case by some intrinsic feature of the swimmer, such as the length of the flagellum. The dimensionless Reynolds number, Re , is a measure of the relative importance of inertial and viscous forces. The Reynolds numbers of a variety of swimmers and flyers are shown in figure 1.5.

For the swimming problems that we will consider, typical length-scales L are $\mathcal{O}(10^{-5} - 10^{-4})$ m and velocities U are $\mathcal{O}(10^{-5} - 10^{-4})$ m \cdot s $^{-1}$. Fluid densities ρ are $\mathcal{O}(10^3)$ kg \cdot m $^{-3}$ and fluid viscosity is μ is $\mathcal{O}(10^{-3})$ Pa \cdot s or greater. Thus, the Reynolds number (1.4) is no higher than $\text{Re} = 10^{-2} \ll 1$ for these swimming problems. Thus, viscous forces dominate inertia. Indeed, if a bacterium, moving at $30 \mu\text{m} \cdot \text{s}^{-1}$ through an idealised fluid with no thermal fluctuations, should stop beating its flagellum, it would theoretically stop within a distance of around 0.1 \AA (Purcell, 1977), a tenth the diameter of a hydrogen atom.

Since the swimmers we will consider are neutrally buoyant, the only body force acting on the flow is gravity, which may be neglected at microscopic length-scales. Thus, an accurate representation of the fluid flow is given by simplifying equations (1.1) via equations (1.3) and (1.4) by setting $\text{Re} = 0$, to the inertialess Cauchy equations,

$$\nabla \cdot \boldsymbol{\sigma} + \mathbf{F} = 0, \quad \nabla \cdot \mathbf{u} = 0. \quad (1.5)$$

The precise form of $\boldsymbol{\sigma}$, the relationship between fluid stress and strain rate, depends on the rheological properties of the fluid. For the fluids we will consider, $\boldsymbol{\sigma}$ is dependent upon the fluid strain rate $\boldsymbol{\varepsilon}(\mathbf{u}) = \frac{1}{2} (\nabla \mathbf{u} + (\nabla \mathbf{u})^T)$, the symmetric part of the velocity gradient tensor $\nabla \mathbf{u}$. For the simple case of shear flow, shown in figure 1.6, the strain rate is given by

$$\boldsymbol{\varepsilon}(\mathbf{u}) = \frac{1}{2} (\nabla \mathbf{u} + (\nabla \mathbf{u})^T) = \frac{1}{2} \begin{pmatrix} 0 & \dot{\gamma} \\ \dot{\gamma} & 0 \end{pmatrix}. \quad (1.6)$$

This motivates the definition of a scalar shear rate as the second invariant of the strain rate tensor $\dot{\gamma} = (2\varepsilon_{ij}(\mathbf{u})\varepsilon_{ij}(\mathbf{u}))^{1/2}$. We will consider swimmers in fluids for which the viscosity is dependent upon shear rate $\dot{\gamma}$, however we will first review salient aspects of the simpler Newtonian theory, which is an appropriate model for water.

1.2.1 Swimming in Newtonian fluid: Stokes flow

For Newtonian fluids stress is proportional to strain rate, so that the fluid viscosity depends only on temperature which is assumed to be constant throughout this study. In such cases,

$$\boldsymbol{\sigma} = -p\mathbf{I} + 2\mu\boldsymbol{\varepsilon}(\mathbf{u}), \quad (1.7)$$

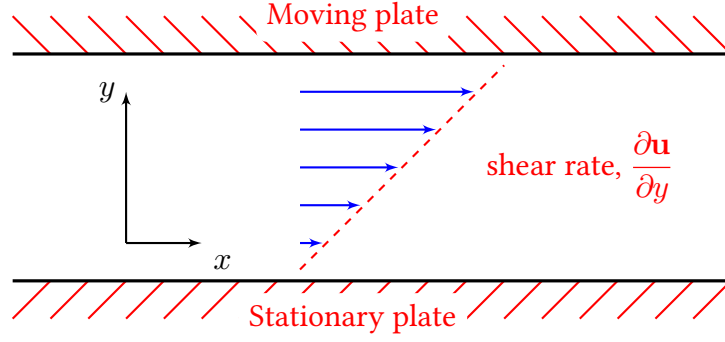


Figure 1.6: A schematic of a homogeneous, unidirectional shear flow in a two dimensional channel of height h . The velocity field $\mathbf{u} = (Uy/h, 0, 0)$ is generated by the upper boundary, which moves with speed U . In this case, the shear rate $\dot{\gamma}$ is given by $\partial \mathbf{u}_1 / \partial y = U/h$.

for pressure p and identity tensor \mathbf{I} . The constant of proportionality between stress and strain rate is the fluid dynamic viscosity, μ . Substitution of the stress (1.7) into the inertialess Cauchy equations (1.5) yields the Stokes flow equations.

$$\mu \nabla^2 \mathbf{u} - \nabla p + \mathbf{F} = 0, \quad \nabla \cdot \mathbf{u} = 0. \quad (1.8)$$

Note that the Stokes flow equations are linear, so that if $(\mathbf{u}, p_u), (\mathbf{v}, p_v)$ are solutions, then

$$\nabla^2(\mathbf{u} + \mathbf{v}) - \nabla(p_u + p_v) = (\nabla^2 \mathbf{u} - \nabla p_u) + (\nabla^2 \mathbf{v} - \nabla p_v) = 0, \quad (1.9a)$$

$$\nabla \cdot (\mathbf{u} + \mathbf{v}) = \nabla \cdot \mathbf{u} + \nabla \cdot \mathbf{v} = 0, \quad (1.9b)$$

and thus $(\mathbf{u} + \mathbf{v}, p_u + p_v)$ is also a solution. This means that fluid flow governed by the Stokes flow equations may be constructed by superposition, which underlies the majority of techniques that have been developed to model viscous swimming in Newtonian fluids (section 1.3.1).

Since there is no time dependence in the Stokes flow equations (1.8), the flow field is determined instantaneously by the boundary conditions. Thus, if the motion of the boundary were to be reversed, or time played backwards, the Stokes flow equations would be satis-

fied by the equal and opposite flow to the forwards-time solution. This reversibility places severe restrictions on the possible motion that may give rise to propulsion in Stokes flow. Any periodic motion must be irreversible in order to generate a net flow. Thus many familiar swimming techniques, such as single-oar sculling and the clapping of a clam shell, that are indistinguishable from their time reversals, generate no net displacement in Stokes flow. This was demonstrated in Taylor’s film on low-Reynolds number flow (Taylor, 1967), where it was also shown that a body driven by a rotating helical filament could swim in a viscous environment, and formalised by Purcell as the “Scallop Theorem” in his famous lecture (Purcell, 1977). The theorem, proved formally by Ishimoto and Yamada (2011), states that a body in Stokes flow cannot swim with a reciprocal stroke. A natural corollary is that an animal with a single hinge, such as a scallop, cannot generate net displacement over the course of a beat in Stokes flow, though this is possible in Newtonian flows of arbitrarily small Reynolds number (Lauga, 2007a). The Scallop theorem is also only valid for isolated swimmers in infinite domains of Newtonian fluid, and violating any one of these conditions can lead to its breakdown (Lauga, 2011).

Purcell’s example of the simplest possible swimmer able to propel itself in Stokes flow is known as the three-linked swimmer, shown in figure 1.7a. It comprises a central arm linked at either end to two hinged swimming arms which move between the configurations $S_1 \dots S_5$. The three-linked swimmer generates net displacement through hydrodynamic interactions between the swimming arms, though its average speed and direction depend on both the angular amplitude of the swimming strokes and the relative length of the arms (Becker et al., 2003).

An arguably simpler viscous swimmer was proposed by Najafi and Golestanian (2004). It comprises two outer spheres which move relative to a central sphere with a non-reciprocal motion, as shown in figure 1.7b. The mechanism underlying the Najafi-Golestanian swimmer is as follows: one of the outer spheres will move at any given time. By force balance, leftward relative motion of an outer sphere results in rightward motion of the remaining spheres

through the fluid, and vice versa. The distance that the remaining spheres move in the fluid depends on the drag of the remaining two spheres.

The beat is divided into two effective and two recovery strokes, where the swimmer travels along and opposite the direction of net progress respectively. Relative leftward motion of an outer sphere occurs while the other spheres are far apart; relative rightward motion of an outer sphere occurs while the other spheres are close together. Hydrodynamic interaction results in the drag of the other spheres being reduced when they are close together. Therefore the drag of the remaining spheres is less during relative rightward motion of the active sphere, and so the beat cycle is slightly more effective in moving the swimmer to the left than the right.

The fundamental singularity

Since the Stokes flow equations are linear, it is possible to superpose fundamental solutions in order to generate more complex flows. Consider an infinite fluid obeying the Stokes flow equations (1.8), driven by a concentrated force per unit volume $\mathbf{F} = \mathbf{f}\delta(\mathbf{x} - \mathbf{y})$ of magnitude and direction \mathbf{f} , where δ is the three dimensional Dirac delta distribution centered at \mathbf{y} . The velocity solution corresponding to this fundamental singularity is given by

$$u_i(\mathbf{x}) = \frac{1}{8\pi\mu} \left(\frac{\delta_{ij}}{r} + \frac{r_i r_j}{r^3} \right) f_j(\mathbf{y}) =: S_{ij}(\mathbf{x}, \mathbf{y}) f_j(\mathbf{y}), \quad i, j = 1, 2, 3, \quad (1.10)$$

where $r_i = x_i - y_i$, $r^2 = r_1^2 + r_2^2 + r_3^2$ and $S_{ij}(\mathbf{x}, \mathbf{y})$ is known as the stokeslet.

The anisotropic term $r_i r_j / r^3$ within the stokeslet has an important consequence for the fluid mechanics of cilia and flagella. As shown in figure 1.8, the flow velocity at a distance α from a singular force is twice as large at points in line with the force than at those perpendicular to it. A slender cylinder, such as a cilium or flagellum, moving through a fluid may be approximated by a line distribution of singular driving forces, as shown in figure 1.8. The corresponding velocity field is then approximated by a sum of stokeslet solutions, so that the

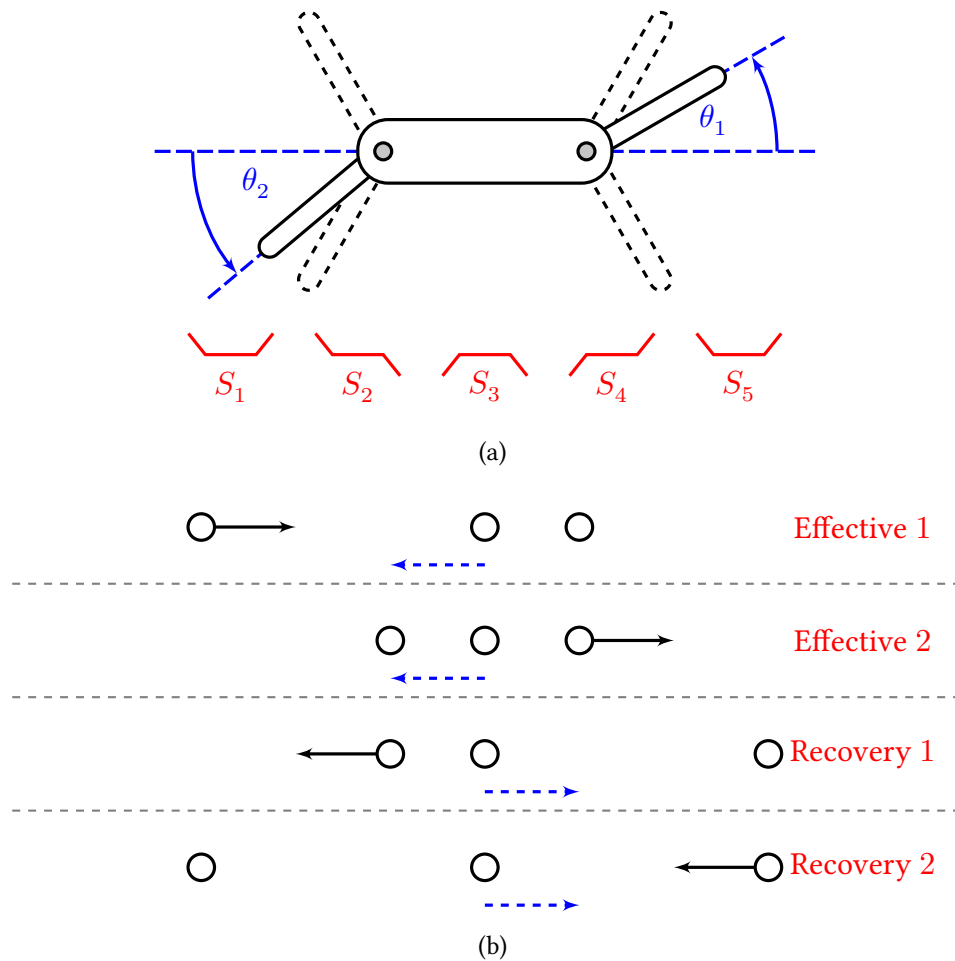


Figure 1.7: Two examples of simple viscous swimmers. (a) Purcell's three-link swimmer, showing the configuration $S_1 \dots S_5$ of its swimming arms relative to its body at 5 key points during its periodic beat cycle and (b) a complete beat cycle of the Najafi-Golestanian swimmer showing the position of the outer spheres relative to the central sphere, the direction in which they move and the direction of swimming.

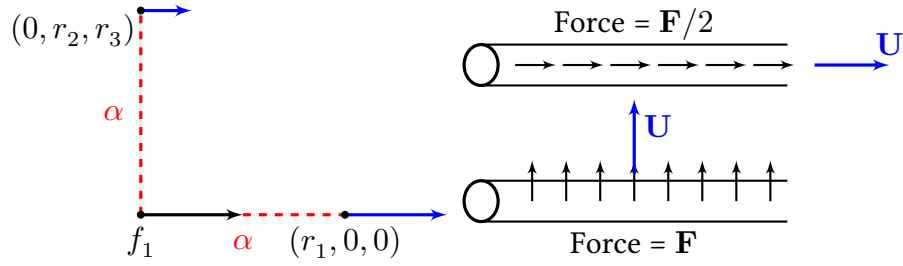


Figure 1.8: The flow generated by a singular force, and a demonstration of the 2:1 drag anisotropy that enables flagellar and ciliary propulsion, redrawn from Blake and Sleight (1974).

drag on a slender body moving tangentially through the flow is approximately half that on an equivalent body moving normally. This “two to one ratio”, first described in the resistive force theory of Gray and Hancock (1955) is the basis for flagellar and ciliary propulsion.

Swimmers in Stokes flow move in such a way that no net forces (Taylor, 1951) or torques (Chwang and Wu, 1971) act upon them. Thus, the far-field of the flow arising from a Stokes swimmer is given by singularities of higher order than the stokeslet. By taking derivatives of the stokeslet, it is possible to derive the flow fields arising from, for instance, point stresses and point torques. These provide valuable insight into the far-field behaviour of the fluid surrounding swimming cells, and into the hydrodynamic effects arising from the inclusion of no-slip boundaries in the flow (Blake, 1971a; Vilfan and Jülicher, 2006). With each increase in the order of singularity, the decay of the fluid velocity in the far-field is increased by $\mathcal{O}(1/r)$, so that stokeslets decay with $\mathcal{O}(1/r)$, stokes dipoles decay with $\mathcal{O}(1/r^2)$ and stokes quadrupoles with $\mathcal{O}(1/r^3)$.

Singularity models capture many of the essential features of cilia and flagella driven flows. For small swimmers, such as sperm, bacteria and algae, gravitational sedimentation has a negligible effect upon the flow field, so that the zero total force condition gives stresslet behaviour in the far-field (Drescher et al., 2011). Larger swimmers, such as *Volvox Carteri* colonies, are subject to a significant gravitational force, resulting in a stokeslet far-field (Drescher et al., 2010).

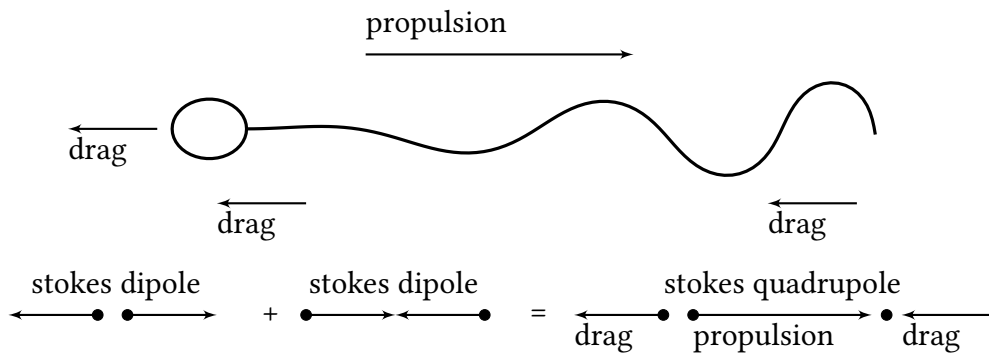


Figure 1.9: An approximate singularity representation of the flow field surrounding a human sperm, redrawn from Smith and Blake (Smith and Blake, 2009). The quadrupole representation was suggested after calculation of the force distribution in the tail with slender body theory.

Closer to the cell the flow field is more complex. For biflagellate algae, the time averaged flow field arising from two propulsive flagella and the cell body may be represented by three stokeslets (Drescher et al., 2010). For sperm, simulation (Smith and Blake, 2009) predicts that the surrounding flow may be approximated by a stokes quadrupole, arising from drag components at the front and rear of the cell and a propulsive component in the middle, shown in figure 1.9.

Two dimensional flow and Stokes' Paradox

The $\mathcal{O}(1/r)$ decay of the stokeslet has important consequences for the solution of flow arising from translating rigid bodies in unbounded fluid domains. Far from a body of typical length L , translating with speed U , the perturbation to the stagnant flow is $\mathcal{O}(UL/r)$, so that the body generates infinite flux at infinity. This is because the inertial terms that have been discarded from the Cauchy momentum equation (1.1a) are of a comparable magnitude to the viscous terms when r is $\mathcal{O}(\mu/[\rho U])$. However, solution of flow past rigid bodies in Stokes flow is still

possible, due to the error in the velocity solution approaching zero at infinity: neglecting the inertial terms is not valid only for regions where the fluid is essentially unperturbed by the translating body. Furthermore, for free swimmers zero net force acts on the fluid and the far-field is dominated by the stresslet or higher-order singularities, which do not entail the unphysical aberration of infinite flux.

For two dimensional flow, however, no solutions are possible for flow arising from translating rigid bodies in unbounded fluid domains. This is because the flow arising from a point force in two dimensions diverges as $\log r$ far from the force (Batchelor, 1967). However, this paradox is not present the case of force-free swimmers, or by the inclusion of boundaries. Stokes' Paradox pertains to translating bodies in unbounded two dimensional flow, and is thus an important consideration when modelling swimmers under these conditions. However, human sperm navigate the convoluted channels of the fallopian tubes (figure 1.1b), and so a more faithful model of their swimming is given by finite domains. As a first step to modelling three dimensional systems, it can be highly instructive to consider two dimensional flow models of swimming. Thus, following the recent work of Teran et al. (2010) or Crowdy (2011), the modelling that we will present in chapters 2 and 3 will be in finite, two dimensional domains. A discussion of the particular rheological model we will employ now follows.

1.2.2 Swimming in non-Newtonian fluids: shear dependent viscosity

The Stokes flow equations provide important insights into the mechanisms underlying viscous propulsion, for instance stroke irreversibility. However, many biological fluids are suspensions of long polymer chains which will tend to align with flow and relax to a coiled state when stretched out. These fluids have complex rheological properties, and the Stokes flow equations do not give an accurate representation of the fluid dynamics. In such cases, fluid rheology can have a significant impact upon a swimmer's progression, which may have important consequences for the study of internal fertilisation.

The need for detailed study of non-Newtonian swimming has long been recognised (Mills and Katz, 1978; Katz et al., 1980). A property of polymer suspensions that has received much recent study (Lauga, 2007b; Fu et al., 2009; Teran et al., 2010; Pak and Lauga, 2011; Zhu et al., 2012) is fluid elasticity. Viscoelastic fluids retain an elastic memory of their recent flow history. Swimmers in viscoelastic fluid can gain propulsive advantages by timing their stroke with the fluid elastic recoil (Fu et al., 2009). However, it has also been shown that that the effect of fluid viscoelasticity is dependent upon the method of swimming employed, helping flagellated pushers yet hindering swimmers that generate propulsion by squirming (Lauga, 2007b; Teran et al., 2010; Zhu et al., 2012).

Another property of polymer suspensions is a dependence of the apparent fluid viscosity on shear rate $\dot{\gamma}$. This arises from the polymers' tendency to be stretched and aligned by shear flow. However, relatively less study (Balmforth et al., 2010; Shen et al., 2012) has been given to understanding the been given to understanding the impact of shear dependent viscosity on viscous swimming. Modelling viscous swimmers with prescribed swimming strokes in fluids with shear dependent viscosity will form the focus of this thesis.

We will consider a class of fluids for which the effective fluid viscosity μ_{eff} is a function of the shear rate $\dot{\gamma}$. These are known as generalised Newtonian fluids (Phan-Thien, 2002). The dynamics of the flow are then governed by

$$\nabla \cdot (2\mu_{\text{eff}}(\dot{\gamma})\boldsymbol{\varepsilon}(\mathbf{u})) - \nabla p + \mathbf{F} = 0, \quad \nabla \cdot \mathbf{u} = 0. \quad (1.11)$$

For shear thinning fluids, the effective viscosity μ_{eff} decreases as shear rate $\dot{\gamma}$ increases.

Shear-thinning rheology leads to regions of the flow domain where the fluid is highly viscous and regions where the fluid is thinner. Swimmers in shear-thinning fluids generate a surrounding envelope of thinned fluid which will have a non-trivial effect on the swimmer.

The simplest constitutive law modelling shear dependent viscosity is the power law,

$$\mu_{\text{eff}}^{\text{pow}}(\dot{\gamma}) = \mu_0 \dot{\gamma}^{n-1}. \quad (1.12)$$

For $n = 1$, the power law reduces to Stokes flow, $n > 1$ describes shear-thickening fluids, an example being Oobleck, a paste of cornstarch and water, and $n < 1$ gives shear-thinning fluids (figure 1.10a). However, the power law is inaccurate at very high and very low shear rates, predicting zero or infinite effective viscosities respectively.

An alternative model of polymer suspensions is given by the Carreau constitutive law (Carreau, 1968)

$$\mu_{\text{eff}}^{\text{car}}(\dot{\gamma}) = \mu_{\infty} + (\mu_0 - \mu_{\infty})(1 + (\lambda\dot{\gamma})^2)^{(n-1)/2}, \quad 0 < n \leq 1. \quad (1.13)$$

The effective viscosity of a Carreau fluid decreases monotonically between the zero strain rate viscosity, μ_0 , and an infinite strain rate viscosity μ_{∞} , shown in figure 1.11. The characteristic time scale on which an extended polymer chain relaxes to a coiled rest state is given by λ .

Generalised Newtonian constitutive laws may also be used to model yield stress fluids, which behave as solids until a critical threshold of stress $\tau_y = \mu_{\text{eff}} \cdot \dot{\gamma}$ is exceeded, after which they flow. This behaviour typically results in a mixture of yielded and unyielded regions within the flow. For example, if a Bingham fluid (Bird, 2002)

$$\begin{aligned} \dot{\gamma} &= 0 && \text{if } \tau < \tau_y, \\ \mu_{\text{eff}}^{\text{bin}}(\dot{\gamma}) &= \mu_0 + \frac{\tau_y}{\dot{\gamma}} && \text{if } \tau \geq \tau_y, \end{aligned} \quad (1.14)$$

flows down a circular pipe under the action of a constant pressure gradient, a solid plug of unyielded fluid is carried down the centre of the pipe. The plug is carried by the yielded region between the plug and the pipe walls (Frigaard et al., 1994). This flow occurs, for example, when

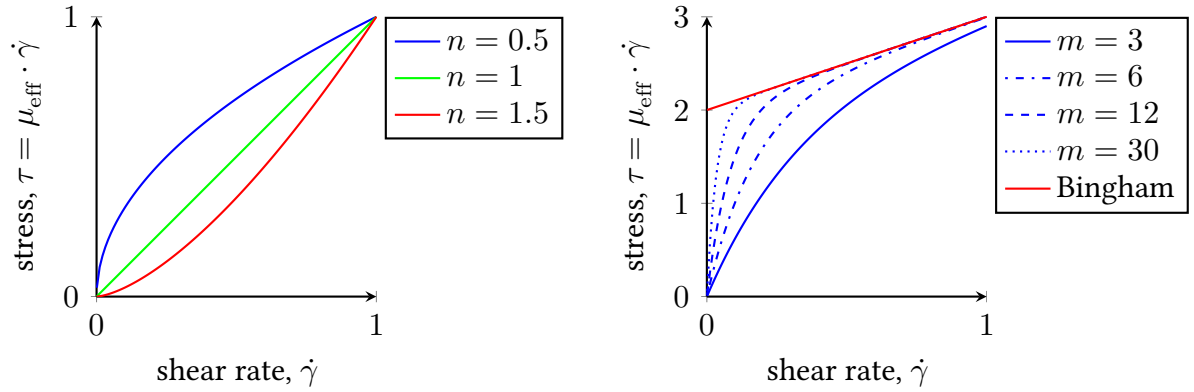


Figure 1.10: Stress - shear rate graphs of (a) power law fluids with $\mu_0 = 1$ and differing values of the exponent n and (b) a Papanastasiou fluid with $\mu_p = 1$ and $\tau_y = 2$, gradually approaching the Bingham law as the stress growth exponent m increases.

toothpaste is squeezed from a tube, flowing out yet emerging as a solid. The Bingham constitutive law is the simplest fluid that exhibits yield stress behaviour; once yielded, it behaves as a Newtonian fluid.

However, for Bingham flow there is not a single stress-strain relation that is valid throughout the whole domain; there is no information about the stress in the unyielded portion of the fluid. This presents problems in the numerical solution of such flow. An alternative model was proposed by Papanastasiou (1987),

$$\mu_{\text{eff}}^{\text{pap}} = \mu_p + \tau_y \left(\frac{1 - e^{-m\dot{\gamma}}}{\dot{\gamma}} \right). \quad (1.15)$$

Note that as the stress growth exponent m increases, the Papanastasiou law gives a better approximation to a Bingham fluid as shown in figure 1.10b. In fact, experiments have shown that in certain cases, for instance solvent-based paints (Ellwood et al., 1990), the Papanastasiou model provides a better approximation of rheological data, though this is to be expected since the Papanastasiou law has more free parameters.

Upon examining the Papanastasiou constitutive law (1.15), it becomes clear that it shares

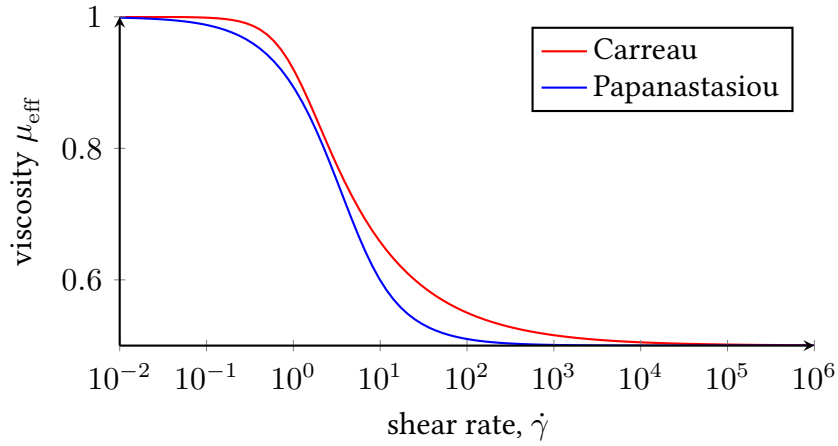


Figure 1.11: The effective viscosity of Carreau and Papanastasiou fluids as a function of shear rate $\dot{\gamma}$ for $\mu_0 = 1$, $\mu_\infty = 0.5$, $m = 0.3$, $\lambda = 1$ and $n = 0.5$ showing their rheological similarity.

some similarities with the Carreau law (1.13). Firstly,

$$\text{As } \dot{\gamma} \rightarrow \infty, \mu_{\text{eff}}^{\text{pap}} \rightarrow \mu_p + \tau_y \cdot 0 = \mu_p. \quad (1.16)$$

Thus, like Carreau fluid, Papanastasiou fluids exhibit an infinite shear rate viscosity, so that $\mu_\infty \equiv \mu_p$. Furthermore,

$$\text{As } \dot{\gamma} \rightarrow 0, \mu_{\text{eff}}^{\text{pap}} \rightarrow \mu_\infty + \tau_y \left(\frac{1 - (1 - m\dot{\gamma})}{\dot{\gamma}} \right) = \mu_\infty + \tau_y \cdot m, \quad (1.17)$$

and thus Papanastasiou fluids also have a zero shear rate viscosity, with $\mu_0 \equiv \mu_\infty + \tau_y \cdot m$. Both models decrease monotonically between zero and infinite shear rates, so we may say that these models are in a sense phenomenologically similar, as shown in figure 1.11. Thus, for the swimming problems that we will model later, we will adopt the Carreau law, which is more typically used to characterise mucus (Lai et al., 2009).

The most common tool for examining the rheology of cervical mucus is the cone and plate rheometer (Lai et al., 2009). Mucus is held between a flat plate and a cone, and the plate rotates. By controlling the applied shear stress or strain over a long time scale, the viscous

properties of the fluid can be measured. By rotating the cone at different frequencies, the elastic response of the fluid can be measured. The viscous response of human cervical mucus was examined for human cervical mucus in Lai et al. (2007). Fitting data from Lai et al. (2007) to the Carreau constitutive law with a least squares method, we found rheological parameters in the region of $\mu_0 = \mathcal{O}(10^3)$ Pa \cdot s, $\mu_\infty = \mathcal{O}(10^1)$ Pa \cdot s, $\lambda = \mathcal{O}(10^0)$ s and $n \approx 0.5$. However, for swimming problems that entail beating flagellar, it is arguably more appropriate to extract rheological data with oscillatory rheometry, and as early as 1945 researchers have observed that the elastic recoil time of mucus is “lightning fast” (Clift, 1945). This shows that value of $\lambda \approx 1$ s may not be accurate for the application of flagellated swimmers. A rigorous framework for the simultaneous extraction of viscous and elastic properties, including shear-thinning, under large amplitude oscillatory rheometry was developed by Ewoldt et al. (2008), however this has yet to be applied to human cervical mucus. The parameter values used in this study are $\mu_0/\mu_\infty = \mathcal{O}(10^1)$, $\lambda = \mathcal{O}(10^{-1})$ and $n \geq 0.3$, which for μ_0/μ_∞ and λ are an order of magnitude lower than suggested by Lai et al. (2007) in order to achieve a convergent numerical scheme. Since the methodology of Ewoldt et al. (2008) has yet to be applied to human cervical mucus, rather than focus on fluids with biologically realistic parameter values, we will examine the physical effects that changing fluid rheology has upon swimmers with prescribed kinematics.

For swimmers with prescribed strokes, a characteristic velocity is given by $U = \omega L$, where ω is the angular frequency of the swimmer’s stroke and L is a characteristic length, for instance the length of a flagellum. Scaling the force by $\mathbf{F} = \mu_\infty \omega L \hat{\mathbf{F}}$ and stress $\boldsymbol{\sigma} = \mu_\infty \omega L \hat{\boldsymbol{\sigma}}/L$ gives a dimensionless form of equation (1.13),

$$\hat{\nabla} \cdot \left[2 \left(1 + \left[\frac{\mu_0}{\mu_\infty} - 1 \right] \left[1 + \left(\lambda \omega \hat{\gamma} \right)^2 \right]^{(n-1)/2} \right) \hat{\boldsymbol{\varepsilon}}(\hat{\mathbf{u}}) \right] - \hat{\nabla} \hat{p} + \hat{\mathbf{F}} = 0, \quad (1.18a)$$

$$\hat{\nabla} \cdot \hat{\mathbf{u}} = 0. \quad (1.18b)$$

Thus, for swimmers exhibiting prescribed beat kinematics, trajectories are dependent only on three dimensionless quantities: the viscosity ratio μ_0/μ_∞ , the power law index n and the Deborah number $De = \lambda\omega$. While the Deborah number is more commonly associated with viscoelastic flows, its physical meaning as a ratio of elastic response time and characteristic flow time is appropriate for Carreau flow. This non-dimensionalisation has reduced the number of free parameters from 4 to 3.

The dependence of the trajectories of swimmers with prescribed kinematics upon these three dimensionless parameters of Carreau flow is in contrast to Stokes flow, in which swimmers with a prescribed waveform exhibited no dependence on the viscosity. The absolute values of the viscosity only become important when flagellar forces are prescribed within the context of a fluid-structure interaction model, which we will not consider. Having discussed the equations governing Newtonian and non-Newtonian fluid mechanics, we will now focus on viscous swimming, and the computational techniques that have been employed in its study.

1.3 Studies of microscopic swimming

The active locomotion of cells and transport of fluids on microscopic scales has been a benchmark problem in applied mathematics for the past 60 years, since Taylor (1951) demonstrated that a two dimensional sheet could swim in Stokes flow by propagating a travelling wave down its length. The field had already been studied extensively by zoologists (Engelmann, 1868; Verworn, 1891; Parker, 1905; Gray, 1928), however progress was accelerated greatly when experimentalists and theoreticians began to collaborate. It was in this spirit of collaboration, fostered by Taylor and Gray, that Hancock (1953) first developed slender body theory (SBT), a powerful method based upon modelling slender swimmers by distributions of force singularities.

1.3.1 Singularity-based approaches

The idea underlying singularity-based approaches is that free, immersed boundaries representing the swimmer may be approximated by a distribution of force that drives the fluid. This is a common strand that runs through almost all of the computational approaches to viscous swimming, including that which we will develop in chapter 2. Singularity approaches were applied to viscous swimming in Hancock (1953), in which a headless flagellum moving through Newtonian fluid was modelled by placing a weighted distribution of stokeslets S_{ij} and source dipoles D_{ij} along its centreline. The surface of the flagellum is modelled as a cylinder of radius a extruded along the centreline.

For Stokes flow, there is no explicit time dependence. Thus, the velocity field is defined instantaneously by the singularities and their positions along the flagellum centreline. This may be extracted from experiment, or some prescribed function, such as a travelling bending wave. Applying these Dirichlet velocity conditions on the flagellum surface yields constraints on the weightings $f_j(s)$ and $g_j(s)$ (Hancock, 1953). The swimmer's translational and angular velocities at each instant of the waveform, $\mathbf{U}, \mathbf{\Omega}$ provide additional unknowns which are closed by the conditions that zero net force (Taylor, 1951) or torque (Chwang and Wu, 1971) act on the swimmer.

The fundamental mechanism by which flagellar deformations give rise to propulsion in Stokes flow is derived from the algebraic approximation of SBT, first given by Gray and Hancock (1955) and shown schematically in figure 1.8. For a slender body, the drag coefficient associated with normal motion is approximately twice that associated with tangential motion,

$$C_t = \frac{2\pi}{\ln \frac{2\lambda}{a} - \frac{1}{2}}, \quad \frac{C_n}{C_t} \approx 2, \quad (1.19)$$

where λ is the wavelength of the flagellar beat, and a the cross-sectional radius of the flagellum. This is known as the Resistive Force Theory (RFT). A propagating wave generates a net

propulsive force that is balanced by the drag on the cell body as it swims, resulting in zero net force and torque acting upon the swimmer. The value of these RFT coefficients was later improved upon by Lighthill (1976)

$$C_t = \frac{2\pi}{\ln \frac{2q}{a}}, \quad C_n = \frac{4\pi}{\ln \frac{2q}{a} + \frac{1}{2}}, \quad (1.20)$$

where $q = 0.09\Lambda$, for Λ the wavelength measured along the centreline of the flagellum.

RFT can compare favourably with experimental data, (Dresdner and Katz, 1981; Friedrich et al., 2010), and Johnson and Brokaw (1979) showed that for a headless flagellum far from any surfaces, RFT provides a good estimate for the force distribution provided a problem-dependent heuristic adjustment is made to the anisotropy ratio C_n/C_t . However, because of the dominance of viscous forces, Stokes flow is characterised by long-range hydrodynamic reactions as embodied by the $\mathcal{O}(1/r)$ decay of the stokeslet. RFT discounts these interactions (Lighthill, 1975) and so is inaccurate when the swimmer has a large body (Johnson and Brokaw, 1979), is near a boundary, or when the flagellum exhibits high-amplitude, short-wavelength beating resulting in flagellum self-interaction, as with human sperm swimming in highly viscous media (Smith et al., 2009c). It is also particularly inaccurate at either end of the flagellum, since the assumption that an element of the flagellum is ‘slender’ breaks down at the ends of the filament.

SBT has been used extensively for microscopic swimming studies. Chwang and Wu (1971) used a cylindrical model of the flagellum and applied an additional drag force due to a translating sphere to model a bacterium swimming with a helical beat. They derived an optimal value for the head size to tail length ratio and compared the relative efficiency of helical and planar beating for simple beat patterns. In a later paper, Chwang and Wu (1975) derived the flow solutions for a prolate ellipsoid translating and rotating through a fluid using a line distribution of stokeslets and dipoles, and Johnson (1980) created an improved SBT whereby the

flagellum was represented as a slender, prolate ellipsoid. Smith et al. (2007, 2009b) showed that ‘end errors’, the errors associated with the breakdown of the slenderness assumption at the ends of the flagellum, extended a significant distance along the flagellum when it is modelled as a curved cylinder, and instead used a ‘curved ellipsoidal’ representation based upon that of Chwang and Wu (1975) and Johnson (1980) which greatly reduced these errors.

To allow for the inclusion of no-slip boundaries in the flow, the ‘method of images’ was applied to Stokes flow singularities (Blake, 1971a; Liron and Mochon, 1976). It was shown that for a given singularity in infinite flow, the effect of a no-slip boundary could be included by placing appropriate singularities, the image system, the opposite side of the boundary. Higdon (1979) developed a SBT that included an image system to model a spherical head, thereby including both flagellum-flagellum and flagellum-body interactions. However, this methodology was restricted to spherical cell morphology. Furthermore, whilst more accurate than RFT, SBT is still inaccurate when the assumption of slenderness breaks down; for strong interactions with a boundary or the cell body and high flagellar curvature (Gaffney et al., 2011).

A resolution was found in the boundary element method (BEM) of Youngren and Acrivos (1975), which was first applied to flagellar dynamics in Phan-Thien et al. (1987) and benchmarked against existing SBT results in Ramia et al. (1993). By considering surface distributions of singularities, BEM gives the fluid forces acting on a body with prescribed boundary conditions in a Newtonian fluid, from which the flow field and swimming velocity of the body may be calculated. Thus, BEM makes no assumption about the slenderness of a swimmer, and so is perfect for modelling systems where this approximation may not be valid, as in the case of primary cilia (Smith et al., 2012).

Smith et al. (2009b) used a hybrid BEM/SBT for the cell head/flagellum to allow flow calculation of swimmers with biologically accurate cell morphologies. The scheme was used to study the phenomenon of boundary accumulation for human sperm with realistic heads. Boundary accumulation was first quantitatively measured by Rothschild (1963), who noted

that in droplets of bull semen placed between two slides, sperm would accumulate near either surface. Rothschild then went on to hypothesise that hydrodynamic interaction between the sperm head and the wall resulted in an attractive force. Smith et al. (2009b) found critical conditions on the beat wavelength under which the cells would either be attracted to or escape from the boundary, which has potential important consequences in fertility treatments. Furthermore, Smith et al. (2009b) found that a realistic head morphology, whilst having 2% more resistance to forward motion than an equivalent spherical head, actually conferred a propulsive advantage to the cell. This is because resistance to rolling was almost doubled, and the decrease in cell yaw led to a 2.8% increase in progress. Gillies et al. (2009) employed a model with an ellipsoidal head, and observed the same effect; elongation of the ellipsoidal head increased drag, resulting in a reduction of yaw.

When fluid modelling is coupled with a structural model of the flagellum, head morphology can have a dramatic impact upon the cell. Gadêlha et al. (2010) modelled human sperm using a geometrically nonlinear fluid-structure interaction method described in section 1.3.2, with head morphology incorporated through BEM and flagellum-fluid interaction incorporated through RFT. Gadêlha et al. (2010) showed that at high viscosity, changes in head morphology affected the waveform through a buckling instability resulting in dramatic changes to cell trajectory. Such studies show the importance of modelling a realistic cell morphology when considering a given system.

With the advent of more powerful computers, SBT and BEM could be used to consider the optimisation of a swimmer's beat pattern or morphology. In Tam and Hosoi (2007), the stroke pattern of Purcell's three-linked swimmer, figure 1.7a, was optimised for both energy efficiency and swimming speed. The swimmer was modelled as a jointed chain of three slender rods using SBT, yielding an optimal stroke pattern that was more efficient than that found by previous studies, such as that of Becker et al. (2003) which did not consider hydrodynamic interactions between links. Shum et al. (2010) utilised BEM to model both swimmer body and a helical,

bacterial flagellum. It was found that hydrodynamic interactions with the boundary could trap the bacteria in circular swimming trajectories, previously observed for *E. coli* swimming near a boundary by Lauga et al. (2006). The radius of the orbit was shown to be sensitive to the morphology of the cell.

Since the flow solutions arising from singular forces, stresses and torques are not valid at the location of the singularity, Cortez (2001) developed the method of regularised stokeslets, which has been used in a number of recent studies (Cisneros et al., 2007; Gillies et al., 2009; O'Malley and Bees, 2012). A regularised stokeslet gives the fluid flow arising from a concentrated 'blob' force $\mathbf{F} = g^\epsilon(\mathbf{x} - \mathbf{x}_s)\mathbf{f}$, where g^ϵ is a cut-off function giving the envelope of the blob force in terms of the regularisation parameter ϵ . This introduces an error of $\mathcal{O}(\epsilon^2)$ in the calculated flow field, which is small provided ϵ is small, and allows the flow field to be calculated at exactly the location of the singularities. The image system for a particular choice of g^ϵ was given in (Ainley et al., 2008), allowing the inclusion of no-slip domain boundaries. A version of the boundary element method using regularised stokeslets was used in Smith et al. (2011) and Smith et al. (2012) to simulate symmetry breaking flow in the developing mouse and zebrafish embryos respectively.

1.3.2 Filament mechanics

By utilising the RFT approximation of the effects of fluid drag on the flagellum, it is possible to derive a partial differential equation that governs the fluid structure interaction of one dimensional filaments under certain conditions without explicit calculation of the fluid flow. This modelling program was instigated by Machin (1958), who showed that experimentally observed flagella waveforms of sperm must be generated actively along the length of the flagellum, rather than arising from drag on a passive filament driven at the base. Hines and Blum (1978, 1979) extended this framework, modelling the flagellum as a geometrically nonlinear beam with an additional term to characterise the response to the shear forces that drive the

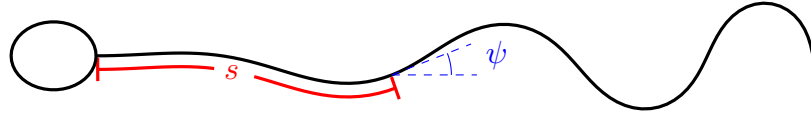


Figure 1.12: The shear angle ψ as a function of arclength along the flagellum for a swimmer resembling a human sperm.

axoneme. This was then further extended to model swimming filaments with cell bodies by Camalet and Jülicher (2000). By considering the two dimensional schematic model of the axoneme employed by Riedel-Kruse et al. (2007); Hilfinger et al. (2009), shown in figure 1.13, the following equation for the shear angle may be derived (Camalet and Jülicher, 2000; Riedel-Kruse et al., 2007)

$$C_n \frac{\partial \psi(s, t)}{\partial t} = -E \frac{\partial^4 \psi(s, t)}{\partial s^4} + \tau_0 \frac{\partial^2 \psi(s, t)}{\partial s^2} + a \frac{\partial^2 f(s, t)}{\partial s^2} \quad (1.21)$$

where C_n is the normal drag coefficient from RFT, E is the bending stiffness of the filament, a is the filament radius and f is the shear force. The dependent variable $\psi(s, t)$ is the filament shear (tangent) angle, shown in figure 1.12. The constant τ_0 is the first term in an asymptotic expansion of the filament tension, which is determined by the constraint that the filament is inextensible (Camalet and Jülicher, 2000). If no external force is applied to the tail or the cell is swimming freely, then $\tau_0 = 0$.

The shear force $f(s, t)$ is generated within the axoneme, and so its form is dependent on the mechanisms that regulate the attachment and detachment rates of the dynein molecular motors that drive the relative sliding of microtubule doublets. However, the mechanism that controls these rates is still unknown. Here we summarise three of the most popular competing theories.

Brokaw (1971, 1972, 1984, 1994, 1999, 2002, 2009) developed a sliding filament model whereby the local magnitude of the shear force generated by active sliding of the doublet microtubules

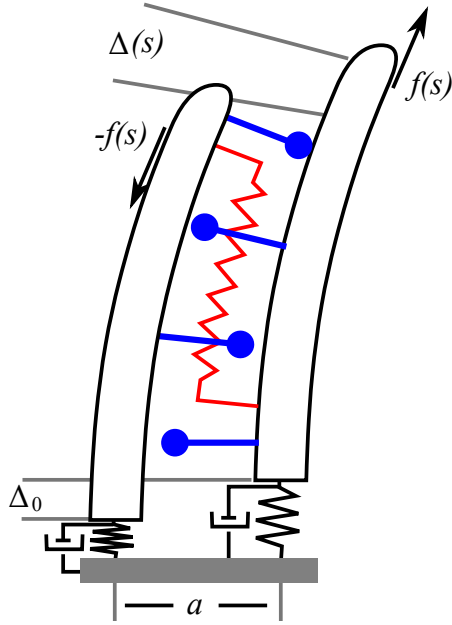


Figure 1.13: View of the beat plane of a two dimensional model axoneme, redrawn from Riedel-Kruse et al. (2007), with sliding displacement $\Delta(s)$, internal shear force density $f(s)$ due to the active dyneins (blue), and the passive nexin links (red). There is some sliding allowed at the basal body (grey), represented by springs and dashpots.

is regulated by the local curvature of the axoneme, so that in the simplest case

$$f(s, t) \propto \kappa(s, t - \tau) \quad (1.22)$$

for f the active shear force and τ some time delay. This generates a feedback loop in the axoneme that is able to yield rhythmic travelling waves that propagate from base to tip. This is known as the ‘Curvature Control’ hypothesis.

In contrast, Lindemann (1994a,b, 1996, 2002, 2004, 2009) proposed that the activity of the dynein motors responds to changes in interdoublet spacing. If neighbouring doublets slide relative to one another, the nexin links binding them must stretch. This generates a tensile force in the doublets, which decreases the distance between doublets. It is the ‘Geometric Clutch Hypothesis’ that the shorter the inter-doublet distance, the easier for the dynein arms to bind to their neighbouring doublet. This increases the rate at which the dynein motors

are ‘on’, creating a positive feedback. Motion is then slowed by the rigid elements within the flagellum which oppose bending.

The ‘Sliding Velocity Control’ model of Camalet and Jülicher (2000) makes the hypothesis that the dynein motors detach more rapidly as the load increases. This gives rise to a similar positive feedback as occurs in the geometric clutch model, since increases in sliding velocity result in a decrease in load (Riedel-Kruse et al., 2007). This leads to a decrease in the detachment rate of the dynein motors, increasing the force that they generate. Again, motion is halted by the inherent bending resistance of the flagellum ultrastructure. The force generated on one side, the ‘+’ side, say, of our two dimensional idealised axoneme is given by

$$f_+(s, t) = -\rho(s)p_+(s, t)f_+ \quad (1.23)$$

where ρ is the dynein density along the filament, p_+ is an attachment probability and f_+ is the force generated by a single dynein motor, assumed to depend linearly on the sliding velocity.

The framework developed by Camalet and Jülicher (2000) was used by Riedel-Kruse et al. (2007) to compare these three control hypotheses. Flagellar beat patterns of bull sperm moving with a planar waveform or pinned to the coverslip were captured with high-speed video microscopy, and the shear angle as a function of arclength automatically detected using an image analysis algorithm. Then, solutions to equation (1.21) were calculated and fit to the experimental data with appropriate boundary conditions, and an appropriate forcing term for each of the three models. It was found that the best agreement to the experimental data was given by the sliding velocity control model, with allowance made for compliance in the base of the axoneme to allow for some sliding in line with the observations of Vernon and Woolley (2004).

So far, the above investigations have been derived from a model of the axoneme derived from geometrically linear beam theory. However, as noted by Gadêlha et al. (2010), this is

an inappropriate assumption where the observed flagellar curvature is high, as with human sperm swimming in cervical mucus. By using the principle of virtual work (Fung and Tong, 2001) in the manner of Goldstein et al. (1998), Gadêlha et al. (2010) calculated a functional for the internal energy of the flagellum in terms of energy associated with bending forces, elastic stiffness and intrinsic resistance to extension and compression. Balancing these internal forces with external viscous drag, modelled by RFT, Gadêlha et al. (2010) derived a geometrically nonlinear equation for the flagellum centreline

$$\text{Sp}^4 \mathbf{X}_t = -\mathbf{X}_{ssss} - (\gamma - 1)(\mathbf{X}_s \cdot \mathbf{X}_{ssss})\mathbf{X}_s + (T\mathbf{X}_{ss} + \gamma T_s \mathbf{X}_s) + (f_s \mathbf{n} + \gamma f \mathbf{n}_s), \quad (1.24)$$

where $\gamma = C_n/C_t$ the ratio of normal to tangential drag and $T(s, t)$ the tension in the filament given by the incompressibility constraint. Sp is a dimensionless parameter, the ‘sperm-compliance number’ giving the relative importance of flagellum stiffness to viscous drag (Goldstein et al., 1998). Using a prescriptive model for the shear forcing of a propagating shear wave of the form $f(s, t) = A \cos(ks - t)$, rather than a local bend control hypothesis, Gadêlha et al. (2010) proceeded to show that geometrical nonlinearity can give rise to a wide range of observed phenomena.

In particular, a buckling instability not present in geometrically linear models was able to break the symmetry of the waveform, leading to morphologically sensitive curved swimming trajectories, and healthy, motile cells swimming in circles (figure 1.14). This buckling instability also resulted in a waveform similar to that observed in sperm cell hyperactivation. It was previously hypothesised that hyperactivation, thought to be crucial to successful fertilisation (Katz et al., 1989; Suarez and Ho, 2003), occurs due to either the presence of boundaries or chemical signalling. Whilst the work of Gadêlha et al. (2010) does not preclude these explanations, it is significant that, in contradistinction to linear beam theories, these observed phenomena may arise purely from the interaction between the fluid and flagellum

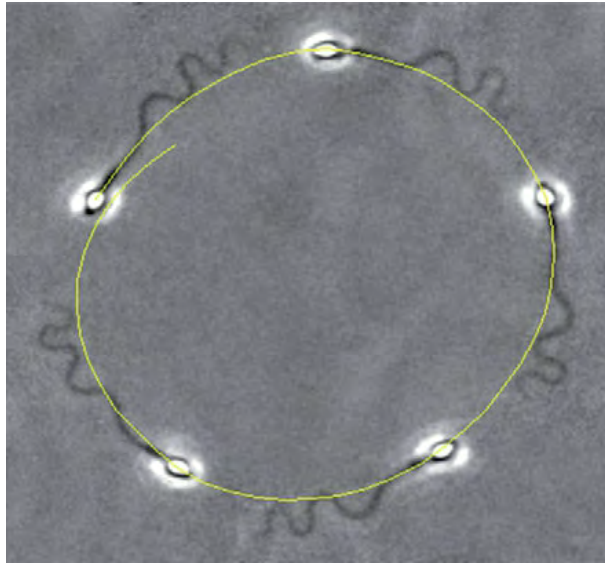


Figure 1.14: A healthy, motile human sperm, swimming in circles through a solution of methylcellulose with a viscosity comparable to the of human cervical mucus. Before the onset of the buckling instability which led to this behaviour, the cell had migrated 2 cm, which is approximately 400 times its body length. Reprinted with permission from Gadêlha et al. (2010), figure 1(b).

in the higher-order geometrically nonlinear theory. Gadêlha et al. conclude that for many parameter régimes, notably those appropriate for human sperm in the female reproductive tract, the linear theory is insufficient, and that higher-order effects can have a dramatic effect on cell migration. However, non-local fluid mechanics can also give rise to important effects, such as cilia metachrony. A fluid-structure interaction approach that utilises non-local fluid mechanics is the Immersed Boundary Method.

1.3.3 The Immersed Boundary Method

The Immersed Boundary Method (IBM) was first developed by Peskin (1972, 1977) to simulate blood flow in the heart. A two dimensional elastic boundary representation of the muscular heart wall, capturing realistic (albeit two dimensional) geometric details of the atrium, ventricle and outflow chamber, was formulated. This boundary was ‘immersed’ in a fluid satisfying the Navier-Stokes equations for Newtonian fluid with inertia, and the fully-coupled system

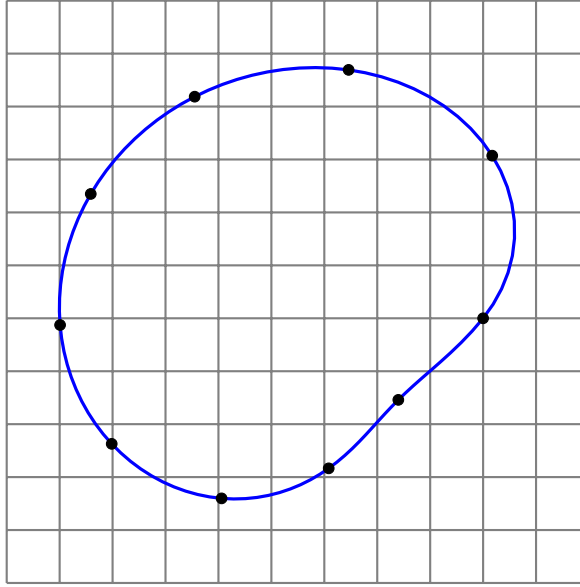


Figure 1.15: Schematic of an immersed boundary with Lagrangian points marked overlaying a Cartesian grid on which the fluid equations are to be solved. Redrawn from Mittal and Iaccarino (2005)

solved.

The fundamental idea behind IBM as applied to viscous flows is as follows. Consider the Stokes flow equations where the immersed boundary drives the flow via a localised forcing. The fluid flow is solved on a regular Cartesian grid and the immersed boundary is represented by a separate surface mesh that cuts through the regular fluid mesh, as shown in figure 1.15.

This differs from body conforming methods, wherein the mesh fits around any flow boundaries, ‘conforming’ to the flow domain geometry. The location of the immersed boundary is tracked in a Lagrangian fashion by a collection of massless particles \mathbf{X}_k (Mittal and Iaccarino, 2005) moving with the fluid velocity

$$\frac{\partial \mathbf{X}_k}{\partial t} = \mathbf{u}(\mathbf{X}_k, t). \quad (1.25)$$

The elastic stress in the immersed boundary is given by a constitutive equation, for example Hooke’s law, which links these particles together. The localised forcing of particle m is given

by

$$\mathbf{f}_m(\mathbf{x}, t) = \sum_k \mathbf{F}_k(t) \delta(\mathbf{x} - \mathbf{X}_k). \quad (1.26)$$

Since the position of the Lagrangian points will not in general coincide with the nodes of the Cartesian grid, the force (1.26) must be distributed over the surrounding nodes. Errors associated with this may then be mitigated by locally refining the mesh around the immersed boundary.

The IBM was first applied to swimming problems by Fauci and Peskin (1988). The Navier-Stokes equations, driven by a force-field given by the immersed sheet, were solved in two dimensions on a periodic, regular, Cartesian grid using the finite difference scheme of Chorin (1968). Fauci (1990) used the same methodology to examine the hydrodynamic interaction between swimming filaments, measuring the effects of phase-difference and proximity of neighbouring filaments upon their swimming speed and energy dissipation. Fauci and McDonald (1995) incorporated the effects of solid and elastic boundaries into this model, and showed that neighbouring organisms tend to adjust their swimming speed in order to lock their beat-phases together. Fauci (1996) extended this modelling to include multiple interacting swimmers and a representation of biflagellate algal cells.

Dillon and Fauci (2000) worked within this framework to model ciliary beating, using a two dimensional schematic representation of the internal structure of the axoneme whereby active and passive structures such as nexin links, sliding microtubules and active dyneins were represented by connected elastic sub-filaments. An asymmetric stroke activation where the effective stroke was modelled with constant dynein activation, with dynein activation progressing down the cilium during the recovery stroke, gave a good qualitative representation of the beat pattern of lung cilia. The methodology was reviewed in Fauci and Dillon (2006) and used by Dillon et al. (2007) to examine mucociliary transport for a two dimensional array of three sequential cilia situated beneath a mucus layer modelled by an elastic immersed boundary. Following on from this, Yang et al. (2008) used the same IBM framework with a two

dimensional idealised model of the axoneme to show that metachrony could arise in neighbouring cilia purely from hydrodynamic coupling without the need for either elastic coupling through the cell surface or any chemical signalling between cilia, as had also been investigated using singularity methods and rod theory by Gueron et al. (1997).

One of the principal advantages of IBM for solving moving boundary problems is that the background Cartesian mesh does not need to be adjusted between time steps, irrespective of the position of the immersed boundary. In solving fluid mechanics for which the governing equations have some time dependence, such as the Navier-Stokes equations which include inertial effects, or viscoelastic fluids which include elastic memory effects, the solution from the previous time step is required in the solution of the fluid equations. Thus, a fixed Cartesian mesh does not suffer from the errors associated with the projection of the previous fluid solution onto a new mesh. However, our governing fluid equations contain no time dependence, and so there is no need to project the fluid solution from previous time steps; the flow field is determined instantaneously by the boundary conditions. We will thus, in contrast, use a body fitted mesh for our numerical scheme.

A further advantage of IBM is that the method does not require the existence of a Green's function for the flow arising from a point force. This idea has been used for the methods we will develop in chapter 2. Thus the equations that govern the mechanics of the flow need not be linear. This allowed Teran et al. (2010) to model large amplitude flagellum fluid interaction in a nonlinear Oldroyd-B fluid, which was an important step in understanding the effects that biologically realistic fluid mechanics could exert on flagellated swimmers. A summary of other non-Newtonian swimming modelling now follows.

1.3.4 Non-Newtonian micro-swimming studies

For the swimming of mammalian sperm, we have already observed that the Stokes flow equations do not give an accurate representation of the fluid environment, namely mucus. Indeed,

it has been observed (Smith et al., 2009c) that the swimming speed of sperm in weakly viscoelastic fluid cannot be fully explained by Newtonian modelling. The problem of internal fertilisation motivated Fulford et al. (1998) to develop a Resistive Force Theory for a linearly viscoelastic fluid. This theory modified the force per unit length exerted by the fluid on the flagellum to take account of fluid relaxation

$$\lambda \frac{\partial}{\partial t} f_t(s, t) + f_t(s, t) = C_t u_t(s, t), \quad (1.27a)$$

$$\lambda \frac{\partial}{\partial t} f_n(s, t) + f_n(s, t) = C_n u_n(s, t). \quad (1.27b)$$

The Newtonian RFT normal and tangential drag coefficients C_n and C_t are still present, but the time derivative of the force also plays a rôle, as does the fluid elastic relaxation time λ . This methodology was used to show that, for small amplitude oscillations of a filament, the rate of work by a swimmer decreases as the relaxation time increases. A similar approach was applied in Lauga (2007b) and Fu et al. (2009), which found that the swimming speed of filaments exhibiting small amplitude beating was decreased in nonlinearly viscoelastic fluid.

In Smith et al. (2009a), a SBT for a linearly viscoelastic Maxwell fluid was developed by utilising a viscoelastic version of the stokeslet to model mucociliary clearance in the lung. It was found that cilia are highly sensitive to fluid rheology, particles being transferred significantly less far than in Newtonian fluids for even short relaxation times. This may have implications in the understanding of lung pathologies, such as cystic fibrosis.

The effects of fluid viscoelasticity upon a swimmer are sensitive to the method of swimming employed. Using small amplitude approximations, Zhu et al. (2012) showed that microscopic swimmers that ‘squirm’ in order to progress, such as *Opalina* and *Paramecium*, are hindered by fluid viscoelasticity, whereas as monoflagellate pushers may be aided by it (Teran et al., 2010). Furthermore, it has recently been shown (Lauga, 2009) that Purcell’s Scallop Theorem can break down in a viscoelastic fluid, net movement being made possible by forces resulting

from ‘normal stress differences’; differences between the normal components of the fluid stress tensor arising from its dependence on the fluid deformation history. These are the same forces responsible for the famous ‘Rod Climbing effect’ (Oldroyd, 1958).

Teran et al. (2010) used the IBM to study of the effects of nonlinear Oldroyd-B viscoelastic rheology on a sperm-like two dimensional sheet. They observed that, for small amplitude oscillations, swimming was impeded by the fluid elasticity. However, for large amplitude oscillations, they demonstrated that for fluid relaxation times comparable to the beating frequency of the sheet propulsion was in fact enhanced. This might be thought of as a kind of viscoelastic resonance, timing flagellar beating with the natural frequency of the fluid recoil led to propulsive gains. Tytell et al. (2010) used the IBM to couple an actuated elastic body with external flow in a model of Lamprey swimming. It was found that identical muscle activation could give rise to different beat kinematics depending upon the body stiffness, and furthermore that well-timed muscle contractions, by affecting the passive stiffness of the body, could lead to optimal swimming patterns. In the case of human sperm, such studies show the need for finite amplitude waveform calculations, together with a consideration of the differing elastic properties of the flagellum due to the passive accessory structures such as the outer dense fibres. However, a full three dimensional study without the approximation of asymptotics for the slenderness of the swimmer or the amplitude of the waveform has yet to be performed (Gaffney et al., 2011), and relatively less attention has been given to understanding the effects of shear rate dependent viscosity. This thesis will examine some of these effects.

1.3.5 Overview of this thesis

In the next chapter we will develop a new technique, the method of femlets, for simulating cell swimming in nonlinear fluids, focusing on its formulation for generalised Newtonian flow. The technique draws inspiration from both the method of regularised stokeslets, by representing the swimmer by a set of regularised forces, and the Immersed Boundary Method discussed

above, by solving the fluid flow without using Green's functions.

The method of femlets utilises a finite element projection of the governing flow equations, enabling solution of nonlinear fluid equations on irregular domains with nonuniform meshes. We discuss appropriate forms for the force regularisation and examine the errors associated with representing a moving domain boundary by a set of immersed forces. We then examine the accuracy of the time stepping procedure used to predict cell swimming trajectories.

In chapter 3, we use this method to examine the effects of shear-thinning rheology on three model swimmers in two dimensional flow. These are swimmers comprising collinear spheres, squirming models of ciliated swimmers and a model human sperm. We find that the effects of shear-thinning are sensitive to the mode of swimming employed, and discuss the underlying mechanisms by which they may aid or hinder cell progress.

Chapter 2

Developing the method of femlets to model microscopic swimmers

2.1 Finite element method stokeslets: femlets

In order to solve microscopic swimming problems in fluids with shear dependent viscosity, we will now develop the method of femlets. Drawing inspiration from the method of regularised stokeslets (Cortez, 2001), the method of femlets represents the interaction of the swimmer with the fluid through a set of concentrated ‘blob’ forces of unknown strength and direction. While the method of regularised stokeslets reduces the problem to finding the coefficients in a linear superposition of velocity solutions of known form, the method of femlets proceeds by applying the finite element method to solve for the fluid velocity field and strength and direction of the forces simultaneously. The use of the finite element method removes the need for the governing equations to be linear, while the representation of the swimmer as a set of forces provides a convenient framework for the future coupling of flagellar solid mechanics to the non local flow calculation, as with IBM. However, unlike IBM, we use a body-fitted mesh, enforcing the swimming velocity conditions at points exactly on the immersed surface and allowing for irregular domains.

In the finite element method, the domain is partitioned into subdomains (elements) and

the solution to the desired differential equation is approximated by a linear combination of low-degree polynomials ϕ_i over these elements, though higher-degree polynomials may also be used to give a more accurate approximation of the underlying solution at the cost of increasing the size of the linear system. The weak form of the differential equation is evaluated by summing the contributions from each element, then the solution found by solving the resultant linear system to give the coefficients of each basis polynomial in its expansion. This process is known as the Rayleigh-Ritz-Galerkin process (Strang and Fix, 1988).

The finite element method was applied to fluid flow by Zienkiewicz and Cheung (1965), and De Vries and Norrie (1971) later derived solutions for potential flow in complex multiply-connected domains for Dirichlet, Neumann and mixed boundary conditions. This showed the potential superiority of finite elements for fluid mechanics over then-prevalent finite difference methods owing to their ability to deal with complex geometries, non-uniform meshes and easy implementation of boundary conditions (Taylor and Hood, 1973). The full Navier-Stokes equations were solved with the finite element method in Oden (1973), and its formulation in terms of the ‘primitive’ velocity and pressure variables which will be used herein was established in Taylor and Hood (1973); Fortin (1975); Fortin and Thomasset (1979). The Stokes flow equations were first examined in Crouzeix and Raviart (1973), and Bercovier and Pironneau (1979) began the rigorous theory of the study of errors for the mixed primitive variable formulation of the Stokes flow equations, which will be used as a basis for our method of modelling cell swimming.

In order to model swimmers with prescribed cell kinematics, it is desirable to describe the swimmer’s deformation in the ‘body frame’ (Higdon, 1979) in which the swimmer’s body neither rotates nor translates. We prescribe a function for the swimmer’s configuration ∂D_{swim} and velocity \mathbf{u}_s in the body frame, and transform these conditions into the ‘lab frame’, in which the domain D is stationary. We solve the fluid flow equations formulated in the lab frame. The translational and rotational velocities that arise from the current configuration of

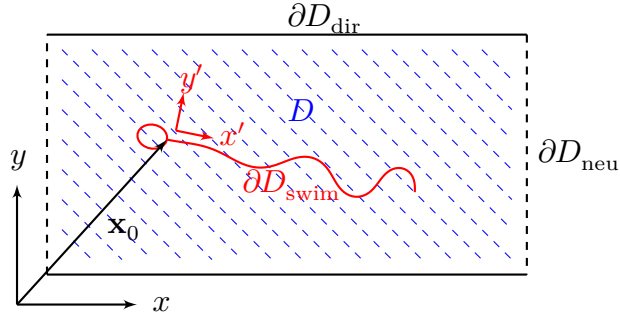


Figure 2.1: An example domain D containing a model human sperm ∂D_{swim} , showing no-slip channel walls ∂D_{dir} and open boundaries ∂D_{neu} . The relationship between the lab frame, (x, y) and the body frame, (x', y') is also shown. Femlets will be distributed along the boundary ∂D_{swim} .

the swimmer are then used to update its global position. The relationship between the body frame and lab frame is shown for a human sperm in figure 2.1. The body frame velocity \mathbf{u}_b , given by the time derivative of the swimmer's prescribed configuration, is related to the lab velocity \mathbf{u} by

$$\mathbf{u}_b = \mathbf{u} - \mathbf{U} - \boldsymbol{\Omega} \times (\mathbf{x} - \mathbf{x}_0), \quad (2.1)$$

where $\mathbf{U}, \boldsymbol{\Omega}$ are the translational and angular velocities of the body frame, and \mathbf{x}_0 is the origin of the body frame, chosen to be the point where the head and flagellum join.

The domain walls will in general have Dirichlet velocity conditions imposed upon them, for example the no-slip condition $\mathbf{u}_{\text{dir}} = \mathbf{0}$. We may also wish to consider channels of infinite length, in which case it is usual to truncate the domain. These truncated boundaries ∂D_{neu} are given the zero normal stress condition $\boldsymbol{\sigma} \cdot \mathbf{n} = \mathbf{0}$. We will now derive the method of femlets for swimmers in fluids with shear dependent viscosity. Henceforth, we will continue to use dimensionless variables, but remove the hats for simplicity.

Let D be a bounded domain in \mathbb{R}^2 . We partition the domain boundary $\partial D = \partial D_{\text{dir}} \cup \partial D_{\text{neu}}$ into those portions on which Dirichlet and Neumann type boundary conditions are applied respectively. If we were to model the surface of the swimmer ∂D_{swim} as a moving domain boundary, it would form a part of ∂D_{dir} . However, we will model the interaction of ∂D_{swim}

with the fluid by an immersed body force distribution. Thus for our case ∂D_{swim} is not a domain boundary, but rather a one dimensional manifold of points in D .

Let $H^1(D)$ be the standard Sobolev space of weakly differentiable functions (Braess, 2007) defined on D , and let

$$V_E = \left\{ \mathbf{w} \in (H^1(D))^d : \mathbf{w}|_{\partial D_{\text{dir}}} = \mathbf{u}_{\text{dir}} \right\}, \quad (2.2a)$$

$$V_0 = \left\{ \mathbf{w} \in (H^1(D))^d : \mathbf{w}|_{\partial D_{\text{dir}}} = \mathbf{0} \right\}, \quad (2.2b)$$

where \mathbf{u}_{dir} are the Dirichlet conditions imposed on ∂D_{dir} . Let also Q be the subspace of $L^2(D)$, the set of square integrable functions on D , with zero mean value on D . The spaces V_E, V_0 are the solution and test function spaces for velocity, and the solution and test function space for pressure is Q . Multiplying equations (1.11) by arbitrary ‘test’ functions $\mathbf{v} \in V_0, q \in Q$, respectively, yields the following integral form of problem (1.11):

$$\int_D \{ \nabla \cdot [2\mu_{\text{eff}}(\dot{\gamma})\boldsymbol{\varepsilon}(\mathbf{u})] - \nabla p + \mathbf{F} \} \cdot \mathbf{v} \, d\mathbf{x} = 0, \quad \int_D q \nabla \cdot \mathbf{u} \, d\mathbf{x} = 0. \quad (2.3)$$

Integration by parts yields an equivalent integral formulation with reduced differentiability requirements for \mathbf{u} and p . This is known as the weak (or variational) formulation of the generalised Stokes flow problem (1.11) and reads:

Find $(\mathbf{u}, p) \in V_E \times Q$ such that $\forall (\mathbf{v}, q) \in V_0 \times Q$,

$$\int_D 2\mu_{\text{eff}}(\dot{\gamma})\boldsymbol{\varepsilon}(\mathbf{u}) : \boldsymbol{\varepsilon}(\mathbf{v}) \, d\mathbf{x} - \int_D p \nabla \cdot \mathbf{v} \, d\mathbf{x} + \int_D \mathbf{F} \cdot \mathbf{v} \, d\mathbf{x} = 0, \quad (2.4a)$$

$$\int_D q \nabla \cdot \mathbf{u} \, d\mathbf{x} = 0, \quad (2.4b)$$

The weak form of the zero normal stress condition

$$\int_{\partial D_{\text{neu}}} \mathbf{v} \cdot \boldsymbol{\sigma} \cdot \mathbf{n} \, d\mathbf{x} = 0, \quad (2.5)$$

is applied on ∂D_{neu} . Existence and uniqueness for problem (2.4) was shown by Baranger and Najib (1990) for both the power law and Carreau models.

As the swimmer moves through the fluid, the moving boundary exerts a force distribution on the fluid that drives the flow. We incorporate this interaction through the unknown body force \mathbf{F} , which is governed by the motion of the swimmer. We approximate \mathbf{F} by a finite number of smooth elongated immersed forces with unknown components (femlets) $\mathbf{F} = \sum_{k=1}^{N_f} g^\epsilon(\mathbf{R}_k[\mathbf{x} - \mathbf{x}_k])\mathbf{f}_k$, for N_f femlets with force vector \mathbf{f}_k located at \mathbf{x}_k . The rotation matrix \mathbf{R}_k is used to orientate the femlet, so that femlets may be defined in their local frame (fig 2.2a). For simplicity, we define $\mathbf{x}_k^{\text{loc}} = \mathbf{R}_k[\mathbf{x} - \mathbf{x}_k]$. The cut-off function $g^\epsilon(\mathbf{x}_k^{\text{loc}})$ is a regularised Dirac δ distribution similar to that used in the method of regularised stokeslets (Cortez, 2001). The choice of cut-off function will be discussed in greater detail in section 2.2.2, an example being the elongated Gaussian

$$g^\epsilon(\mathbf{x}_k^{\text{loc}}) = \exp \left\{ - \left[\frac{(x_k^{\text{loc}})^2}{2\sigma_x^2} + \frac{(y_k^{\text{loc}})^2}{2\sigma_y^2} \right] \right\}, \quad (2.6)$$

shown in figure 2.2a, where the small parameter ϵ has been absorbed into the standard deviations σ_x, σ_y . The orientation of the frame $(x_k^{\text{loc}}, y_k^{\text{loc}})$ is chosen so that each femlet is aligned with the local tangent and normal to the swimmer's body, with $\sigma_x \geq \sigma_y$. The choice of σ_x, σ_y is also discussed in section 2.2.2.

Associated with each femlet k are 2 degrees of freedom, the lab frame force of each femlet in the x and y directions (f_{1k}, f_{2k}) , resulting in $2N_f$ additional scalar variables. To calculate the $2N_f$ force unknowns, we enforce $2N_f$ constraints in the form of Dirichlet velocity conditions \mathbf{u}_s . These are given by the swimmer's velocity in the body frame and applied at the location

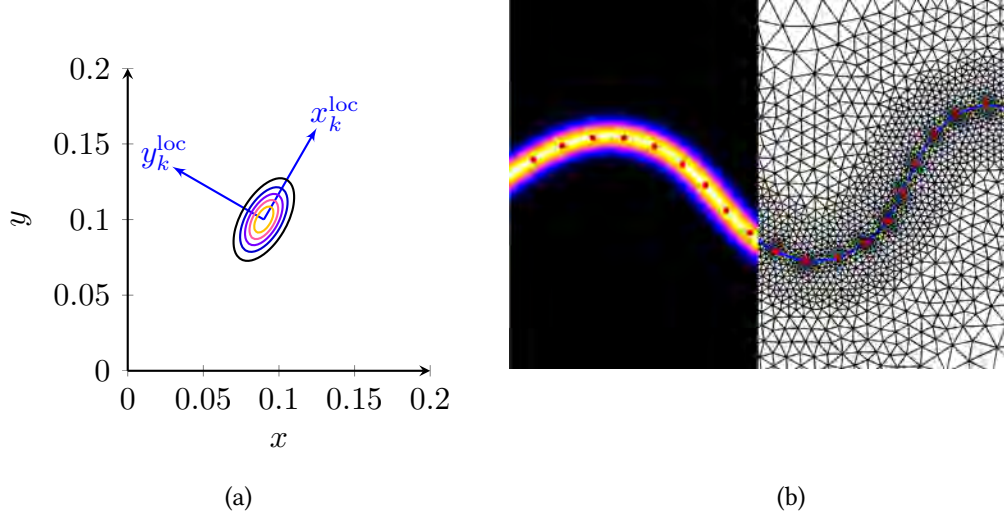


Figure 2.2: (a) The cut-off function g^ϵ , given by equation (2.6) with $\sigma_x = 0.0016$ and $\sigma_y = 0.008$, for a single femlet centered on $\mathbf{x}_k = (0.09, 1)$ and aligned at an angle of $\pi/3$ rad, showing the local frame $(x_k^{\text{loc}}, y_k^{\text{loc}})$. (b) A plot showing the smooth force distribution envelope generated by a sum of such g^ϵ when projected on a finite element mesh, for femlets at the marked locations representing a flagellum.

of each femlet.

The swimmer translational and angular velocities \mathbf{U} , $\mathbf{\Omega}$ provide additional unknowns which are closed by the conditions that zero net force (Taylor, 1951) and torque (Chwang and Wu, 1971) act on the swimmer,

$$\int_D \sum_{k=1}^{N_f} g^\epsilon(\mathbf{x}_k^{\text{loc}}) \mathbf{f}_k \, d\mathbf{x} = 0, \quad \int_D \mathbf{x} \times \sum_{k=1}^{N_f} g^\epsilon(\mathbf{x}_k^{\text{loc}}) \mathbf{f}_k \, d\mathbf{x} = 0. \quad (2.7)$$

The zero net force condition reduces simply to the condition that the sum of the femlet forces

\mathbf{f}_k is zero

$$\begin{aligned} & \int_D \sum_{k=1}^{N_f} g^\epsilon(\mathbf{x}_k^{\text{loc}}) \mathbf{f}_k \, d\mathbf{x} = 0, \\ \therefore & \sum_{k=1}^{N_f} \mathbf{f}_k \int_D g^\epsilon(\mathbf{x}_k^{\text{loc}}) \, d\mathbf{x} = 0. \end{aligned} \quad (2.8)$$

Since all femlets are given the same non-negative cut-off function g^ϵ , the value of the integral of the cut-off function may be cancelled, otherwise a simple alteration to the numerical procedure must be made that accounts for this.

We specify the velocity conditions at the femlet centroid, and also choose the cut-off function so that each femlet exerts no torque about its centroid,

$$\begin{aligned} & \int_D \mathbf{x}_k^{\text{loc}} \times (g^\epsilon(\mathbf{x}_k^{\text{loc}}) \mathbf{f}_k) \, d\mathbf{x} = 0 \quad \forall \mathbf{f}_k \\ & \int_D \mathbf{x}_k^{\text{loc}} g^\epsilon(\mathbf{x}_k^{\text{loc}}) \, d\mathbf{x} = 0, \end{aligned} \quad (2.9)$$

where as before $\mathbf{x}_k^{\text{loc}} = \mathbf{R}_k[\mathbf{x} - \mathbf{x}_k]$. Together with the relation $\mathbf{x} = \mathbf{x} - \mathbf{x}_k + \mathbf{x}_k = \mathbf{R}_k^{-1}[\mathbf{x}_k^{\text{loc}}] + \mathbf{x}_k$, this allows us to simplify the zero net torque condition to the condition that the sum of the torques exerted by the femlet forces \mathbf{f}_k is zero

$$\begin{aligned} & \int_D \mathbf{x} \times \sum_{k=1}^{N_f} g^\epsilon(\mathbf{x}_k^{\text{loc}}) \mathbf{f}_k \, d\mathbf{x} = 0, \\ \therefore & \mathbf{R}^{-1} \underbrace{\int_D \sum_{k=1}^{N_f} \mathbf{x}_k^{\text{loc}} \times g^\epsilon(\mathbf{x}_k^{\text{loc}}) \mathbf{f}_k \, d\mathbf{x}}_{=0} \\ & + \int_D \sum_{k=1}^{N_f} \mathbf{x}_k \times g^\epsilon(\mathbf{x}_k^{\text{loc}}) \mathbf{f}_k \, d\mathbf{x} = 0, \\ \therefore & \sum_{k=1}^{N_f} \mathbf{x}_k \times \mathbf{f}_k \int_D g^\epsilon(\mathbf{x}_k^{\text{loc}}) \, d\mathbf{x} = 0. \end{aligned} \quad (2.10)$$

Thus, the force and torque conditions on the swimmer may be written

$$\sum_{k=1}^{N_f} \mathbf{f}_k = 0, \quad \sum_{k=1}^{N_f} \mathbf{f}_k \times \mathbf{x}_k = 0, \quad (2.11)$$

respectively.

Under these conditions, problem (2.4) has the femlet approximation

Find $(\mathbf{u}, p) \in V_E \times Q$ such that $\forall (\mathbf{v}, q) \in V_0 \times Q$,

$$\int_D 2\mu_{\text{eff}}(\dot{\gamma}) \boldsymbol{\varepsilon}(\mathbf{u}) : \boldsymbol{\varepsilon}(\mathbf{v}) \, d\mathbf{x} - \int_D p \nabla \cdot \mathbf{v} \, d\mathbf{x} + \int_D \left[\sum_{k=1}^{N_f} g^c(\mathbf{x}_k^{\text{loc}}) \mathbf{f}_k \right] \cdot \mathbf{v} \, d\mathbf{x} = 0, \quad (2.12a)$$

$$\int_D q \nabla \cdot \mathbf{u} \, d\mathbf{x} = 0, \quad (2.12b)$$

subject to,

$$\mathbf{u}(\mathbf{x}_k, t) = \mathbf{u}_s(\mathbf{x}_k, t) + \mathbf{U}(t) - \boldsymbol{\Omega}(t) \times (\mathbf{x}_k - \mathbf{x}_0) \quad (2.12c)$$

$$\sum_{k=1}^{N_f} \mathbf{f}_k = 0, \quad \sum_{k=1}^{N_f} \mathbf{f}_k \times \mathbf{x}_k = 0, \quad (2.12d)$$

Note that problem (2.12) is nonlinear, due to the dependence of μ_{eff} on $\dot{\gamma}(\mathbf{u})$. We solve this

nonlinear system with the following Picard iteration: given an initial guess (\mathbf{u}^0, p^0) ,

For $m = 1, 2, \dots$ solve until convergence:

Find $(\mathbf{u}^m, p^m) \in V_E \times Q$ such that $\forall (\mathbf{v}, q) \in V_0 \times Q$,

$$\int_D 2\mu_{\text{eff}}(\dot{\gamma}^{m-1}) \boldsymbol{\varepsilon}(\mathbf{u}^m) : \boldsymbol{\varepsilon}(\mathbf{v}) \, d\mathbf{x} - \int_D p^m \nabla \cdot \mathbf{v} \, d\mathbf{x} + \int_D \left[\sum_{k=1}^{N_f} g^\epsilon(\mathbf{x}_k^{\text{loc}}) \mathbf{f}_k^m \right] \cdot \mathbf{v} \, d\mathbf{x} = 0 \quad (2.13a)$$

$$\int_D q \nabla \cdot \mathbf{u}^m \, d\mathbf{x} = 0, \quad (2.13b)$$

subject to

$$\mathbf{u}(\mathbf{x}_k, t)^m = \mathbf{u}_s(\mathbf{x}_k, t) + \mathbf{U}(t)^m - \boldsymbol{\Omega}(t)^m \times (\mathbf{x}_k - \mathbf{x}_0), \quad (2.13c)$$

$$\sum_{k=1}^{N_f} \mathbf{f}_k^m = 0, \quad \sum_{k=1}^{N_f} \mathbf{f}_k^m \times \mathbf{x}_k = 0, \quad (2.13d)$$

End.

For each m , problem (2.13) is linear, since $\mu_{\text{eff}}(\dot{\gamma}^{m-1}) = \mu_{\text{eff}}(\dot{\gamma}(\mathbf{u}^{m-1}))$ is evaluated with the known velocity from the previous iteration. This sequence of linear problems was solved using the following finite element method.

Since $\mathbf{u}_{\text{dir}} = \mathbf{0}$, we henceforth write $V_E = V_0$ for ease of presentation. Let D_h denote a partition of D into simplices of diameter no greater than h . Let V_0^h, Q^h be finite dimensional subspaces of V_0, Q , respectively, with bases $\{\phi_i\}_{1 \leq i \leq N}, \{\psi_j\}_{1 \leq j \leq M}$ of piecewise polynomial functions defined on the partition D_h . We consider the following discrete weak formulation

corresponding to formulation (2.12):

Find $(\mathbf{u}_h, p_h) \in V_0^h \times Q^h$ such that $\forall (\mathbf{v}_h, q_h) \in V_0^h \times Q^h$,

$$\int_D 2\mu_{\text{eff}}(\dot{\gamma}_h) \boldsymbol{\varepsilon}(\mathbf{u}_h) : \boldsymbol{\varepsilon}(\mathbf{v}_h) \, dx - \int_D p_h \nabla \cdot \mathbf{v}_h \, dx + \int_D \left[\sum_{k=1}^{N_f} g^\epsilon(\mathbf{x}_k^{\text{loc}}) \mathbf{f}_k \right] \cdot \mathbf{v}_h \, dx = 0, \quad (2.14a)$$

$$\int_D q_h \nabla \cdot \mathbf{u}_h \, dx = 0, \quad (2.14b)$$

subject to,

$$\mathbf{u}(\mathbf{x}_k, t)_h = \mathbf{u}_s(\mathbf{x}_k, t)_h + \mathbf{U}(t) - \boldsymbol{\Omega}(t) \times (\mathbf{x}_k - \mathbf{x}_0) \quad (2.14c)$$

$$\sum_{k=1}^{N_f} \mathbf{f}_k = 0, \quad \sum_{k=1}^{N_f} \mathbf{f}_k \times \mathbf{x}_k = 0. \quad (2.14d)$$

Using the expansions,

$$\mathbf{u}_h(\mathbf{x}) = \sum_{i=1}^N U_i \phi_i(\mathbf{x}), \quad \mathbf{p}_h(\mathbf{x}) = \sum_{j=1}^M P_j \psi_j(\mathbf{x}), \quad (2.15)$$

we obtain the discrete form of the Picard iteration (2.13),

$$\underbrace{\begin{pmatrix} A_{m-1} & B^T & C & 0 \\ B & 0 & 0 & 0 \\ D & 0 & 0 & T_1 \\ 0 & 0 & T_2 & 0 \end{pmatrix}}_{\mathbf{M}} \underbrace{\begin{pmatrix} \{\mathbf{u}^m\} \\ \{p^m\} \\ \{\mathbf{f}_k^m\} \\ \{U\} \end{pmatrix}}_{\mathbf{z}} = \underbrace{\begin{pmatrix} \{\mathbf{u}_{\text{dir}}\} \\ \{0\} \\ \{\mathbf{u}_{\text{swim}}\} \\ \{0\} \end{pmatrix}}_{\mathbf{r}}, \quad (2.16)$$

where

$$[A_{m-1}]_{ij} = \int_D 2\mu_{\text{eff}}(\dot{\gamma}_h^{m-1}) \boldsymbol{\varepsilon}(\phi_j) : \boldsymbol{\varepsilon}(\phi_i) \, dx, \quad [B]_{jl} = \int_D \psi_j \nabla \cdot \phi_l \, dx. \quad (2.17)$$

The N_f columns of matrix C are obtained by evaluating the cut-off function g^ϵ at each node and premultiplying by the mass matrix $\int_D \phi_i \phi_j \, dx$. The matrix D applies Dirichlet velocity

conditions, given in the swimmer's body frame on the right-hand side, at the position \mathbf{x}_k of each femlet. The matrix T_1 transforms these conditions into the lab frame, whilst T_2 applies the constraints of zero net force and torque. The velocity derivatives required for the calculation of $\dot{\gamma}_h^{m-1}$ are calculated in a weak sense by premultiplying the solution vector \mathbf{u}_h^{m-1} by the matrix B .

The iteration continues until $\|\mathbf{M}(\dot{\gamma}^{m+1})\mathbf{z}^{m+1} - \mathbf{r}^{m+1}\| < \epsilon_{\text{tol}}$, a small tolerance here set to $\epsilon_{\text{tol}} = 10^{-9}$. The matrix \mathbf{M} , vector \mathbf{r} and solution vector \mathbf{z} of the nonlinear swimming problem are as indicated by equation (2.16). The solution comprises the lab frame velocity of the fluid \mathbf{u} , the fluid pressure p , the force distribution along the swimmer \mathbf{f}_k and the swimming translational \mathbf{U} and rotational $\mathbf{\Omega}$ velocities.

The Picard iterative procedure has been chosen since it has a large radius of convergence and it is easy to implement (Mitsoulis, 2007). However, it only converges at a linear rate. In contrast, the Newton-Raphson method has a smaller radius of convergence (Böhme and Rubart, 1989), that but converges quadratically. Should numerical cost prohibit the use of the Picard scheme, it is possible to use a hybrid technique whereby a good initial guess for a Newton-Raphson scheme is provided by the Picard solver.

To provide an initial guess \mathbf{u}_0 for the Picard iteration, we first calculate the linear Stokes solution under the same conditions, i.e. with the same boundary conditions and same zero shear rate viscosity μ_0 . For fluids with a high degree of nonlinearity, we apply a natural parameter continuation (Allgower and Georg, 1990) approach whereby a series of convergent solutions is found for increasingly nonlinear fluids, each converged solution being used as an initial guess for the Picard iteration for a fluid with incrementally more nonlinearity (Karaigiannis et al., 2005; Böhme and Rubart, 1989; Mitsoulis, 2007). This approach is used in chapter 3 for simulating both collinear sphere and squirming swimmers.

For illustrative purposes, consider calculating a power law flow solution with exponent $n = 0.5$ in domain D with given boundary conditions. First, we calculate the flow arising

from the Stokes constitutive law. This flow is then used as an initial guess for the Picard iteration arising from a power law fluid of exponent $n = 0.9$, say. This is in turn used as a starting point for a calculation with $n = 0.8$ and so on until the desired level of nonlinearity, here $n = 0.5$, is reached. Natural parameter continuation is a common means of ensuring the convergence of the nonlinear solver (Zienkiewicz and Taylor, 1989) by providing at each step an initial guess that is close to the true solution.

2.1.1 Further details of the numerical implementation

In order to discretise the spatial domain D , we generate a tessellation of D with triangles that conforms to the shape of the boundaries. This is referred to as an unstructured, or body-fitted, mesh of D . The triangles form the elements, their vertices being referred to as nodes. The coordinates of the nodes are stored in a $2 \times N$ matrix p , where N is the number of nodes. The connectivity of these nodes is stored in t , a $3 \times E$ matrix where E is the number of elements. Each column of t represents a triangular element, the entries being the indices in p of the nodes belonging to that element, ordered in a local anticlockwise manner by row. Finally, the domain boundaries are stored in a $2 \times N_b$ boundary connectivity matrix, for N_b the number of element edges along the domain boundary. Each column of the edge connectivity matrix lists the nodes on a particular edge. These three matrices completely define the unstructured mesh.

The mesh is generated with the Matlab[®] program DistMesh (Persson and Strang, 2004). The domain is represented implicitly by a signed distance function $d(x, y)$, which is negative inside the domain and zero on the “level set” of the boundary. Points on the internal manifold representing the swimmer ∂D_{swim} , the location of the femlets, are fixed and will form nodes of the triangular mesh. A random, uniform distribution of points within the domain bounding box is generated, and points outside the domain for which $d(x, y) > 0$ are discarded. This set of points is triangulated with the Delaunay algorithm, and passed to an iterative mesh

generation procedure.

The iterative mesh generation technique is analogous to solving for force equilibrium of a truss. Nodes of the truss correspond to nodes of the mesh, with edges corresponding to bars. The bars are modelled by linear springs, constrained at the boundaries, and force equilibrium is used to move the nodes. A user defined size function allows control over the relative sizes of elements in different regions of the domain, allowing for finer discretisation near the swimmer. This size function is used to scale the stiffness of the bars. The Delaunay triangulation algorithm is then reused to determine the new edges of the mesh, and the procedure continues until no node moves more than a desired tolerance, relative to the local mesh size. This iterative procedure naturally lends itself to problems involving moving boundaries; by starting the procedure with a mesh from the previous time-step with boundary nodes set at the current time-step, the speed of mesh generation may be improved significantly.

The mesh is generated so that the elements have the Delaunay property (Delaunay, 1934), that no node lies within the circumcircle of any of the elements, as shown in figure 2.3. Delaunay meshes maximise the minimum angle over all elements in the mesh (Ho-Le, 1988).

The gradient of the error associated with interpolating the solution with basis functions depends linearly on the condition number of the elements (Ciarlet, 1978), that is, the condition number of the affine map from the element to a reference triangle (equation (2.19b)). Thus, avoiding slim elements produces a better approximation of the solution and so Delaunay meshes are desirable. The condition number of a triangle approaches infinity as any one of the internal angles approaches π , so maintaining mesh quality is very important.

Additionally, the error associated with interpolating the solution over any element is dependent on the square of the circumradius of that element (Ciarlet, 1978), and also how much the solution changes over that element. Thus, the accuracy of the finite element interpolated solution may be improved with mesh refinement. This can either be done globally, by remeshing the whole domain with a finer mesh, or locally. Local, or adaptive, mesh refinement is

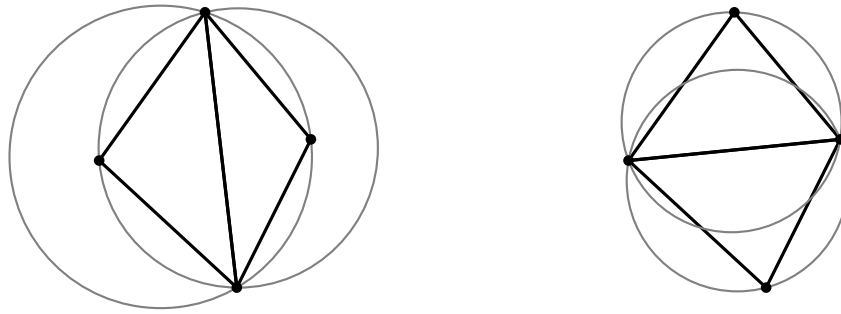


Figure 2.3: An example of a two node patch where the left-hand, non-Delaunay triangulation has undergone an edge-flipping routine to create the right-hand Delaunay triangulation.

achieved by first selecting the elements to refine, then updating these elements as shown in figure 2.4. Surrounding elements must also be updated in the manner indicated, to avoid hanging nodes; nodes that are not vertices in the triangulation. Nodes in the interior of the domain may then be shifted or edges flipped as shown in figure 2.3 in order to maintain the mesh quality.

Global refinement leads to a considerable increase in the size of the linear system to be solved. As such, local refinement is often preferable, since by focusing on regions where the solution quality needs the most improvement, one can achieve equivalent accuracy at lower computational cost. Local refinement is particularly appropriate when examining yield stress fluids, due to the sharp interface between unyielded regions of flow and liquid regions, the so-called ‘yield surface’. The positions of yield surfaces cannot be known a priori, and thus an adaptive procedure whereby the solution is refined locally where the velocity gradient is large is desirable.

We will approximate our velocity and pressure solutions as piecewise quadratic and piecewise linear polynomial functions over this triangulation. These are known as Taylor-Hood $P_2 - P_1$ triangular finite elements (Taylor and Hood, 1973). For a general triangle K with vertices (x_j, y_j) where $j = 1, 2, 3$, shown in figure 2.5, we associate linear shape functions

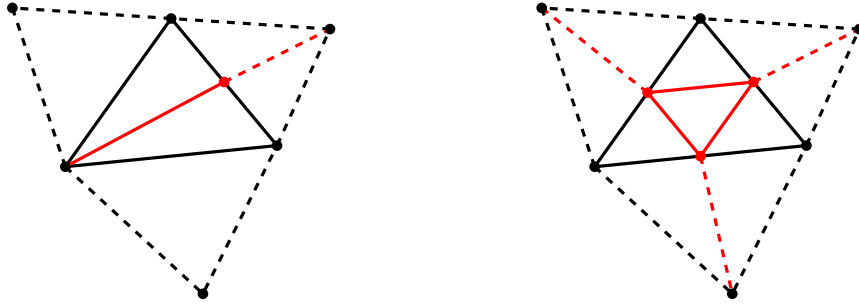


Figure 2.4: Two methods of locally refining the mesh corresponding to selecting an edge (left) and an element (right), where the new mesh edges arising from the refinement have been shown in red. We employ element selection in our refinement algorithm.

$N_j(x, y)$ with each of the vertices j via the property

$$N_j(x_k, y_k) = \delta_{jk}, \text{ for } j, k = 1, 2, 3, \quad (2.18)$$

so that each shape function takes the value of 1 at its associated vertex and linearly decreases to zero at the other two with the form $N_j(x, y) = a + bx + cy$, $x, y \in K$. Applying condition (2.18) gives values for a, b and c . The basis functions ϕ_j are then formed by combining the shape functions over patches, as shown in figure 2.6.

These basis functions are known as hat functions. Hat functions have compact support: they are zero on most of the domain. Thus, in the piecewise polynomial approximation of our solution, only the basis function at a particular node contributes to the solution at that point giving a sparse linear system. We may also construct quadratic, or indeed higher-order, shape functions by the same procedure.

Rather than calculate the shape functions for each element in the mesh, we use the affine mapping

$$\xi = [(y_3 - y_1)(x - x_1) - (x_3 - x_1)(y - y_1)]/\mathcal{J} \quad (2.19a)$$

$$\eta = [(y_1 - y_2)(x - x_1) - (x_1 - x_2)(y - y_1)]/\mathcal{J} \quad (2.19b)$$

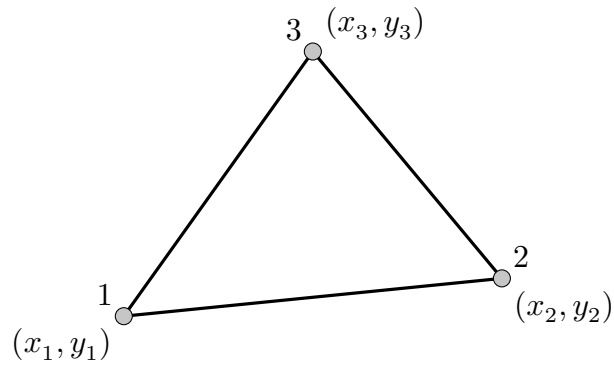


Figure 2.5: A linear triangular element with anticlockwise local node numbering.

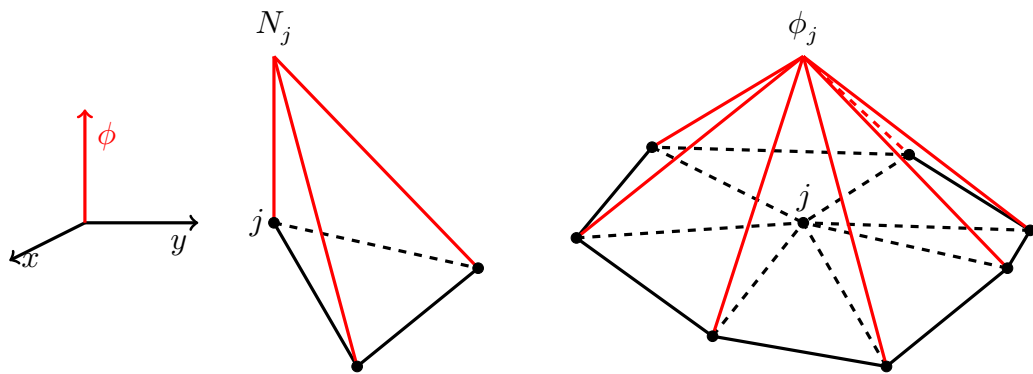


Figure 2.6: A linear shape function (red) plotted over a single element (left) together with the associated linear hat function (red) plotted over the patch of neighbouring elements (right).

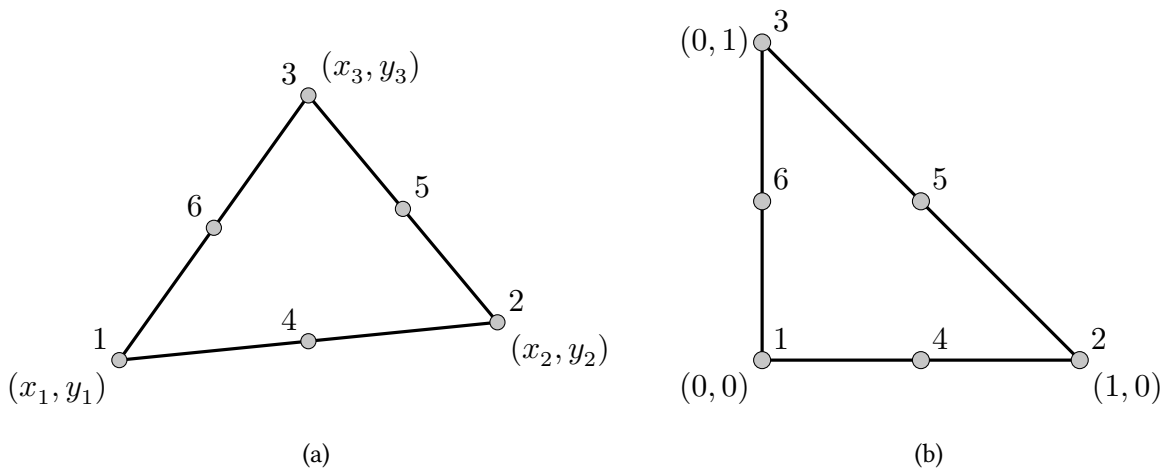


Figure 2.7: (a) A quadratic triangle, with anticlockwise node numbering. Note that since we wish to model fluid pressure with linear elements and the velocity with quadratic elements, the first three quadratic nodes coincide with the linear triangle. (b) The Canonical Triangle.

to map each element K to the canonical triangle E (Strang and Fix, 1988), shown in figure 2.7b. Here, (x, y) are the coordinates of triangle K with vertices (x_i, y_i) , and \mathcal{J} is the Jacobian of the inverse transformation. Over the canonical triangle, the piecewise linear shape functions for the pressure approximation are given by

$$\hat{N}_1^1(\xi, \eta) = 1 - \xi - \eta, \quad (2.20a)$$

$$\hat{N}_2^1(\xi, \eta) = \xi, \quad (2.20b)$$

$$\hat{N}_3^1(\xi, \eta) = \eta, \quad (2.20c)$$

and the piecewise quadratic shape functions for the velocity approximation are given by

$$\hat{N}_1^2(\xi, \eta) = 2\xi^2 + 2\eta^2 - 3\xi - 3\eta + 4\xi\eta + 1, \quad (2.21a)$$

$$\hat{N}_2^2(\xi, \eta) = 2\xi^2 - \xi, \quad (2.21b)$$

$$\hat{N}_3^2(\xi, \eta) = 2\eta^2 - \eta, \quad (2.21c)$$

$$\hat{N}_4^2(\xi, \eta) = 4(1 - \xi - \eta)\xi, \quad (2.21d)$$

$$\hat{N}_5^2(\xi, \eta) = 4\xi\eta, \quad (2.21e)$$

$$\hat{N}_6^2(\xi, \eta) = 4(1 - \xi - \eta)\eta, \quad (2.21f)$$

where the subscripts denote the node at which each polynomial takes a value of 1. These functions are integrated with a 12–point two dimensional quadrature rule, the points and weights of which are given in Strang and Fix (1988).

The velocity solution is given by a piecewise quadratic function over the domain, output at the 6 nodes of each quadratic element. Thus, to calculate the velocity at a general point (x_0, y_0) in D not corresponding to a node it is necessary to project the velocity at that point onto the finite element solution. To do this, we first calculate the element in which the point is contained, then map the containing element to the canonical triangle E using (2.19b), giving

the coordinates (ξ_0, η_0) of the point (x_0, y_0) within E . The x -velocity, say, at (x_0, y_0) is then found by

$$u_1(x_0, y_0) = \{u_1\}_{K(1)}N_1^2(\xi_0, \eta_0) + \{u_1\}_{K(2)}N_2^2(\xi_0, \eta_0) + \{u_1\}_{K(3)}N_3^2(\xi_0, \eta_0) \\ + \{u_1\}_{K(4)}N_4^2(\xi_0, \eta_0) + \{u_1\}_{K(5)}N_5^2(\xi_0, \eta_0) + \{u_1\}_{K(6)}N_6^2(\xi_0, \eta_0), \quad (2.22)$$

where $K(i), i = 1, 2, \dots, 6$ is the global index of the nodes of triangle K , which are ordered locally by i . With this framework in place, we will now test the accuracy of the method of femlets.

2.2 Testing the method of femlets

In this section, we will perform a number of tests to validate the method of femlets. We will begin by comparing our generalised Stokes solver against analytic solutions for flow in a two dimensional channel in the absence of femlets, and then compare the flow arising in a cavity from a moving lid on which we apply Dirichlet boundary conditions, and a line distribution of femlets. We will then discuss the choice of femlet cut-off function g^ϵ whilst examining how the no-slip condition is conserved along a line distribution of femlets representing a beating filament. Finally, we will discuss the accuracy of the time stepping procedure used to advance the swimmer through the domain.

2.2.1 Validating the generalised Stokes flow solver: channel flow

We begin by modelling two dimensional flow driven down an infinite channel channel by a pressure gradient, due to the existence of quantitatively different analytic solutions for Newtonian, power law and Papanastasiou fluids. Unfortunately, no analytic solution exists for Carreau fluid, though the rheological similarity of the Carreau and Papanastasiou constitutive

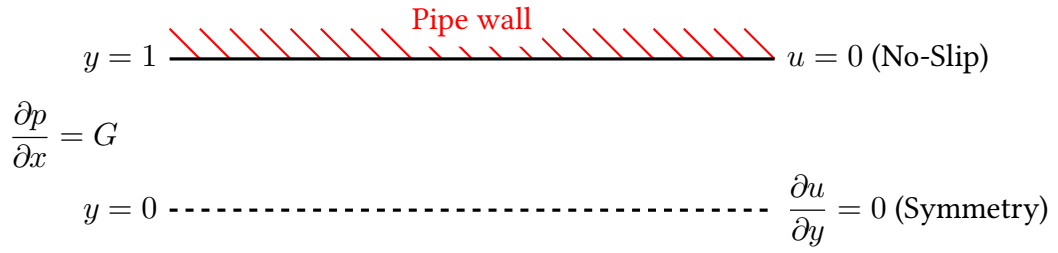


Figure 2.8: The conditions under which analytic solutions of flow down an infinite channel are derived.

laws suggests that numerically calculated profiles should be qualitatively similar.

Consider flow within the infinite no-slip walls $y = [-1, 1]$ driven by a constant pressure gradient G (figure 2.8). Since the channel is infinite in the x -direction, $\mathbf{u} = (u(y), 0)$, so that $\nabla \cdot \mathbf{u} = 0$ holds automatically. From the momentum equation,

$$\nabla \cdot \boldsymbol{\sigma} = 0 \quad (2.23)$$

$$\therefore \nabla \cdot (-p\mathbf{I} + \boldsymbol{\tau}) = 0. \quad (2.24)$$

The boundary conditions are symmetric about $y = 0$, and hence we seek a symmetric form for the solution. Furthermore, we must have $\partial u / \partial y = 0$ at $y = 0$, since otherwise there would be a cusp at the centre of the flow. Thus

$$Gy = \tau_{12} \quad (2.25)$$

For Newtonian fluids, $\tau_{12} = \mu_0(du/dy)$, so that

$$Gy = \mu_0 \frac{du}{dy} \quad (2.26)$$

$$\therefore u = \frac{G}{2\mu_0}(y^2 - 1). \quad (2.27)$$

For power law fluids, $\tau_{12} = \mu_0 (du/dy)^n$, so that,

$$Gy = \mu_0 \left(\frac{du}{dy} \right)^n \quad (2.28)$$

$$\therefore u = \left(\frac{G}{\mu_0} \right)^{1/n} \frac{n}{n+1} (y^{1+1/n} - 1). \quad (2.29)$$

Finally, for Papanastasiou fluids, $\tau_{12} = \mu_\infty du/dy + \tau_y (1 - \exp[-m(du/dy)])$. Rewriting the solution of You et al. (2008) in terms of the physical parameters G, μ_0, μ_∞ and τ_y , and defining $\mu_{\text{rat}} = (\mu_0 - \mu_\infty)/\mu_\infty$, we obtain

$$u = \frac{-\tau_y^2}{G\mu_\infty\mu_{\text{rat}}^2} \left[W(\mu_{\text{rat}} \exp[\mu_{\text{rat}}(1 - Gy/\tau_y)]) + \frac{1}{2} W(\mu_{\text{rat}} \exp[\mu_{\text{rat}}(1 - Gy/\tau_y)])^2 \right] - \frac{\tau_y}{\mu_0} y + \frac{G}{2\mu_\infty} y^2 + C, \quad (2.30)$$

for C the constant of integration,

$$C = \frac{\tau_y^2}{G\mu_\infty\mu_{\text{rat}}^2} \left[W(\mu_{\text{rat}} \exp[\mu_{\text{rat}}(1 - G/\tau_y)]) + \frac{1}{2} W(\mu_{\text{rat}} \exp[\mu_{\text{rat}}(1 - G/\tau_y)])^2 \right] + \frac{\tau_y}{\mu_0} - \frac{G}{2\mu_\infty}, \quad (2.31)$$

and W the Lambert W function (Corless et al., 1996), which satisfies the equation

$$y = W(y)e^{[W(y)]}, \quad (2.32)$$

and hence is also known as the product logarithm.

These analytic solutions are valid for an idealised infinitely long channel. In practice, the computational domain must be truncated. On the downstream open end we apply the zero normal stress boundary condition (2.5), and we extract the finite element solution along the slice $x = 0$, midway along the channel. In this way, flow effects from the imposition of

boundary conditions at either end are negligible, provided the channel is sufficiently long.

Numerical simulation of channel flow

Channel flow has no immersed forces driving it. As such, this initial testing is done without femlets, in order to first verify the generalised Stokes flow solver against the above analytic solutions, before later considering femlets. The fluid domain is the rectangle $(-5, 5) \times (-1, 1)$, and the boundary at $x = -5$ is treated as a Dirichlet boundary with the equivalent analytic solution prescribing the inflow velocity. The numerical velocity solution u_{num} is calculated along the line $x = 0$, the relative error from the analytic solution u_a ,

$$\text{err} = \frac{\|u_{\text{num}} - u_a\|_2}{\|u_a\|_2}, \quad (2.33)$$

in the 2–norm is calculated for a series of meshes with increasing degrees of freedom. The numerical solution for the pressure is similarly calculated along the line segment $x = (-1, 0)$, $y = 0$ and the relative error from the constant pressure gradient solution calculated.

For Stokes flow, the underlying analytic solution is quadratic. Thus, no approximation is made in modelling the solution space with piecewise quadratic basis functions and we expect our $P_2 - P_1$ finite element solution to be exact irrespective of the degree of mesh refinement. For all meshes of 840, 1268, 2270, 4540, 9342 and 16777 degrees of freedom, the relative error err in the calculated solution is $\mathcal{O}(10^{-15})$, the working precision of Matlab[®]. The pressure solution is similarly exact to within working precision.

For power law flow, the constitutive law breaks down as the shear rate approaches zero or infinity (Elias et al., 2006). At zero shear rate, power law fluids have infinite viscosity, which is unphysical. However, the underlying laminar solution for flow down a channel has zero shear rate at the centre of the channel. The Picard solver will fail to converge in this case, since in the small region around the centre of the channel the numerical scheme will not be able to

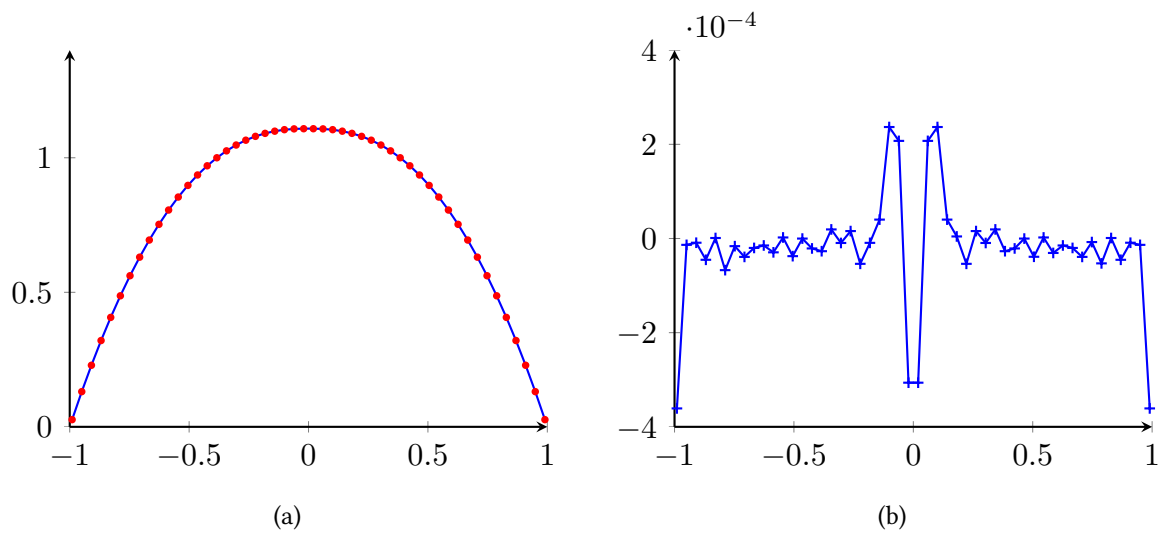


Figure 2.9: (a) The numerical (red) and analytic (blue) solutions for shear thinning power law flow down a pipe evaluated at 50 evenly spaced points for a mesh with 19702 degrees of freedom and (b) the relative error of the numerical solution. The power law index $n = 0.7$.

capture this singularity.

Instead, the singularity is blurred over the mesh, and successive iterations will alternate between overestimating the velocity of the fluid at the centre and then underestimating it. However, the scheme converges to the analytical solution everywhere else in the flow for values of the power law exponent $n \geq 0.5$, and the scheme still produces a good approximation to the analytic solution, shown in figure 2.9 if the Picard iteration is allowed to continue for 25 iterations, whereupon in all cases the error had already begun to oscillate around a value $\sim 10^{-2}$. Because of the issue with non-convergence at zero shear rate, and because biological shear-thinning fluids are better described by the Carreau law, we will not consider power law fluids further.

For Papanastasiou flow with $\mu_0 = 1, \mu_\infty = 0.5$ and $\tau_y = 2$ giving $m = 1$, the maximum relative errors in the flow and pressure numerical solutions as a function of the number of degrees of freedom solved for are given in table 2.1, showing that our scheme converges satisfactorily for the Papanastasiou constitutive law. The greatest error is incurred where the

Papanastasiou fluid		Carreau fluid		
D.o.F.	Err flow ($\cdot 10^{-3}$)	Err press ($\cdot 10^{-4}$)	Ref (h)	Diff ($\cdot 10^{-3}$)
840	0.488	0.150	1	0.504
1268	0.240	0.239	2	0.262
2270	0.0886	0.0575	3	0.0934
4540	0.0321	0.00114	4	0.0331
9342	0.00919	0.00279	5	0.00967
16777	0.00397	0.000163		

Table 2.1: The error in calculated flow and pressure solutions for Papanastasiou flow down a channel as a function of the number of degrees of freedom solved for and the difference between solutions of Carreau flow down a channel for successive refinements of the mesh, where $h = 1$ corresponds to the difference between the solution for 1268 D.o.F. and 840 D.o.F., $h = 2$ the difference between 2270 D.o.F. and 1268 D.o.F. etc.

shear rate varies most quickly, suggesting that adaptive mesh refinement in these regions may improve solution quality without too great an increase in numerical cost.

Whilst there is no available analytic solution against which to compare our numerical solution for Carreau flow in a channel, the rheological similarity between Carreau and Papanastasiou fluids suggests that since the scheme is convergent for Papanastasiou flow it will also converge for Carreau flow for rheological parameters in a similar range. Furthermore, we may test convergence by evaluating the relative difference in the 2–norm between solutions for successive refinements of the mesh, shown in table 2.1 for the case where $\mu_0 = 1$, $\mu_\infty = 0.5$, $\lambda = 1$ and $n = 0.5$. Having established the convergence of our generalised Newtonian flow solver for rheological parameters within these values, we will now consider suitable choices of femlet cut-off function, and the convergence of femlet solutions to equivalent solutions driven by Dirichlet boundaries.

2.2.2 The choice of cut-off function

In the method of femlets, moving boundaries, such as immersed filaments, are represented by distributions of regularised body forces driving the fluid. This raises the question of what properties are desirable for a given cut-off function $g^\epsilon(\mathbf{x}_k^{\text{loc}})$ to produce a good representation of the moving boundary. The force envelope representing the boundary is given by the superposition of cut-off functions $G = \sum_{k=1}^{N_f} g^\epsilon(\mathbf{x}_k^{\text{loc}})$ and the effect of the boundary's motion on the fluid is captured by the a priori unknown femlet forces, or weights, f_k .

Good choices of cut-off function should therefore generate an approximately constant force envelope along the line representing the boundary, which should only change by a small amount if the spacing between femlets changes. We will refer to this as the resolution property of femlets. Furthermore, given this smooth force envelope, the femlet weights should allow good interpolation of the underlying Dirichlet velocity conditions on the boundary being modelled. Note that the numerical scheme ensures that, at the location of the femlets, the Dirichlet velocity condition is imposed exactly. Thus, this property refers to points between the femlets on the underlying boundary being modelled. We will refer to this as the interpolation property of femlets.

These properties are coupled: the resolution property, shown in figure 2.10, ensures that the force driving the fluid changes smoothly between femlets, helping to preserve the Dirichlet velocity conditions at all points on the moving boundary, rather than just at the centroid of each femlet. The interpolation property gives information about the minimum number of femlets required to effectively capture the Dirichlet velocity conditions on the moving boundary. To illustrate these ideas, we first consider some one dimensional femlets, before proceeding to analysis in two dimensions.

The most simple candidate for a choice of cut-off function, inspired by the finite element

method, is the linear hat function, given in one dimension by

$$g^\epsilon(\mathbf{x}_k^{\text{loc}}) = \begin{cases} 1 - \frac{x_k^{\text{loc}}}{\epsilon} & \text{if } x_k^{\text{loc}} \leq \epsilon, \\ 0 & \text{otherwise.} \end{cases} \quad (2.34)$$

If each femlet is spaced exactly ϵ apart, the superposition function G is constant between all femlets, decreasing linearly to zero at either end over a distance of ϵ (figure 2.10a). Hat functions have compact support, and the δ interpolation property. This means that the calculated weights for interpolating a given function are independent of the weights at other nodes, and that the function will be interpolated piecewise linearly (figure 2.11a). However, it should be noted that Hat functions do not respect all aspects of the resolution property, since a small change in the position of a given femlet leads to $\mathcal{O}(1/\epsilon)$ changes in the gradient of G as shown in figure 2.12a, and destroys the δ property for the adjacent femlets. Thus, when modelling boundaries with hat femlets it is important to ensure that they are evenly spaced, although the error in the flow solution will be less than that shown in figure 2.12a owing to the smoothing effect of viscous dissipation.

For the two dimensional analogue of these hat functions, we define the ellipse

$$R^{\text{loc}} = \frac{\sigma_x \sigma_y}{\sqrt{(\sigma_y \cos \theta^{\text{loc}})^2 + (\sigma_x \sin \theta^{\text{loc}})^2}}, \quad (2.35)$$

where as with the Gaussian femlets (2.6) the small parameter ϵ has been absorbed into the semi-axes σ_x, σ_y . We then define the function

$$g^\epsilon(\mathbf{x}_k^{\text{loc}}) = \begin{cases} 1 - \frac{r^{\text{loc}}}{R^{\text{loc}}} & \text{if } r^{\text{loc}} \leq R^{\text{loc}}, \\ 0 & \text{otherwise,} \end{cases} \quad (2.36)$$

that decreases linearly from 1 at the centre of the ellipse and 0 at its edge. For representing straight lines, a spacing of $\epsilon \sigma_x$ between femlets gives a representation with the desired

properties. However, for representing curved boundaries, such as an immersed filament, the resolution property will not be respected unless $\sigma_x = \sigma_y$, which gives a piecewise linear representation of the boundary with equal segment lengths. This requirement entails that a larger number of femlets are required to model a given curved boundary, however hat functions are a viable choice of cut-off function. Femlets with this choice of cut-off function will hereafter be referred to as Hat femlets.

Another possible choice of cut-off function is the Gaussian (2.6), given in one dimension by

$$g^\epsilon(\mathbf{x}_k^{\text{loc}}) = \exp\left[-\frac{(x_k^{\text{loc}})^2}{2\epsilon^2}\right], \quad (2.37)$$

which is often used as a regularisation of the Dirac δ function. Rayleigh's criterion for resolving distinct Gaussian sources entails that these sources must be further apart than $\sqrt{2}\epsilon$ in order to observe them. At this distance, the maximum of a Gaussian of height 1 will coincide with its neighbours when they are at height $1/e$ (Cywiak et al., 2001). Thus, a spacing of $\Delta < \sqrt{2}\epsilon$ between gaussian femlets also gives an approximation to the square wave, which improves as $\epsilon \rightarrow 0$ (figure 2.10b). Note that while these functions are interpolating, they do not have the δ property in that the velocity at adjacent femlets will also contribute when calculating the weighting required to respect the Dirichlet velocity conditions on the moving boundary.

Two advantages of Gaussian femlets over Hat femlets are that they have the resolution property for all spacings $< \sqrt{2}\epsilon$ and that small changes to these spacings only have a small effect on G and its gradient (figure 2.12a). Consequently, provided the radius of curvature of a curved boundary, say an immersed filament, does not change too quickly, a set of two dimensional elongated Gaussians given by equation (2.6) provides a good approximation of the boundary. Additionally, Gaussian femlets may provide a smoother interpolation of the underlying velocity field (figure 2.11b), though the absence of the δ property entails that they are associated with greater 'end errors' in this interpolation, particularly if the underlying velocity function is non-zero at the end of the boundary we wish to model (figure 2.12b). Thus,

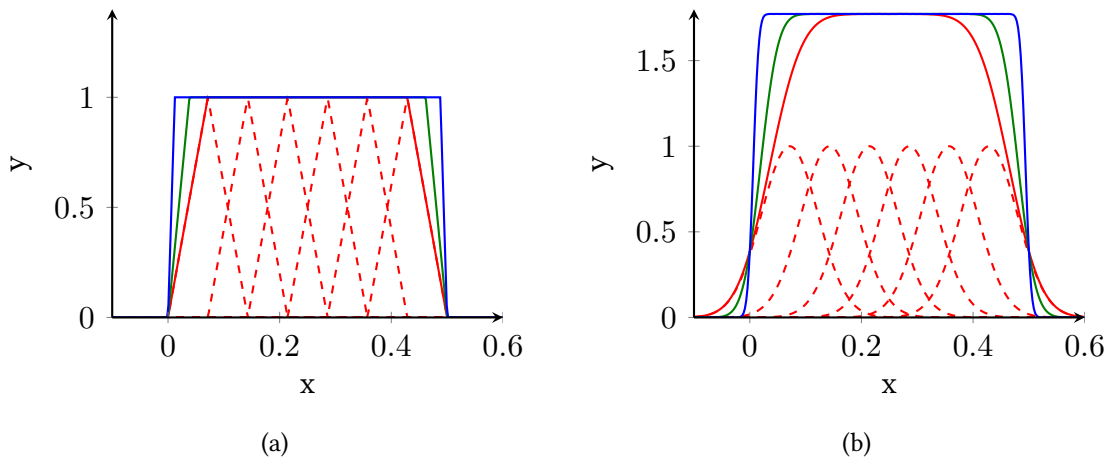


Figure 2.10: Approximations to the square wave on the interval $[0, 0.5]$ formed by superposing 10 (red) 20 (green) and 40 (blue) hat functions (a) and Gaussians (b).

whilst Gaussian femlets will be preferred for modelling swimmers such as squirmers that have a smooth velocity over a continuous surface such as a circle, Hat femlets may provide a better model for beating filaments.

In order to capture the shape of the cut-off function in a finite element framework, we refine the mesh locally around each femlet and project the cut-off function onto the finite element space using P_2 quadratic basis functions. It is important to be aware of the error associated with this projection. Hat femlets are interpolated exactly by quadratic functions, and so any error is associated with no coincidence of mesh nodes with the ellipse R . For Gaussians, the gradient of the function varies most rapidly within one standard deviation, and we find that specifying a maximum mesh size of $\sigma_y/2$ within a radius of σ_x adequately resolves the function. This is also adequate for Hat femlets.

Femlet solutions vs Dirichlet boundaries

Since the method of femlets represents the action of Dirichlet boundaries through a distribution of femlets, we must test whether this approximation is valid by comparing flow driven by femlets and Dirichlet boundaries. Thus, we will now consider the flow in a cavity driven

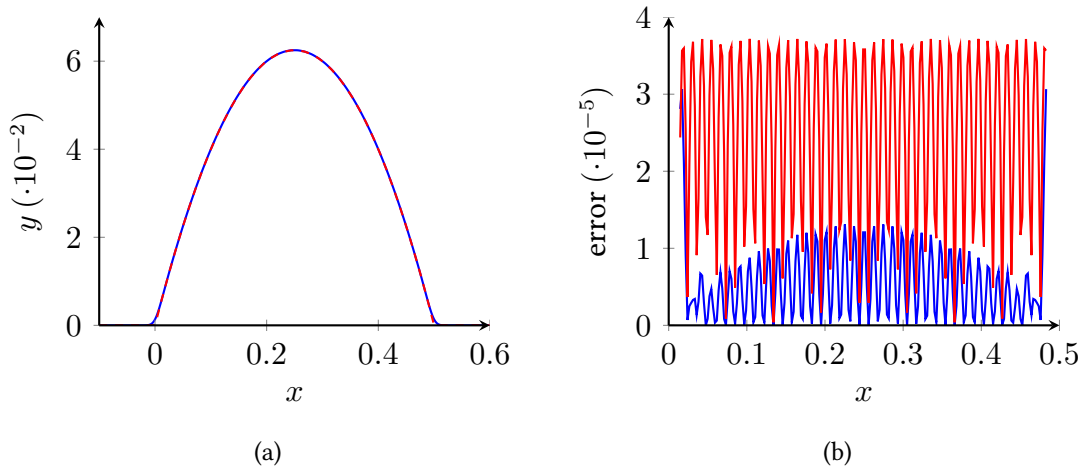


Figure 2.11: (a) Interpolation of the function $y = -x(x - 0.5)$ on the interval $[0, 1]$ by 40 Gaussian (blue, solid) and Hat (red, dashed) femlets and (b) the relative error associated with these interpolations within the region where Gaussian femlets have the interpolation property.

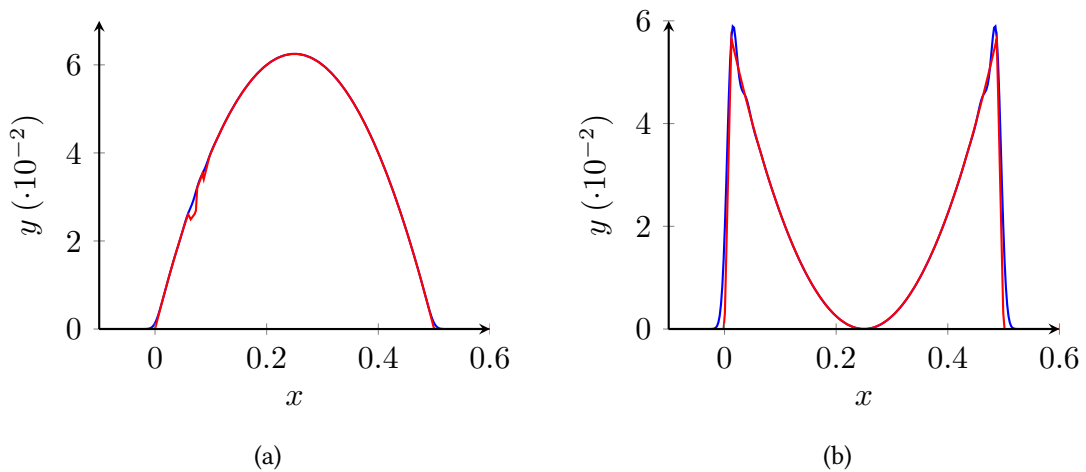


Figure 2.12: (a) The interpolation of the function $y = -x(x - 0.5)$ if a single femlet is shifted by approximately 8% of the optimal spacing, showing sharp gradients in the interpolation by Hat femlets (red) and little change in the interpolation by Gaussian femlets (blue). (b) The 'end errors' associated with interpolating a function that is non-zero at the edge of the femlets, showing errors for the Gaussian propagating further into the interpolation.

by a moving lid. The domain D is the square $(0, 1)^2$, and the no-slip condition is applied on the three lower stationary walls. On the upper wall, we apply the Dirichlet velocity condition $\mathbf{u} = (-x(x - 1), 0)$. The resultant flow is shown for the case of Stokes fluid in figure 2.13a. We will compare solutions of Stokes flow generated by both a Dirichlet boundary and a line distribution of femlets modelling the upper wall. In the femlet case, a mirror domain is placed above the driving wall, so that the fluid domain is the rectangle $(0, 1) \times (0, 2)$.

For 10, 15, 20, 30 and 40 femlets, the velocity of the flow along the line $y = 1$, which represents the Dirichlet boundary, was sampled at 500 points. Crucially, this means the velocity was sampled not only at the centroid of each femlet, but also at points between the femlets, for which $\sigma_y = 0.01$ and σ_x is chosen so that for each density of femlets along the line, the resolution property is preserved. Table 2.2a shows the relative error in the flow at these points when compared to the equivalent Dirichlet conditions. The error is maximum near the corners $(0, 1)$ and $(1, 1)$, since the femlets do not reach the very edges of the domain. The error shown in table 2.2a is calculated in the interpolating region of the femlets, i.e. the region where the sum of their cut-off functions is constant, and so does not include these end errors. This is because when modelling an immersed swimmer, there will be no boundary conditions that lie outside the interpolating region of the femlets.

The error is roughly inversely proportional to the number of femlets used in the representation, so that the error is linearly dependent upon the spacing between femlets. Gaussian femlets provide greater accuracy, however for 40 femlets per unit length, the relative error in the boundary condition is $\mathcal{O}(10^{-4})$, and we conclude that that this provides a satisfactory representation of the moving boundary for both types of femlet.

For 40 femlets, we then maintained σ_x as this is contingent on the femlet spacing Δ , whilst incrementally reducing σ_y to give an increasingly sharp approximation of the Dirichlet boundary. The flow velocity was sampled at 500 points along the line $x = 0.5$, where its variance is greatest. Table 2.2b shows the relative error in the femlet solution as σ_y is decreased, demon-

strating linear convergence.

However, closer examination of the resultant flow near the femlet boundary $y = 1$ shows that the effect of σ_y regularisation is to push the boundary condition further out into the flow (figure 2.13b). In the near-field of the femlets, yet outside the envelope of their forcing, we may examine the y -values at which a given velocity occurs as a function of σ_y . This gives an effective radius r_{eff} for the femlet. By shifting the femlet boundary up a distance r_{eff} , the near-field of the flow is much better matched to the Dirichlet case. The effective radii for hat and Gaussian femlets are given by

$$r_{\text{eff}}^h \approx \frac{\sigma_y}{3}, \quad r_{\text{eff}}^g \approx \frac{2\sqrt{2 \ln 2} \sigma_y}{3}, \quad (2.38)$$

which in both cases is a third of the function's Full Width at Half Maximum (FWHM), the distance between the two extreme values at which the cut-off function is half maximum. This effective radius is largely insensitive to rheology for the flow parameters that we will consider. Figure 2.14a shows the value of the ratio $r_{\text{eff}}^g/\text{FWHM}$ for Gaussian femlets with $\sigma_y = 0.01$ in Carreau fluid as a function of the power law index n . Thus, the effective radius of the femlets increases with fluid thinning, however the change is around 7%, which when modelling sperm flagella equates to measuring the width of the flagellum to within around 70 nm. Therefore, we can discount the dependence of r_{eff} on fluid rheology.

Whilst this upwards shift better approximates the flow in the near-field, by conservation of mass it must increase errors in the far-field: since more flow is being driven to the right, the position and speed of the return flow will be altered. However, this effect is not present when considering filaments in open channels, which will be modelled in the next section where we represent slender filaments by femlets with an effective radius equal to the width of the filament.

Number of femlets	Error ($\cdot 10^{-3}$)		σ_y	Error	
	Gaussian	Hat		Gaussian	Hat
10	0.889	2.71	0.1	0.0608	0.0255
15	0.394	1.95	0.09	0.0547	0.0230
20	0.267	1.56	0.08	0.0487	0.0207
30	0.1645	1.16	0.07	0.0426	0.0181
40	0.121	0.931	0.06	0.0366	0.0157
			0.05	0.0307	0.0132

(a) (b)

Table 2.2: (a) Errors in the no-slip condition on the upper wall of a regularised driven cavity when that wall is modelled as a line distribution of varying numbers of Gaussian and Hat femlets with $\sigma_y = 0.01$. (b) Errors along the line $x = 0.5$ in the calculated flow in a regularised driven cavity where the upper wall is modelled as a line distribution of 40 femlets of increasing sharpness.

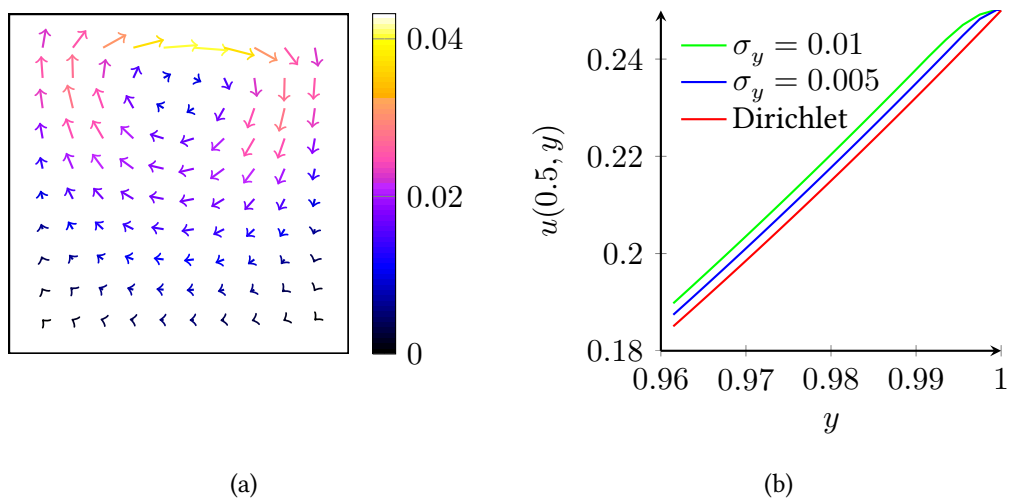


Figure 2.13: (a) Stokes flow in a two dimensional enclosed cavity driven by a regularised moving lid. Arrow lengths and colour denote the fluid speed. (b) Plot showing the x -component of the flow velocity on the slice $x = 0.5$ near the moving lid, showing convergence onto the Dirichlet solution (red) as σ_y is decreased from $\sigma_y = 0.01$ (green) to $\sigma_y = 0.05$ (blue) for Gaussian femlets. Note that the effective radius of the femlets is given by an average in the near-field of the distances at which the femlet velocity is equal to the Dirichlet. Shifting the femlets upwards by the effective radius causes these lines to essentially overlap.

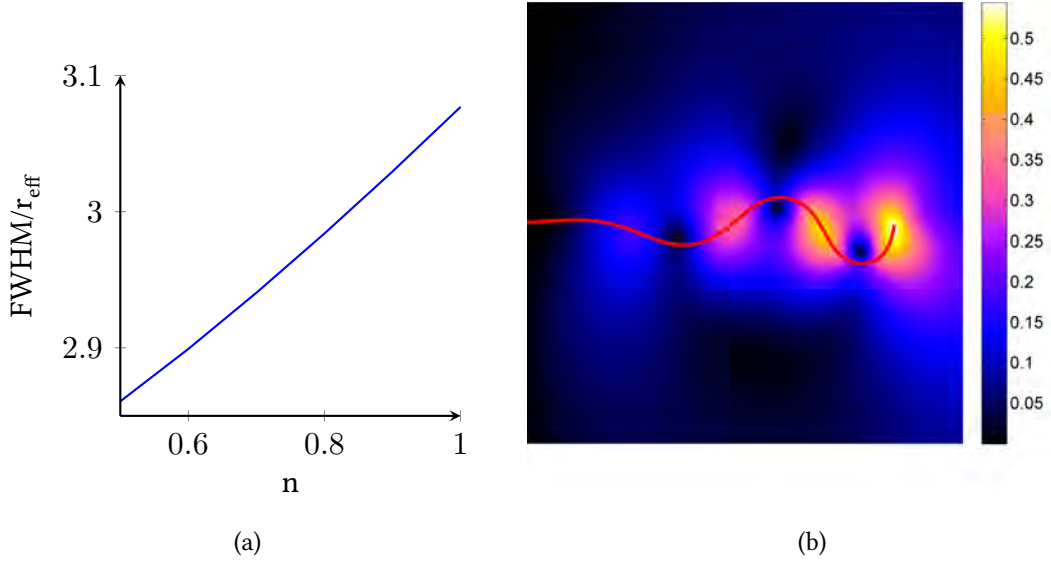


Figure 2.14: (a) The effective radius of Hat femlets modelling a driven cavity as a function of the power law index n and (b) the speed of fluid driven by a beating filament as given by equation (2.39)

The preservation of the no-slip condition on a beating filament

We will now examine the beating of a filament of unit length protruding from the lower wall in a cavity with sides of length 5 with an open lid. The outer boundary is treated as a zero normal stress boundary, whilst the other three walls are given the no-slip condition.

We parameterise the flagellum in terms of its shear (tangent) angle $\psi(s, t)$, given in the body frame. By integrating along the tangent vector of the filament, its centreline may be calculated in the body frame

$$\boldsymbol{\xi}(s, t) = \boldsymbol{\xi}_0 + \int_0^s [\cos(\psi(s', t)), \sin(\psi(s', t))]^T ds', \quad (2.39)$$

where s, t are the length along the filament and time respectively. The centreline velocity of

the filament in the body frame is then

$$\dot{\boldsymbol{\xi}}(s, t) = \int_0^s [-\sin(\psi), \cos(\psi)]^T \dot{\psi} ds'. \quad (2.40)$$

Points on the surface $\boldsymbol{\xi}(s, t)$ of a finite width two dimensional filament and the corresponding velocity are then given by

$$\boldsymbol{\Xi}(s, t) = \boldsymbol{\xi}(s, t) \pm a\mathbf{n}, \quad \dot{\boldsymbol{\Xi}}(s, t) = \dot{\boldsymbol{\xi}}(s, t) \pm a\dot{\mathbf{n}} \quad \mathbf{n} = [-\sin(\psi(s', t)), \cos(\psi(s', t))], \quad (2.41)$$

for a the filament radius. We prescribe a shear angle of the form

$$\psi(s, t) = Cs \cos(ks - \omega t), \quad (2.42)$$

which represents a bend propagating down the filament, steepening towards the less stiff distal end with a linear envelope. Note that since this filament is pinned, the body frame and lab frame are coincident in this case. This parameterisation will be used in section 3.4 to model human sperm flagella.

The slenderness ratio of human sperm flagellum is approximately 1:50, that is, its length is $\approx 50 \mu\text{m}$ and its diameter is $\approx 1 \mu\text{m}$. Thus, when modelling a sperm flagellum with femlets, we match the effective radius of the femlets to this slenderness ratio. For Hat femlets, this implies

$$\frac{\sigma_y^h}{3} \approx \frac{1}{100}, \quad \therefore \sigma_y^h \approx 0.03. \quad (2.43)$$

As we have already seen, Hat femlets only make a good choice provided the femlet spacing is exactly correct. Thus, we will model the filament as a set of piecewise linear sections of length 0.03, using 33 radially symmetric Hat femlets. For Gaussian femlets, we have

$$\frac{2\sqrt{2 \ln 2} \sigma_y^h}{3} \approx \frac{1}{100}, \quad \therefore \sigma_y^h \approx \frac{1}{80}. \quad (2.44)$$

Thus, the filament may also be modelled with 40 Gaussian femlets with $\sigma_x/\sigma_y = 2$, corresponding to the sperm modelling presented in Montenegro-Johnson et al. (2013, 2012). We will also model the filament with 80 Gaussian femlets, to examine the effect that elongation has on the forces calculated and the end errors incurred. Note that since Gaussian femlets do not require exact positioning to produce good interpolations, we may place them at equal points along the arclength of the filament, rather than given equal Cartesian spacing. This saves the need to numerically invert equation (2.39).

Figure 2.14b shows the speed of the fluid surrounding the filament at time $t = 0$ for maximum shear angle $A = 0.45\pi$ and wavenumber $k = 2.5 \times 2\pi$. Upon examining the no-slip condition on the filament's centreline, the v -component error of which is shown in figure 2.15a, we see that both Gaussian and Hat femlets give a good representation of the analytic value of the no-slip condition, the differences being very small. Furthermore, upon examining the projected velocity solution at points on the bottom edge of the equivalent finite width filament 2.15b, we see good qualitative agreement between the femlet solution and the equivalent Dirichlet surface velocity. In both cases, the velocity is better represented by Gaussian femlets, and as such we will use these exclusively henceforth.

2.2.3 Accuracy of the time stepping procedure

To predict the path of the swimmer as it moves through the fluid, we require an explicit time stepping procedure, for which we choose the Adams-Bashforth multistep method (Bashforth and Adams, 1883; Iserles, 2009). For the third order scheme we employ, the swimmer's position is calculated by extrapolating a cubic through the current and previous 2 values of translational and angular velocity. The method incurs no more numerical cost than a forwards Euler scheme, yet the error in the solution of the n -step method decays as $\mathcal{O}(\Delta t^n)$ (Iserles, 2009) for time step Δt .

At each step, the coordinates of the swimmer in the body frame are rotated by an angle

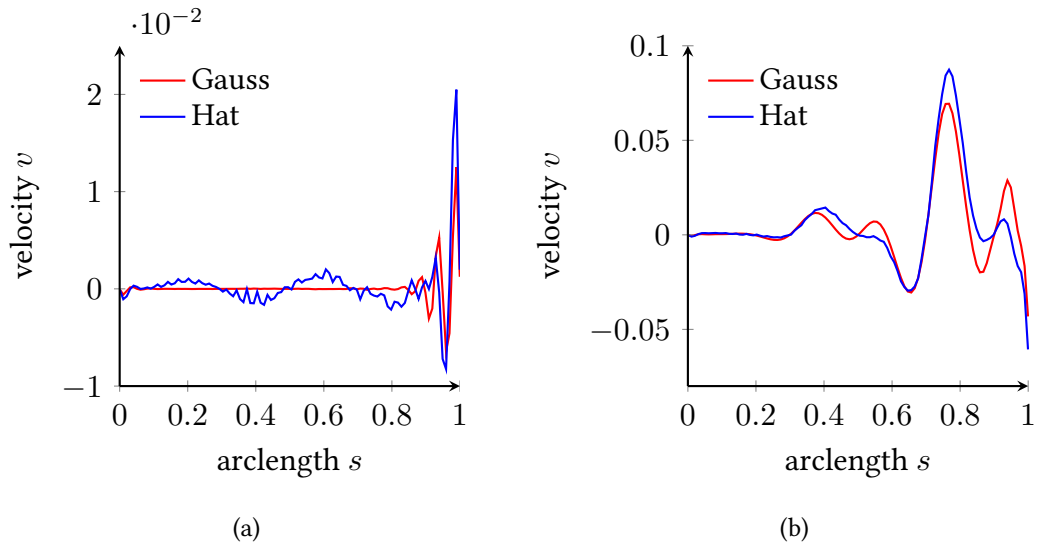


Figure 2.15: (a) The relative error in the y -component of the fluid velocity along the centreline of the flagellum as a function of arclength, s , for Gaussian (red) and Hat (blue) femlets. (b) The error in the y -component of the velocity on the lower 'surface' of the filament, taken at the femlets effective radius, for Gaussian (red) and Hat (blue) femlets, showing good qualitative representation of a finite width filament by femlets, with Gaussian femlets providing greater accuracy.

θ given by solving $\dot{\theta} = \Omega(t)$ with the third order Adams-Bashforth scheme then translated by solving $\dot{\mathbf{x}} = \mathbf{U}(t)$ in the same manner. For a two dimensional sperm in a channel filled with Newtonian fluid, we found only a 0.0431% change in the position of the swimmer after a single beat cycle between 40 and 80 steps per beat. Since this is of the same order as the error associated with the imposition of the no-slip condition by the femlets, we use the third order scheme with 40 steps per beat.

Chapter 3

Does shear dependent viscosity aid microscopic swimming?

3.1 Introduction

We will now use the method of femlets to examine the effects of shear dependent viscosity on swimmers with prescribed beat kinematics. Results will be obtained for swimmers in Carreau fluids, and the effects of varying the viscosity ratio μ_0/μ_∞ , the power law index n and the Deborah number $De = \lambda\omega$ will be examined. These parameters will be varied smoothly from the Newtonian case, to which the Carreau viscosity law reduces if $\mu_0/\mu_\infty = 1, n = 1$ or $De = 0$.

Swimmers will exhibit prescribed beat kinematics, so that their configuration in the body frame is given by a prescribed function of time. The body frame velocity, applied at the location of each femlet, will then be given by the time derivative of this function. In order to understand the effects of shear-thinning, we will examine the velocity, progress and trajectories of three qualitatively different classes of model swimmer as $\mu_0/\mu_\infty, n$ and De are varied. The first class of swimmers comprise sliding, collinear spheres which swim through utilising the reduction in drag experience by these spheres as they move into one another's slip stream. The second class of swimmers, the squirmers, is inspired by ciliated swimmers. The squirmers we will

consider are rigid bodies where the effects of coordinated ciliary action have been incorporated through a surface slip velocity. Finally, we will examine monoflagellate pushers exhibiting waveforms similar to those of human sperm in cervical mucus, which swim through utilising the drag anisotropy ratio of slender bodies. The effects of changing cell morphology and beat kinematics will be considered for different values of μ_0/μ_∞ , n and De .

3.2 Najafi-Golestanian swimmers

We will begin by considering the effects of shear-thinning on the Najafi-Golestanian swimmer (Najafi and Golestanian, 2004), discussed in section 1.2.1. The Najafi-Golestanian swimmer comprises two outer spheres which move relative to a central sphere with a non-reciprocal motion, as shown in figure 1.7b. We model this swimmer by three collinear symmetric Gaussian femlets. In our first variant of this swimmer, the sphere motion has been made smooth in time, which was an extension suggested in the original paper.

The outer spheres move as harmonic oscillators relative to the central sphere, and symmetry is broken by enforcing a phase difference, χ , between them. The body frame positions $x_i, i = 1, 2, 3$ of the sphere centroids are then given by

$$x_1(t) = -d + a \sin(2\pi t), \quad x_2(t) = 0, \quad x_3(t) = d + a \sin(2\pi t - \chi), \quad (3.1)$$

with the body frame velocity of each sphere given by $(u_b)_i = \dot{x}_i$. A characteristic length scale for the swimmer L is given by $L = 2d$, where d is a constant displacement, and a is the amplitude of the swimming sphere motion.

Due to the symmetry of the problem domain and beat pattern in the line $y = 0$, the swimmer will move solely in the x -direction. Thus, rather than moving the swimmer through the domain with an explicit time stepping procedure, we will calculate its instantaneous velocity $\mathbf{v} = (v, 0, 0)$ at different points over the beat cycle and use numerical integration to evaluate

the distance it travels over a single beat. This is referred to as the swimmer's progress.

We calculate the velocity at 25 points over the beat cycle $t = [0, 1)$ at the node locations for one dimensional Gaussian quadrature, and then integrate the velocity using Gaussian quadrature to obtain a value for the progress. The position of the central sphere in Stokes flow over a single beat cycle for $d = 0.5$, $a = 0.25$ and $\chi = \pi/2$ is shown in figure 3.1a. The fluid domain D is a channel of height $5L$ and length $10L$, where L is a characteristic length of the swimmer, with no-slip walls at $y = \pm 5L/2$ and open boundaries at $x = \pm 5L$. The radius of the spheres is $0.02L$.

If the viscosity ratio, μ_0/μ_∞ , is less than 1, then the effective viscosity (1.13) of a Carreau fluid increases with shear rate. For such a model, the relaxation time λ no longer has a physical interpretation in terms of polymer physics, but it may still be used as a regularised law to examine the effects of shear-thickening on microscopic swimmers (Montenegro-Johnson et al., 2012) Examples of shear-thickening fluids are custard and a mixture of cornstarch with water known colloquially as Oobleck. Thus, when considering the effects of changing the viscosity ratio on a given swimmer, we may consider a range of values of μ_0/μ_∞ covering both shear-thinning and thickening fluids.

3.2.1 Results, further analysis and discussion

The progress of the swimmer with kinematics prescribed by equation (3.1) over a single beat cycle in Carreau fluid is calculated as a function of three dimensionless quantities, the power law index n , the viscosity ratio μ_0/μ_∞ and the Deborah number De (figure 3.1b,c,d, respectively). These results show that shear-thinning aids the progression of the Najafi-Golestani swimmer, with figure 3.1c demonstrating that thickening hinders progress. When plotted on a semi-logarithmic axis (figure 3.2), a nearly perfect linear relationship is evident between progress and the logarithm of μ_0/μ_∞ for shear-thinning fluids, and the logarithm of μ_∞/μ_0 for shear-thinning fluids, respectively.

Figure 3.1d shows that for this model swimmer, optimum progress is achieved for $De \approx 0.5$, so that the angular frequency of the swimmer is approximately $1/2$ the characteristic relaxation time of the fluid. This is important since De is a function of the swimmer's beat frequency, which for an artificial swimmer, say, may be controlled and therefore optimised, whereas the power law index and viscosity ratio are fixed parameters for a given fluid. These results also draw an interesting parallel with the analysis of Teran et al. (2010) who used the immersed boundary method to show that the progression of a waving filament may be enhanced in a viscoelastic Oldroyd-B fluid at Deborah numbers close to 1.

To analyse the mechanism underlying this rheologically enhanced progression, we will begin by considering an even more simple model comprising two moving spheres modelled by collinear Gaussian femlets,

$$x_1(t) = -d + a \sin(2\pi[t - 1/4]), \quad x_2(t) = 0. \quad (3.2)$$

Since there is no mechanism to break time symmetry, this model is incapable of generating a net displacement in Newtonian viscous fluid. The centroid of the swimmer remains stationary, with the two arms exhibiting symmetric beat kinematics about the centroid in the lab frame. Since there is no apparent anisotropy in shear-thinning fluid to break this symmetry, this swimmer should exhibit identical lab frame kinematics for shear-thinning fluid.

For varying $n = [0.5, 0.6, \dots, 1]$, $De = [0, 0.1, \dots, 1]$ and $\mu_0/\mu_\infty = 1/2^{0,0.1,\dots,2}$, this swimmer exhibits zero net progress over its beat cycle, and thus shear-thinning has no impact. However, the average viscosity of fluid surrounding each sphere, taken over points at each femlet's effective radius, does decrease with shear-thinning, though for any fixed set of rheological parameters it is equal for each sphere. This suggests that shear-thinning acts on swimmers with prescribed kinematics through differences in the viscosity of fluid surrounding parts of the swimmer responsible for propulsion and parts responsible for drag. This is consistent

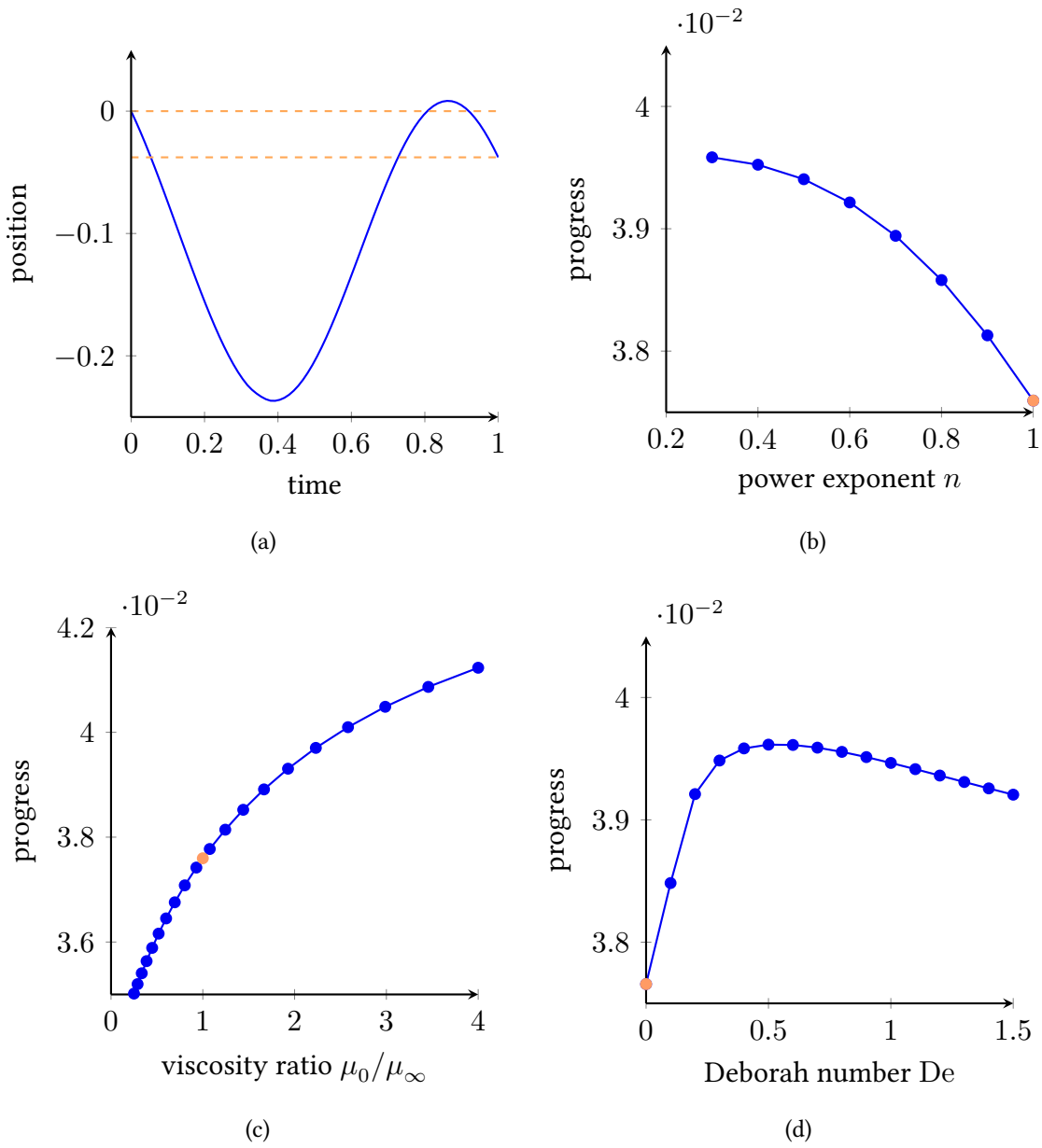


Figure 3.1: Simulation results for the smooth time Najafi-Golestani swimmer given by equation (3.1) (a) The global position of the central sphere moving through Newtonian fluid over the course of a single beat cycle, showing the progress as the distance between the two dashed lines. The swimmer's progress over a single beat cycle as a function of (b) the power law index n with $\mu_0/\mu_\infty = 2$ and $De = 1$, (c) the viscosity ratio μ_0/μ_∞ with $n = 0.5$ and $De = 1$ and (d) the Deborah number De with $n = 0.5$ and $\mu_0/\mu_\infty = 2$. In panels (b,c,d), the case corresponding to Stokes flow has been marked in orange

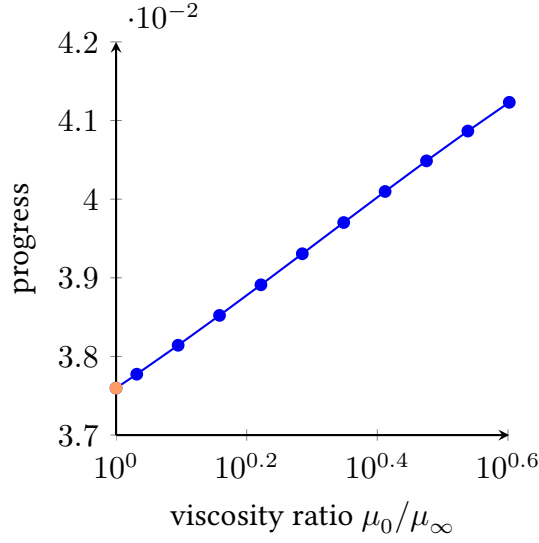


Figure 3.2: The shear-thinning results of figure 3.1c plotted on a logarithmic scale, showing a near perfect linear relationship.

with the approximate linear dependence of progress upon the logarithm of the viscosity ratio $\log(\mu_0/\mu_\infty) = \log(\mu_0) - \log(\mu_\infty)$, a difference between the zero and infinite shear log viscosities.

To examine this hypothesis, we add another stationary sphere to the the swimmer (3.2), giving

$$x_1(t) = -d + a \sin(2\pi[t - 1/4]), \quad x_2(t) = 0, \quad x_3(t) = d. \quad (3.3)$$

In the interval $t = [0, 0.5]$, the swimming arm moves in from $x_1(0) = -0.75$ to $x_1(0.5) = -0.25$, so that by force balance the swimmer will move to the left, having negative velocity at all times.

At each instant, we first calculate the average fluid viscosity around each sphere as evaluated at the femlet's effective radius. We then calculate the difference between the viscosity surrounding the moving sphere, responsible for propulsion, and the average of the viscosity surrounding the two stationary spheres. This viscosity differential has been plotted against the total progress of the swimmer relative to Stokes flow for varying $n, \mu_0/\mu_\infty$ and De in

figure 3.3a. This shows that the range of behaviours shown in figure 3.1 all collapse onto a single straight line, showing apparent proportionality between progress and this viscosity difference. This draws an interesting parallel with the drag force acting on a translating sphere in Newtonian fluid, which is proportional to the fluid viscosity.

For this portion of the beat cycle, leftward progress is in fact inhibited by shear-thinning. Progress is hindered because the fluid is relatively thicker around the spheres that are stationary, which are responsible for drag. This increases the drag on the swimmer. Additionally, the sphere responsible for propulsion has thinned fluid surrounding it, and therefore exerts less force on the fluid, decreasing propulsion.

This argument is consistent with the observation of an optimal Deborah number for the Najafi-Golestanian swimmer, since increasing De from 0 will initially increase the differential viscosity to an optimum, after which fluid will be thinned relatively more by the stationary spheres, thereby decreasing the difference, as shown in figure 3.4.

One could argue that the decreased swimming velocity over this portion of the beat cycle is responsible for the increase in the difference in the viscosity between the stationary spheres and the moving sphere, rather than the other way around. It is true that, for a given set of rheological parameters, decreasing the swimming velocity will decrease the velocity of the stationary spheres and increase the velocity of the moving sphere relative to the fluid, thereby increasing the viscosity difference. However, this effect is small compared to the effect of changing rheological parameters on the viscosity. Put another way, decreasing the swimming velocity leads to a change in shear rate of the fluid surrounding the spheres, leading to a change in viscosity, but this is small compared to the change in viscosity arising from changing the fluid rheological properties. Thus the change in viscosity affects the forces that the fluid exerts on the spheres, changing the swimming velocity rather than vice-versa.

Returning to the Najafi-Golestanian swimmer (3.1), we can now qualitatively understand the effects of shear-thinning at all moments in its beat cycle. This is summarised for the swim-

mer of the original paper (Najafi and Golestanian, 2004), for ease of exposition, in figure 3.5. Since at all moments in the beat cycle the fluid is thicker around the drag-inducing stationary spheres than the propulsive moving sphere, we expect swimming over each portion of the beat cycle to be inhibited by shear-thinning rheology. However, the results for the smooth time swimmer (3.1) show that total progress is in fact increased over the whole beat cycle.

This seems inconsistent with the result that progress over a full beat-cycle is enhanced by shear-thinning rheology, but since progress over the recovery portion of the stroke will be inhibited more by shear thinning than progress over the effective portion of the stroke, it is not. Thus, while at all moments the swimmer is inhibited by thinning, the net result is a gain in leftward progress.

We can test this qualitative prediction by considering the progress of this swimmer over each portion of its beat cycle. For simplicity, we will assume that the swimming spheres move at a constant speed. The positions of the three spheres $i = 1, 2, 3$ are given as a function of time t in table 3.1. Since we have shown that, at least for this swimmer, varying $n, \mu_0/\mu_\infty$ and De are all equivalent in terms of the underlying effect upon the swimmer, we consider only the swimmer's progress over each portion of the beat-cycle as a function of varying n . Figure 3.3 shows that swimming is indeed hindered over all portions of the beat cycle. However, as predicted, swimming is more greatly hindered during the recovery strokes, where the swimmer is moving in the opposite direction to that intended. Thus, the overall progress of the swimmer, shown in figure 3.3d is increased by shear-thinning, as in the smooth time version (3.1) we first considered.

3.2.2 Generalisation to N spheres

Since we wish to consider sperm-like swimmers, which swim by propagating a bending wave from the base to the tip of their flagellum, it is instructive to consider a generalised form of

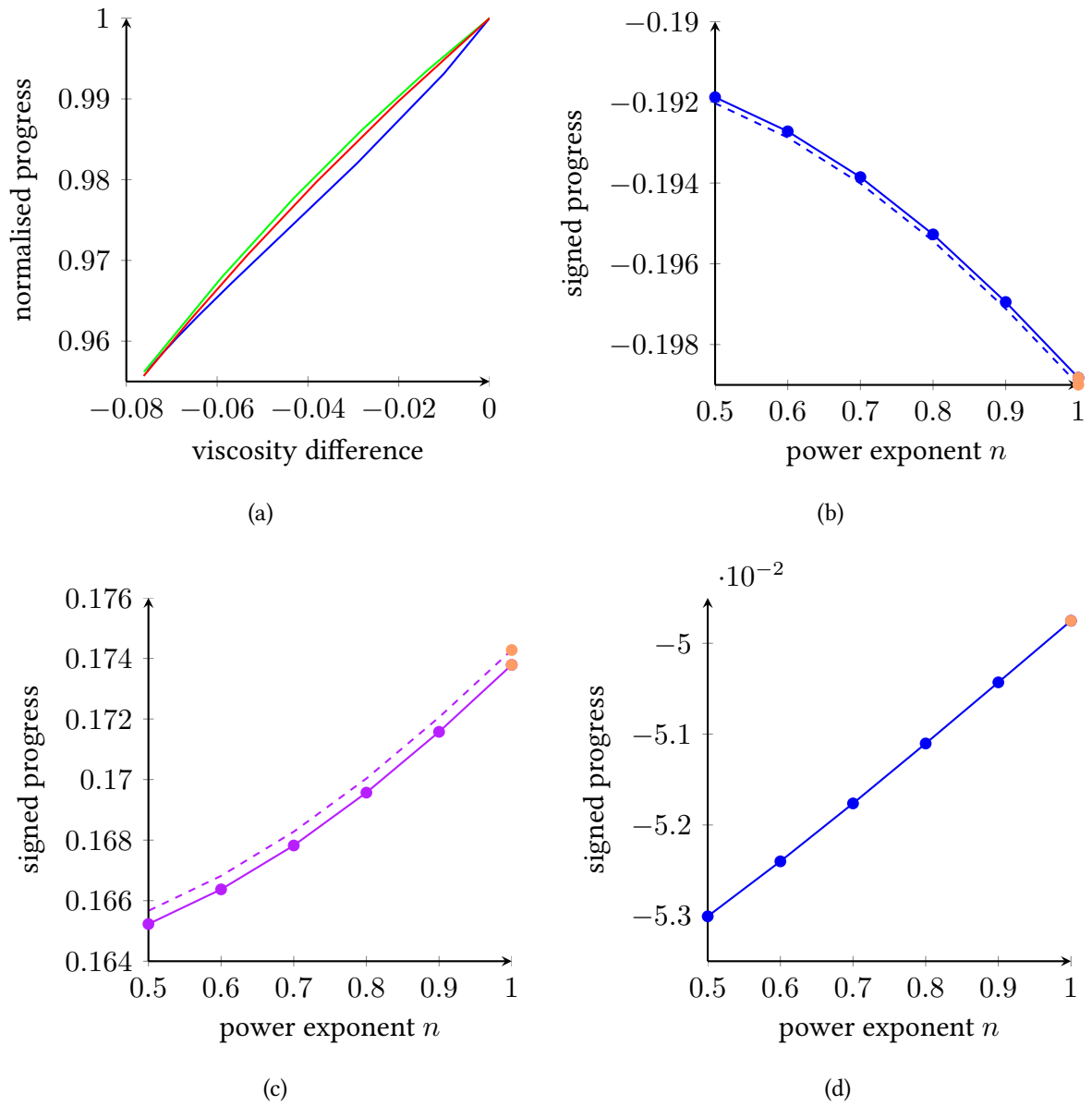
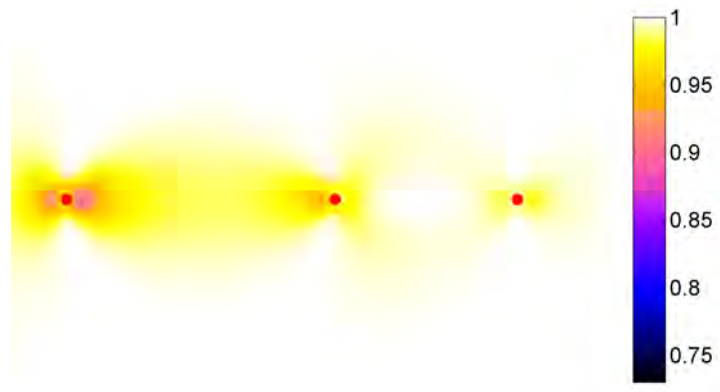
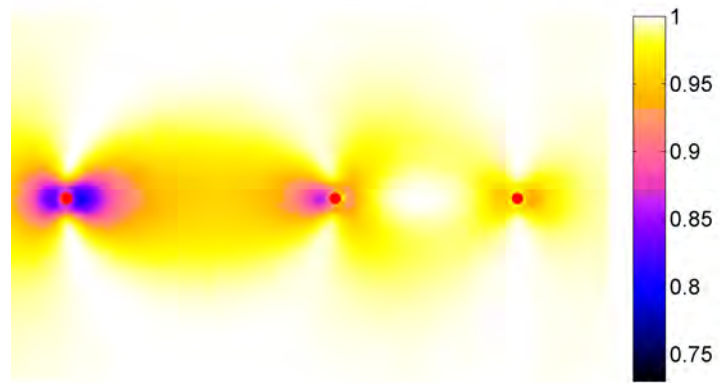


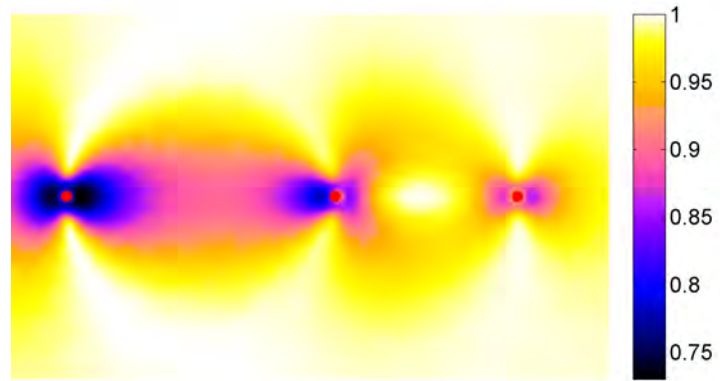
Figure 3.3: (a) The progress of the three-sphere swimmer defined by equation (3.3) as a function of the gradient along the swimmer in the direction of travel, obtained by varying the power law index (red), the viscosity ratio (green) and the Deborah number (blue) independently between the extremal values $n = [0.5, 1]$, $\mu_0/\mu_\infty = [1, 2]$ and $De = [0, 1]$. (b) The decrease in leftward progress during the effective strokes 1 (solid) and 2 (dashed) of the swimmer described in table 3.1 as a function of increasing power law index n and (c) the greater absolute decrease in rightward progress during the recovery strokes 3 (solid) and 4 (dashed). This leads to an overall increase in leftward progress with shear thinning rheology (d).



(a)



(b)



(c)

Figure 3.4: The viscosity field of fluid surrounding the three-sphere swimmer defined by equation (3.3), with $n = 0.5$, $\mu_0/\mu_\infty = 2$ and $De =$ (a) 0.4, (b) 0.8, and (c) 1.6, showing that although the minimum viscosity decreases with De , the viscosity difference across the swimmer is non-monotonic.

x_1	x_2	x_3	time t
$-(d+a) + 8at$	0	$d-a$	$[0, 1/4)$
$-(d-a)$	0	$d-a + 8a(t - 1/4)$	$[1/4, 1/2)$
$-(d-a) - 8a(t - 1/2)$	0	$d+a$	$[1/2, 3/4)$
$-(d+a)$	0	$d+a - 8a(t - 3/4)$	$[3/4, 1)$

Table 3.1: The positions of the three spheres of the original Najafi-Golestanian swimmers over each portion of its beat cycle.

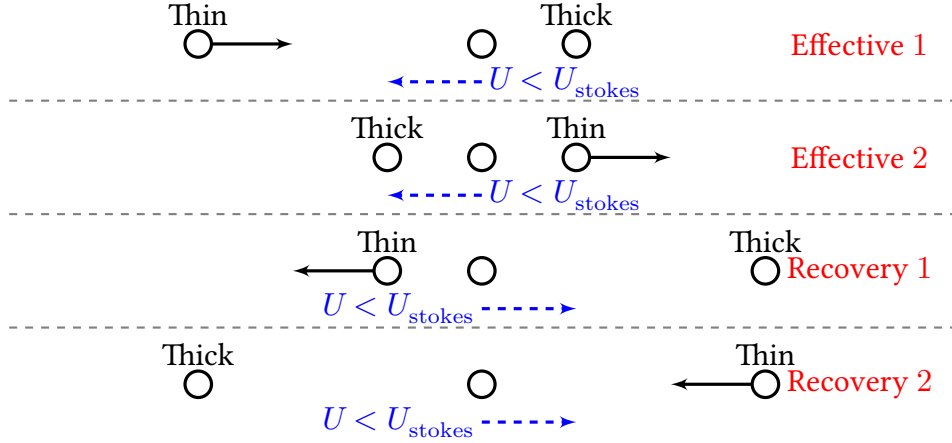
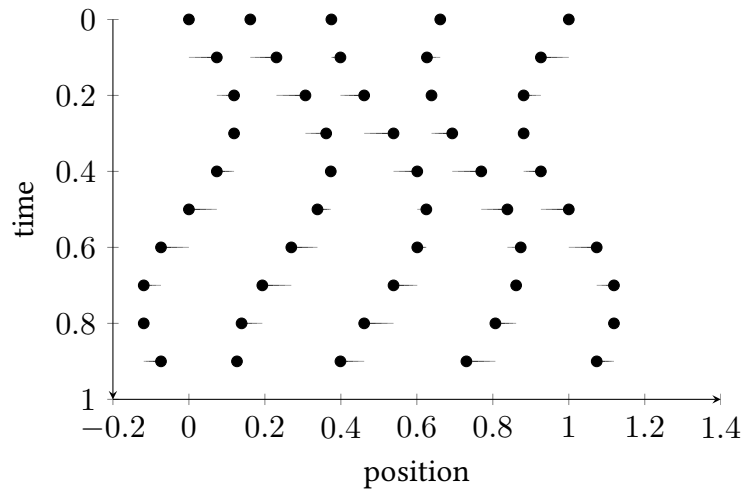


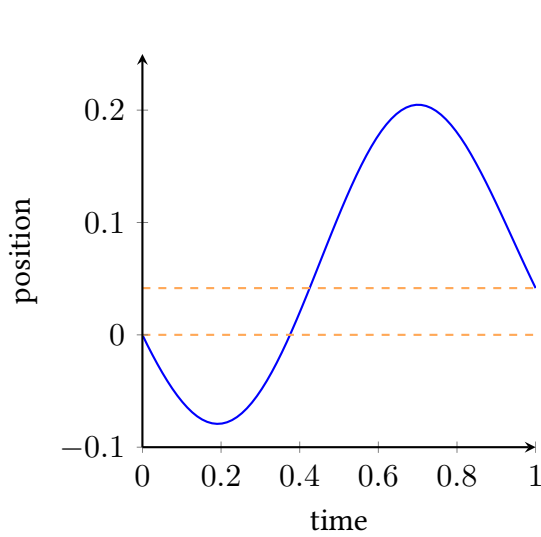
Figure 3.5: A schematic demonstration of the effects of shear-thinning rheology on the original Najafi-Golestanian swimmer over the effective and recovery parts of its stroke, showing the location of thick and thin fluid around it, and the direction of travel.

the Najafi-Golestanian swimmer with N spheres. A general swimmer in Stokes flow where each sphere underwent unspecified time-periodic motion was analysed recently by Vladimirov (2012). It was found that in the limit where spacing between spheres was large compared with their radius, the swimming velocity is found by a linear combination of velocities of all possible triplets of spheres. We will consider a particular form of N -sphere swimmer that propagates a compression wave from left to right

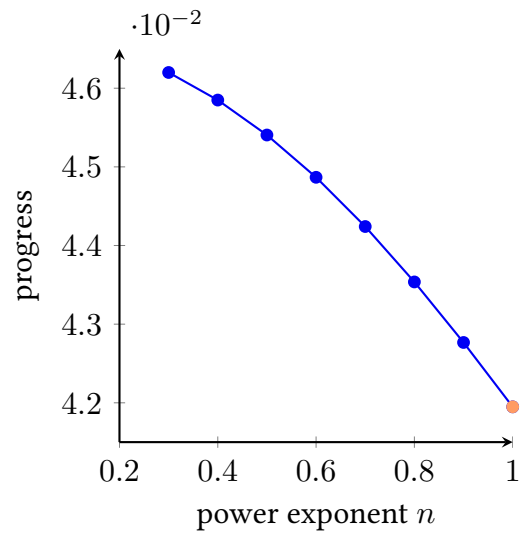
$$x_i(t) = \frac{i-1}{N-1} + \frac{1}{2(N-1)} \sin \left[2\pi \left(t - \frac{i-1}{2(N-1)} \right) \right], \quad i = 1, 2, \dots, N, \quad (3.4)$$



(a)



(b)



(c)

Figure 3.6: (a) The locus of the swimming spheres for the generalised Najafi-Golestani swimmer with $N = 5$ over the course of a beat cycle. The streaks show the distance and direction, in the body frame, of sphere travel over one tenth of a beat. (b) For $N = 5$, the global position of the N -sphere swimmer as it moves through Stokes flow over the course of a single beat cycle, showing the progress as the distance between the two dashed lines. (c) The five-sphere swimmer's progress over a single beat cycle as a function of the power law index n with $\mu_0/\mu_\infty = 2$ and $De = 1$, with the case corresponding to Stokes flow marked in orange.

For $N = 3$, this reduces to the smooth time Najafi-Golestanian (3.1) with $d = 1/2$, $a = \sqrt{2}/4$ and $\chi = -\pi/2$. The shift by π of the phase difference χ entails that this swimmer will travel in the opposite direction (right) to the swimmers considered previously. The locus of the swimming spheres over a single beat is shown for the case $N = 5$ in figure 3.6a.

This swimmer will travel in the same direction as the compressional wave that it propagates. This is in contradistinction to sperm-like swimmers, which swim in the opposite direction to the waves that travel along their flagella. This is because the underlying fluid mechanics that they exploit to generate net displacement is different: sperm utilise the two-to-one drag anisotropy ratio in order to swim (Gray and Hancock, 1955), whereas the class of generalised Najafi-Golestanian swimmers utilise the fact that the drag on spheres moving along the same line is lower if the spheres are in one another's slip stream than if they are far apart.

The position of the swimmer (3.4) is shown as a function of time for $N = 5$ in Stokes flow in figure 3.6b. Figure 3.6c shows that this swimmer is affected by shear-thinning in a similar manner to the three-sphere swimmer. There is a difference, however, in the amount by which progress is increased. For the five-sphere swimmer, the increase in progress arising from shear-thinning, relative to the Stokes case, is approximately twice that occurring for the three-sphere swimmer.

Before examining more biologically realistic models of viscous swimmers, we can gain an additional insight from the N -sphere model. To examine the effect of shear-thinning rheology on the three-sphere model, we considered the difference in viscosity surrounding the propulsive and drag inducing spheres respectively. As N increases towards a continuous swimmer, more akin to a flagellum, this discrete difference approaches a gradient. As such, for sperm flagella and other continuous swimmers, it may be that the effects of shear-thinning are best understood by considering gradients of the effective viscosity between propulsive and drag inducing portions of the swimmer.

3.3 Two dimensional squirmers

Before examining the propulsion of sperm-like swimmers, we will consider the effects of shear-thinning rheology on another conceptual model of a viscous swimmer inspired by ciliates. Cilia utilised for locomotion typically beat with an asymmetric waveform, known as the effective-recovery stroke pattern (Blake and Sleight, 1974). A ciliated swimmer will in general express a large number of cilia which beat with a phase difference between neighbours in a coordinated manner (Childress, 1981). Examples are the protozoa *Opalina* and *Paramecium* (Brennen and Winet, 1977) and the alga *Volvox Carteri*. This type of swimming motivates ‘envelope’ modelling approaches (Lighthill, 1952; Blake, 1971b) whereby the array of cilia are incorporated through either a slip velocity condition on the cell surface, or by small ‘squirming’ deformations of the cell body (Ishikawa et al., 2006; Lin et al., 2011).

We first analyse a model swimmer with a time independent stroke, where the effects of coordinated ciliary beating have been time averaged over a beat as a constant slip velocity. For a spherical squirmer swimming with a tangential slip velocity u_θ given in polar coordinates, the slip velocity is typically decomposed into ‘swimming modes’ of spherical harmonics (Michelin and Lauga, 2011)

$$u_\theta(\cos \theta) = \sum_{n=1}^{\infty} \alpha_n K_n(\cos \theta), \quad (3.5)$$

for

$$K_n(\cos \theta) = \frac{(2n+1)\sin \theta}{n(n+1)} L'_n(\cos \theta), \quad (3.6)$$

with $L_n(\cos \theta)$ the n -th Legendre polynomial. Thus, slip velocity squirmers are characterised by the coefficients α_n of the modes of their swimming.

We will begin by considering the simplest two dimensional squirmer (Crowdy, 2011; Davis and Crowdy, 2012) with purely the first mode, i.e. $\alpha_n = 0 \forall n \geq 2$. This ‘treadmilling’ squirmer has a radius $r = L/2$ and generates a time independent tangential slip velocity in the body

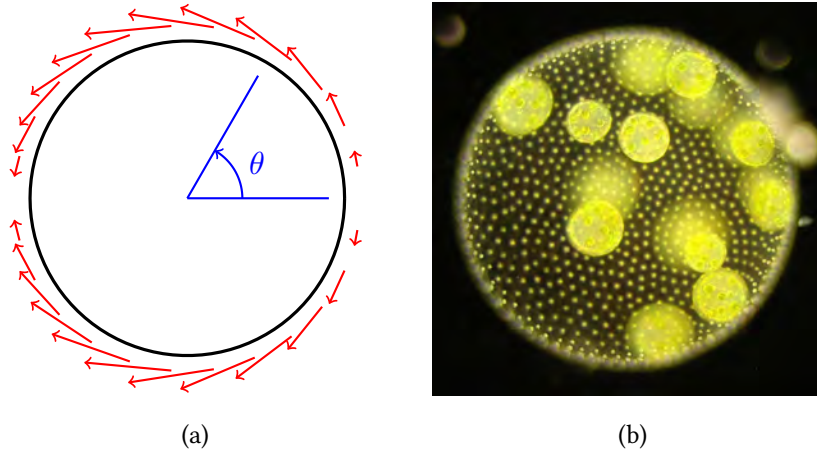


Figure 3.7: (a) A schematic of the two dimensional treadmilling squirmer, along with (b) a micrograph of a *Volvox Carteri* colony, showing surface cilia that beat in a coordinated fashion to propel the colony forwards. This cell also shows a number of characteristic ‘daughter’ colonies within it. Image taken by Prof. Ray Goldstein and reprinted with his permission.

frame of

$$u_{\theta} = (1/2) \sin \theta. \quad (3.7)$$

This swimmer is shown, along with an image of *Volvox Carteri*, in figure 3.7. By symmetry, the squirmer swims purely in the positive x direction.

3.3.1 Results and discussion

Shear-thinning decreases the velocity of this squirmer (figure 3.8). Figure 3.8c shows a striking apparently linear dependence of the swimming velocity upon the power-law index n . The decrease in velocity is small; for $\mu_0/\mu_{\infty} = 2$, $n = 0.5$ and $Sh = 1$, the velocity is reduced by a little over 3%.

The effective viscosity field of the flow has a simple form; even relatively near to the swimmer, contours of equi-viscosity are approximately circular, centered on the swimmer (figure 3.9). However, very near to the surface, the fluid surrounding the propulsive elements of the treadmilling squirmer is relatively thicker than that surrounding the drag-inducing portions.

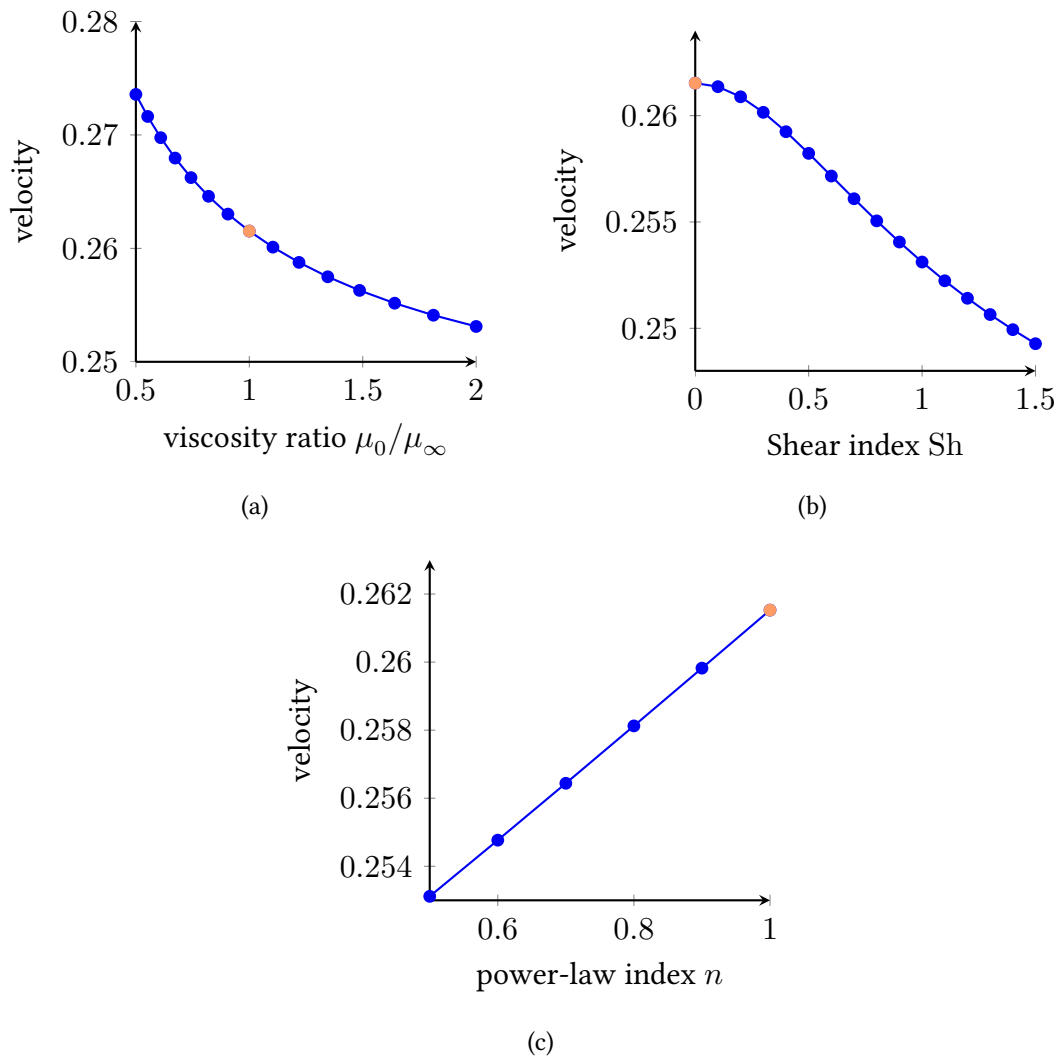


Figure 3.8: The velocity of the treadmilling squirmer with slip velocity given by equation (3.7) as a function of (a) the viscosity ratio μ_0/μ_∞ with $n = 0.5$ and $Sh = 1$, (b) the shear index Sh with $n = 0.5$ and $\mu_0/\mu_\infty = 2$ and (c) the power-law index n with $\mu_0/\mu_\infty = 2$ and $Sh = 1$. In each panel, the case corresponding to Newtonian fluid is marked in orange.

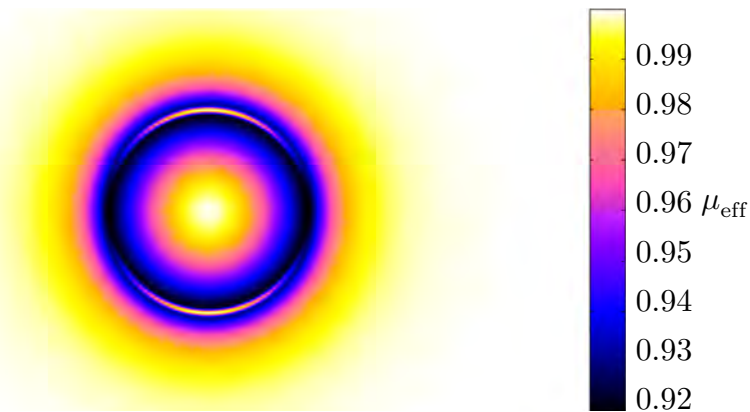


Figure 3.9: The effective viscosity of Carreau fluid, normalised to $\mu_0 = 1$, surrounding the treadmilling squirmer for $\mu_0/\mu_\infty = 2$, $n = 0.5$ and $Sh = 0.5$. These parameter values are the extremal values used for the data in figures 3.10 and 3.11. Away from the swimmer surface, contours of equi-viscosity are approximately circular. On the surface, fluid is relatively thicker surrounding the propulsive portions of the swimmer.

Thus, the viscosity differential for this squirmer is positive, yet its velocity is decreased by shear-thinning, demonstrating that slip velocity models differ from no-slip multiple sphere swimmers in this respect. The reduction in velocity arises from the envelope of thinned fluid surrounding the squirmer.

Figure 3.10 shows the radial variation in the effective viscosity of the fluid surrounding the squirmer. As n decreases, the viscosity immediately surrounding the swimmer decreases, but the rate at which the viscosity approaches the zero-shear value increases. As a result of this increase, the size of the envelope of thinned fluid surrounding the swimmer varies little with changes in rheological parameters (figure 3.10a). For any fixed value of the radial coordinate r , with $r = 0.5$ being the squirmer's surface, the effective viscosity at that point decreases approximately linearly with n .

Since the decrease in swimming velocity also exhibits a linear dependence upon the power-law index n , we examine the dependence of swimming velocity on the effective viscosity of the fluid surrounding the squirmer. Figure 3.11a shows the decrease in swimming velocity relative to the Newtonian case as a function of the effective viscosity of the fluid envelope

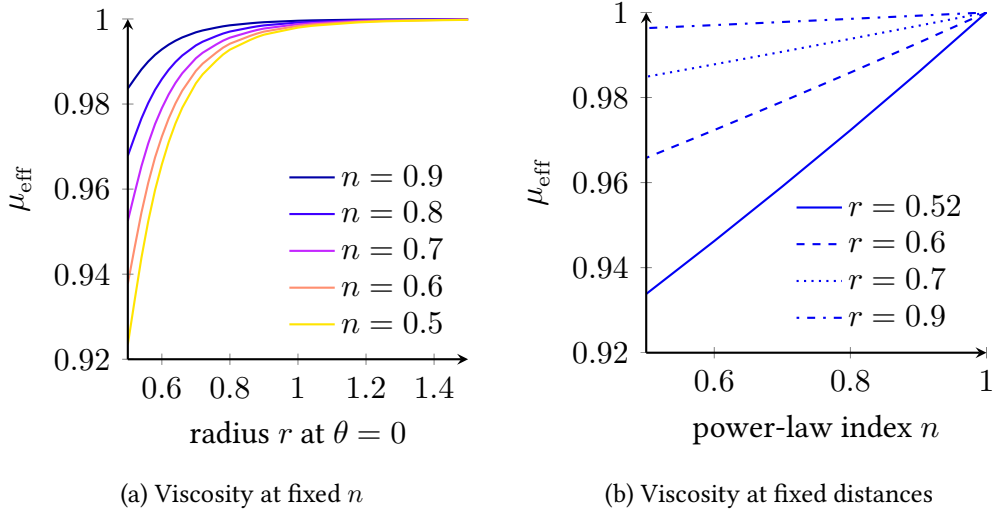


Figure 3.10: The effective viscosity of the fluid envelope surrounding the treadmilling squirmer. (a) Changes in the viscosity field as a function of the radial coordinate r for different values of the power-law index n . The swimmer surface is given by $r = 0.5$. (b) For fixed values of r , the effective viscosity exhibits a near linear dependence upon the power-law index n .

at $r = 0.52$, a small distance from the squirmer's surface, for varying viscosity ratio, shear index and power-law index. This figure demonstrates a strong linear correlation between the effective viscosity of the fluid a small distance from the swimmer's surface and the swimmer's velocity.

However, whilst the absolute values of viscosity do not affect swimmers with prescribed kinematics, the envelope of thinned fluid shields the far field flow from the flow generated by the squirmer. As fluid becomes relatively thinner around the squirmer, the decay rate of the near-field flow increases. This draws an interesting parallel with the work of Zhu et al. (2012), who found a similar effect for viscoelastic (Giesekus) fluids. In the near-field, along the line $\theta = 0$, the velocity of the flow is approximately

$$u \approx \frac{A}{r^\alpha}, \quad \therefore \log u \approx \log A - \alpha \log r. \quad (3.8)$$

Thus, the flow decay rate is given by

$$\alpha = -\frac{\Delta \log u}{\Delta \log r}. \quad (3.9)$$

Close to the squirmer's surface, the Newtonian flow decay rate $\alpha_{\text{newt}} = 1.95$.

Figure 3.11b shows the swimming velocity of the squirmer as a function of this decay rate at $r = 0.52, \theta = 0$, a small distance from the squirmer's surface, relative to the Newtonian case for varying rheological parameters $\mu_0/\mu_\infty, n$ and Sh . The decrease in velocity and increase in flow decay exhibit a linear relationship, and are the same magnitude; the slope of the curve is close to -1 . This observation motivates the following argument: The squirmer generates an envelope of thinned fluid around itself when swimming through Carreau fluid. This envelope increases the decay rate of flow away from the squirmer's surface. Thus, prescribed motion on the surface moves relatively less fluid, which decreases the swimming velocity.

Although the potential number of slip velocity swimming modes to consider is infinite, this reasoning suggests that all time averaged slip velocity squirmers will be inhibited by shear-thinning rheology. This is certainly the case for swimmers with second mode behaviour incorporated, which are affected by shear dependent rheology in much the same manner.

Thus, if we seek a squirmer that may effectively exploit shear-thinning rheology, we need to examine a broader range of squirming models. We may wish to consider the impact of radial velocity modes (Ishikawa et al., 2006), however the above reasoning suggests that these swimmers would also be hindered by shear-thinning. Since a ubiquitous feature of viscous propulsion is the propagation of travelling waves, and motivated by the fact that the Najafi-Golestanian swimmer is only aided by shear-thinning because of effective-recovery stroke asymmetry, we will now examine time dependent slip velocities which incorporate the effective-recovery stroke of the ciliated surface and the propagating metachronal wave.

The effect of cilium beating is again incorporated through a purely tangential surface slip

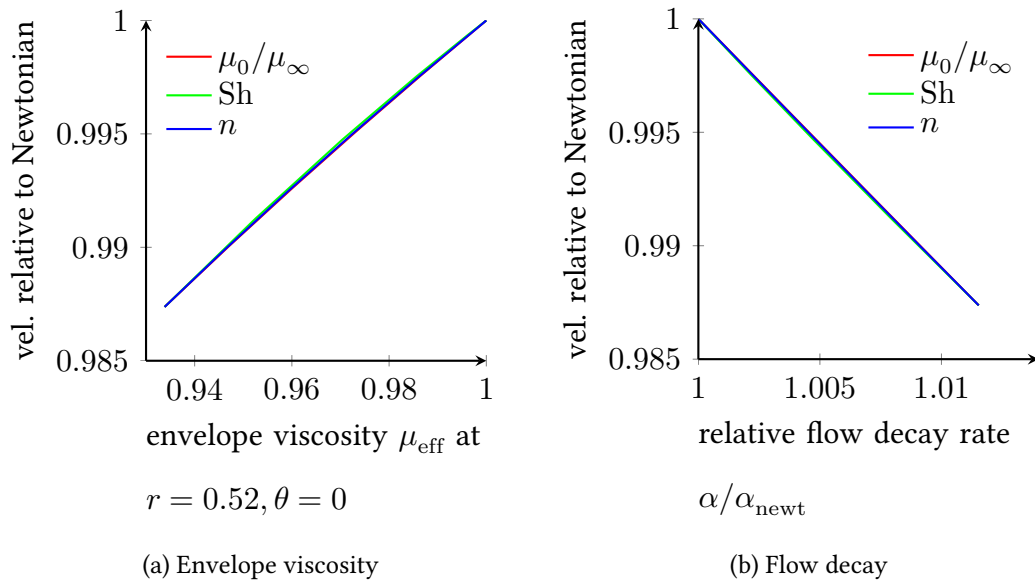


Figure 3.11: The velocity relative to the Newtonian case of the treadmilling squirmer as a function of (a) the effective viscosity on the contour $r = 0.52$ and (b) the rate of decay α of the velocity from the surface of the squirmer relative to the Newtonian case α_{newt} . The velocity has been calculated while varying the three rheological parameters of Carreau flow for $n = 0.5, \mu_0/\mu_\infty \in [1, 2], \text{Sh} = 0.5$ (red), $n = 0.5, \mu_0/\mu_\infty = 2, \text{Sh} \in [0, 0.5]$ (green) and $n \in [0.5, 1], \mu_0/\mu_\infty = 2, \text{Sh} = 0.5$ (blue). This figure demonstrates a striking proportionality between the velocity and the decay rate of the fluid.

velocity u_θ , which is now a function of time. The metachronal wave is modelled as a travelling wave of cilium activity moving from $\theta = 0$ to $\theta = \pm\pi$, so that $u_\theta = A(\theta) \sin(k\theta - 2\pi t)$. To incorporate the effective-recovery stroke asymmetry, we will decrease the slip velocity of recovering cilia. This is achieved by taking the wave function $\sin(k\theta - 2\pi t)$ and decreasing the magnitude of the negative portions of the function relative to the positive, i.e. by adding $B(\theta) = \hat{B} \sin^2(k\theta - 2\pi t)$, $0 \leq \hat{B} < 1$. Finally, to avoid velocity discontinuities at $\theta = 0, \pi$, the envelope function $A(\theta)$ is given the property $A(0) = A(\pi) = 0$. After the treadmilling squirmer, we choose $A(\theta) = \hat{A} \sin(\theta)$. This gives a swimmer with tangential velocity

$$u_\theta(t) = \hat{A} \sin \theta \left\{ \sin(2\pi[k\theta - t]) + \hat{B} \sin^2(2\pi[k\theta - t]) \right\}. \quad (3.10)$$

Whilst this approach may seem ad-hoc, the resultant form of the tangential velocity captures the travelling wave of cilium activation and recovery, an essential feature of ciliated swimmers. Furthermore, upon taking the time average over a single beat of the slip velocity (3.10) we recover

$$\begin{aligned} \langle u_\theta(t) \rangle &= \int_0^1 u_\theta(t) dt = \hat{A} \sin \theta \int_0^1 \left[\sin(k\theta - 2\pi t) + \hat{B} \sin^2(k\theta - 2\pi t) \right] dt \\ &= \frac{\hat{A}\hat{B}}{2} \sin \theta, \end{aligned} \quad (3.11)$$

the tangential velocity of the treadmilling squirmer.

Figure 3.12a shows the position of this swimmer for $\hat{A} = 1$, $\hat{B} = 1/2$ and $k = 1/2$ over a single beat cycle. The swimmer's progress over a single beat cycle is given as a function of the power law index n in figure 3.12b, showing that this swimmer, too, is hindered by shear-thinning rheology. This is because shear rates are higher at the portions of the swimmer's surface responsible for rightward propulsion, the portions modelling the cilia effective strokes, than at the recovery sections, making a differential of thick to thin fluid on the drag

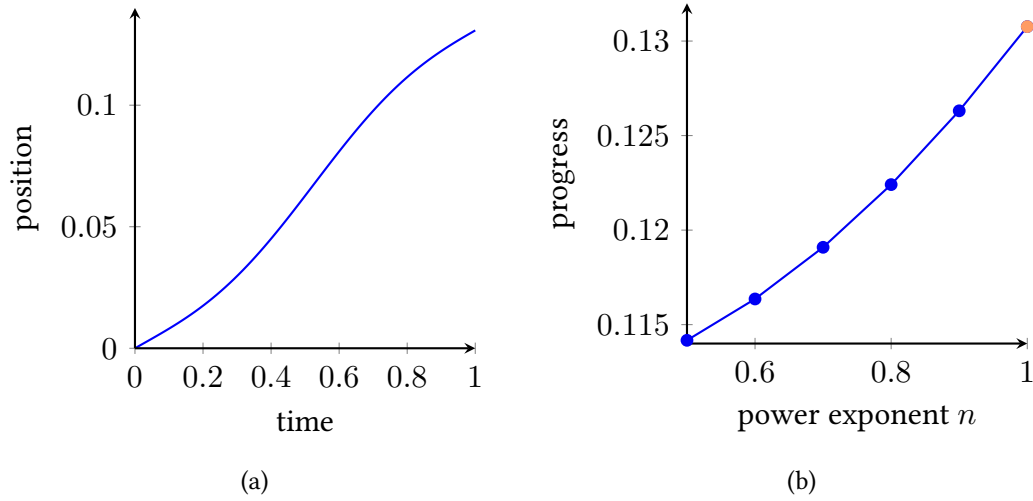


Figure 3.12: (a) The global position of the squirmer with slip velocity (3.10) over the course of a single beat with $\hat{A} = 1$ and $\hat{B} = 0.5$, and (b) the swimmer's progress over a single beat cycle as a function of the power law index n with $\mu_0/\mu_\infty = 2$ and $De = 1$. In panel (b), the case corresponding to Stokes flow has been marked in orange.

to propulsive portions of the swimmer, hindering progress.

While this does not preclude the possibility of finding a model squirmer that is aided by shear-thinning, it seems unlikely that this squirmer will be modelled by a rigid body with some prescribed surface velocity. In fact, the above reasoning would suggest that for any isolated rigid body G with a surface velocity distribution \mathbf{u}_s , shear-thinning will hinder swimming in whatever direction G should move. This draws an interesting parallel with the work of Zhu et al. (2012), who found that spherical squirmers were also hindered by a different non-Newtonian fluid property, viscoelasticity.

However, modelling squirmers with a surface velocity distribution may neglect effects arising from interactions below the scale of this averaging. We have not considered squirmers where the surface is perturbed following the metachronal wave, which for the majority of ciliated swimmers is a more accurate model. Furthermore, we still have yet to consider the effects of non-Newtonian on a beating filament which may, in the case of viscoelasticity (Teran et al., 2010) improve propulsion. A study of the effects of shear thinning rheology on beating

filaments exhibiting prescribed kinematics forms the final part of this chapter.

3.4 A two dimensional sperm-like swimmer

We will conclude this study by examining the effects of shear-thinning rheology on the swimming of a two dimensional model sperm with prescribed waveform. Swimming trajectories will be analysed using variables from Computer Aided Semen Analysis (CASA), see for example Mortimer (1997). However, while CASA variables are statistical averages over many beat-cycles determined from video microscopy of living cells sampled at 60 Hz, we will generate a smooth, time periodic waveform and thus our parameters will be measured over a single beat. The variables we will consider are demonstrated for an example trajectory over one beat-cycle in figure 3.13. Recall that the cell ‘progress’ is the distance between its start and end points, its straight line velocity VSL is then given by $\text{progress}/T$. Its curvilinear, or instantaneous, velocity VCL is the velocity of the centroid of the cell head at any given point in time, and ALH is the amplitude of the cell’s lateral head displacement, which we define as the difference between the maximum and minimum y values on the trajectory. We may also wish to consider the path length PL of the trajectory, that is the total distance travelled, as well as the path straightness $\text{STR} = \text{progress}/\text{PL}$.

It has been shown (Katz et al., 1978; Smith et al., 2009c) that the flagellar waveform of human sperm is modulated by the viscosity of the medium in which it swims. Low viscosity swimming is characterised by long wavelength, low amplitude beating. The head exhibits a high degree of pitch and yaw, thrashing and often rolling through the fluid. High viscosity swimming is typified by planar beating that grows in peak curvature and shear angle towards the distal portion of the tail. The yaw amplitude is greatly reduced, and the cell may either remain entirely in the plane or roll much more slowly than in the case of low viscosity beating. In the following modelling, we will prescribe a function for the flagellar configuration which

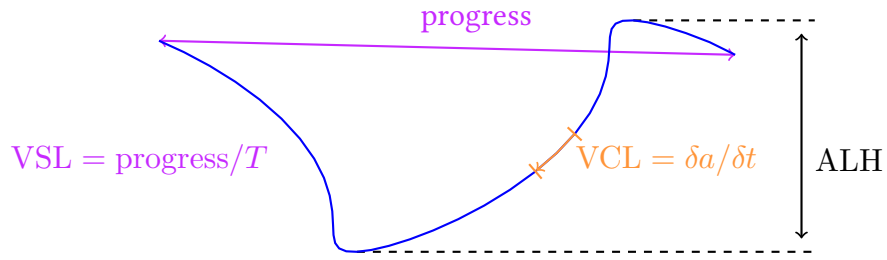


Figure 3.13: A schematic demonstrating how our swimming parameters are calculated for the trajectory (blue) of a swimmer moving from right to left over one beat-cycle of period T . The progress is the distance between start and end points, VSL is progress divided by the beat period T , ALH is the total side-to-side motion and the instantaneous velocity VCL is the derivative of the arclength along the trajectory s with respect to time.

captures the features of this high viscosity waveform.

The ultrastructure of mammalian spermatozoa, the passive stiffening structures surrounding the axoneme such as the outer dense fibres in human sperm, are hypothesised (Lindemann, 1996) to have evolved in order to generate waveforms of this kind that are able to propel the cell through high viscosity fluid at the roughly the same speed as the swim through water. This is evidenced by the fact that sea urchin sperm, which do not have these passive stiffening elements, are unable to produce this high viscosity waveform (Brokaw, 1966; Woolley and Vernon, 2001), as shown at the beginning of this thesis in figure 1.1, and exhibit greatly reduced motility.

We will now examine the swimming of a two dimensional monoflagellate pusher through Carreau fluid as an analogue of human sperm exhibiting planar beating in mucus. The swimmer is propelled by a single flagellum that propagates a bending wave along its length, generating the forces required to move the cell forward. As in section 1.3.2, we parameterise the flagellum in terms of its shear angle $\psi(s, t)$, the angle of the tangent of the flagellum given in

the body frame. A shear angle of the form

$$\psi(s, t) = Cs \cos[2\pi(ks - \omega t)], \quad (3.12)$$

represents a bending wave propagating down the flagellum, steepening towards the less stiff distal end with a linear envelope. This produces a waveform representative of sperm swimming in high viscosity fluids (Smith et al., 2009c), shown in figure 3.14. The lab frame position of the flagellum is then given by rotating the centreline (2.39) by the swimmer's orientation, and translating by the current head position. The head is modelled by an ellipse, with semi-axes $a_x = 0.05L$ and $a_y = 0.04L$ where L is the length of the flagellum. This is maintained at a constant angle to the neck of the flagellum, as shown in figure 3.14a. Note that since this model is two dimensional, the flagellum is in fact equivalent to a waving sheet, and thus fluid is unable to pass over it as it would in three dimensions. As such, the pressure at the end of the flagellum will be relatively higher, and so too the force at the distal portion of the flagellum. However it is still instructive to examine models in two dimensions to gain understanding of physical effects that may be present in three dimensions, and furthermore the velocities we will calculate equate to approximately 1 body length per second, which is comparable to that observed experimentally for sperm in viscous media (Smith et al., 2009c).

Length scales are normalised to the flagellum length, so that one length unit corresponds to $55 \mu\text{m}$, and one time unit corresponds to a single beat of the flagellum. Thus, for a tail beating at 10 Hz one time unit corresponds to 0.1 s. We will begin by modelling a sperm obeying equation (3.12) for maximum shear angle $A = 0.45\pi$ and wavenumber $k = 2.5$.

3.4.1 Results and discussion

Figure 3.16a shows trajectories of the swimmer over a single beat-cycle for different values of μ_0/μ_∞ . As μ_0/μ_∞ increases, the trajectories become flatter and the cell travels a greater

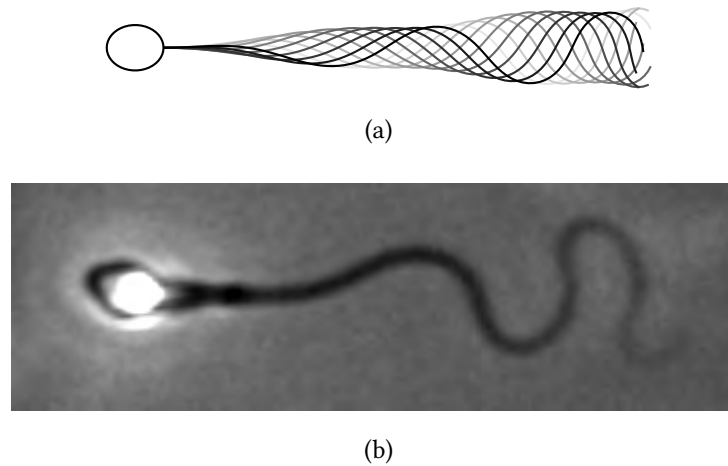


Figure 3.14: (a) The flagellar waveform generated by shear angle (3.12) and (b) a micrograph of a human sperm in methylcellulose, a fluid with comparable viscosity to that of cervical mucus.

distance, as shown in figure 3.17a. For a viscosity ratio of $\mu_0/\mu_\infty = 4$, the cell progresses 38% further in a single beat than it would in Newtonian fluid.

This increase in cell progress can be attributed to two factors. Firstly, the decrease in ALH entails an increase in forward relative to side-to-side motion, quantified in figure 3.17b, thereby increasing the cell progress. This effect arises because the cell thins the fluid substantially less around its head than its flagellum, as shown in figure 3.15. This leads to a relative increase in the drag on the head relative to the rest of the cell, which has the effect of reducing side-to-side motion. For Najafi-Golestani type swimmers, thicker fluid around the drag inducing portions of the swimmer led to decreases in cell speed, but here this is more than balanced out by decreases in ALH. This is consistent with the findings of Smith et al. (2009b), who used the Boundary element method in three dimensions for Newtonian fluid to show that models of human sperm cells with biologically realistic head morphology exhibit less yaw than those with spherical head, due to increased drag.

However, figure 3.17c shows that the increase in cell progress is not wholly accounted for by the reduction in ALH, since the average curvilinear velocity \overline{VCL} of the cell over a beat also increases with μ_0/μ_∞ . For $\mu_0/\mu_\infty = 4$, the increase in \overline{VCL} accounts for approximately 38%

of the total increase in the cell's progress. This is despite the relatively thicker fluid around the drag inducing head which, as we have already seen, would tend to decrease \overline{VCL} .

There are a number of possible explanations for this. Firstly, we might expect that shear-thinning rheology could enhance the drag anisotropy ratio for slender bodies. Since this is the fundamental mechanism by which monoflagellate pushers swim, an increase in drag anisotropy would lead to an increase in propulsion. However, numerical investigation of a slender rod in an enclosed cavity revealed that the drag anisotropy ratio for slender bodies in shear-thinning fluid decreased very slightly as a function of μ_0/μ_∞ . Since monoflagellate pushers exploit drag anisotropy to generate propulsion, we would expect that this would in fact decrease \overline{VCL} slightly. Thus we may exclude rheologically enhanced drag anisotropy as a possible cause for the observed increase and there must be an increase in the propulsion produced by the flagellum. From our understanding of the effects of shear-thinning on Najafi-Golestani swimmers and squirmers, we hypothesise that the increase in propulsion arises from complex interactions between the propulsive and drag inducing portions of the flagellum with the gradient of thick to thin fluid along that the waveform induces.

As with the Najafi-Golestani swimmer, such a mechanism is consistent with the existence of an optimal Deborah number for \overline{VCL} shown in figure 3.17e, since the gradient of fluid viscosity along the flagellum depends non-monotonically on De . For low De , the fluid is only thinned a small amount at the very distal region of the flagellum. As De increases to its optimal value, less shear is required to thin the surrounding fluid, thus increasing the differential viscosity between the proximal and distal regions to a maximum. For values of De greater than the optimum, even a small amount of shear thins the fluid, so that the fluid surrounding the proximal portion of the flagellum is thinned substantially, thereby decreasing the differential viscosity, as shown in figure 3.15.

The force that the flagellum exerts upon Newtonian (blue) and shear-thinning (orange) fluid is shown in figure 3.16b. This shows that there is no appreciable change in the direc-

tion of the force profile along the flagellum for shear-thinning rheology, which is consistent with the observation that rheological changes in drag anisotropy are not responsible for increased propulsion. However, figure 3.16d shows that the relative strength of the force that the proximal relative to the distal portion of the flagellum exerts on the fluid is increased with shear-thinning rheology. This is because the fluid is thinner around the proximal portion of the flagellum. A time series of the magnitude of the flagellar force profile is shown in figure 3.16d, which shows peaks in the magnitude propagating from proximal to distal ends of the flagellum through time. Upon examining figure 3.16c, it is clear that these peaks correspond to propulsive portions of the flagellum, whereas the troughs correspond to drag inducing portions.

With this in mind, re-examination of figure 3.16d shows that the drag in the proximal portion of the flagellum is not increased appreciably in Carreau fluid relative to the Stokes case, whereas drag in the distal end is decreased significantly. Thus, the relative increase in propulsion in the distal relative to the proximal portion of the flagellum and the decrease in drag in the distal portion are responsible for the observed increase in \overline{VCL} .

Figures 3.17d and 3.17f show the ratio of the magnitude of force generated in the proximal and distal portions of the flagellum as a function of viscosity ratio and Deborah number respectively, for the flagellum at time $t = 0$. The force ratio is estimated in these results as the average of peaks 2 and 3 in the force magnitude, shown in figure 3.16d, divided by the average of peaks 4 and 5. The functional similarity between the force ratio and the average curvilinear velocity, shown in figure 3.17, gives support to the hypothesis that redistribution of propulsive and drag forces along the flagellum induced by the observed gradient of thick to thin fluid are responsible for increases in instantaneous velocity.

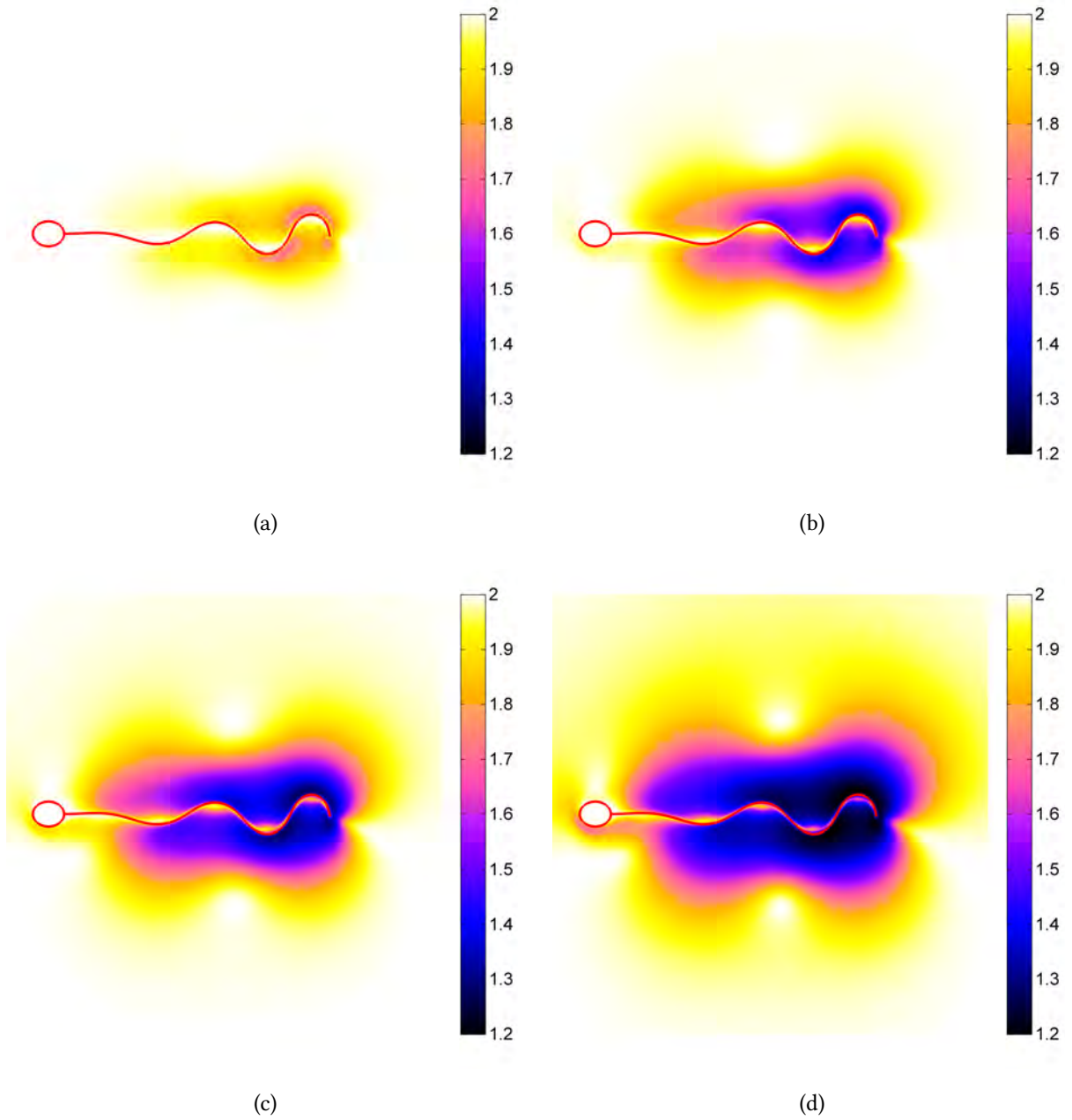
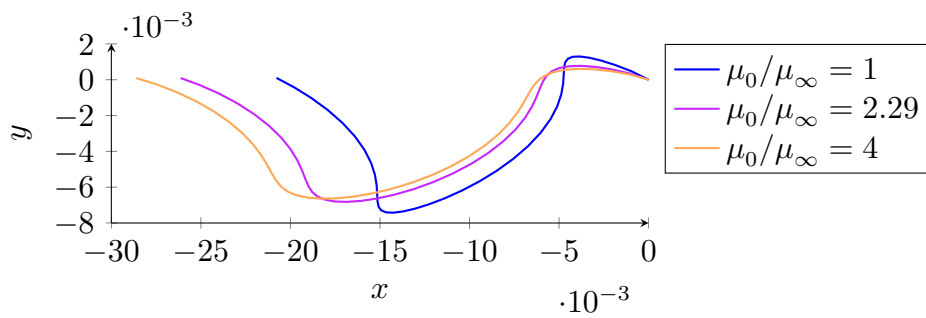
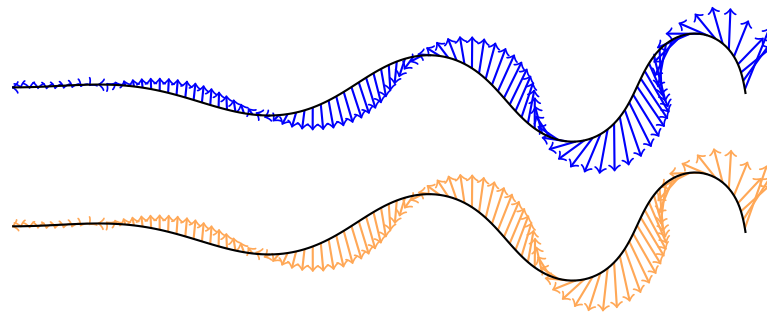


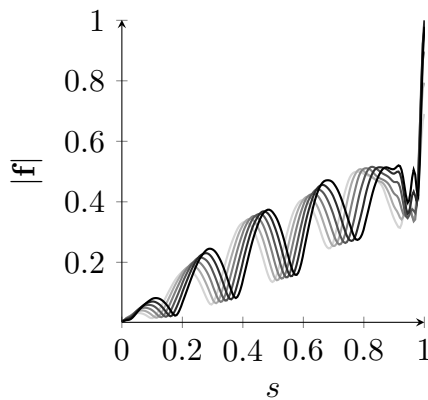
Figure 3.15: The impact of varying $De = \lambda\omega$ on the effective viscosity μ_{eff} of Carreau fluid surrounding a two dimensional sperm-like swimmer at (a) $De = 0.2$, (b) $De = 0.8$, (c) $De = 1.5$ and (d) $De = 3$ with $\mu_0/\mu_\infty = 2$ and $n = 0.5$. Here, $k = 2.5$ and $A = 0.45\pi$.



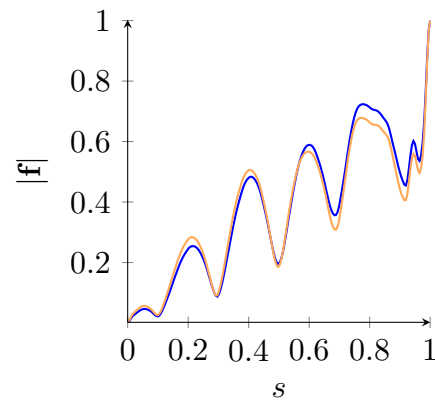
(a)



(b)



(c)



(d)

Figure 3.16: (a) Trajectories of a two dimensional sperm-like swimmer in Carreau flow for different values of the viscosity ratio μ_0/μ_∞ , showing an increase in progress and a decrease in ALH as μ_0/μ_∞ increases. (b) The force generated by the flagellum on Newtonian fluid at time $t = 0$ (above) and Carreau fluid with $\mu_0/\mu_\infty = 2$, $n = 0.5$ and $De = 0.8$, corresponding to figure 3.15b (below). Arrow lengths are normalised to the largest force at the distal end of the flagellum. (c) A time series of the magnitude of the force profile along the flagellum for Stokes flow, showing the progression of the of the travelling bending wave from proximal to distal end and (d) the magnitude of the force profile of the flagella shown in (b), colours matching, showing a redistribution of force to the distal portion of the flagellum in the case of shear-thinning flow. Force is greatest at the tip of the flagellum.

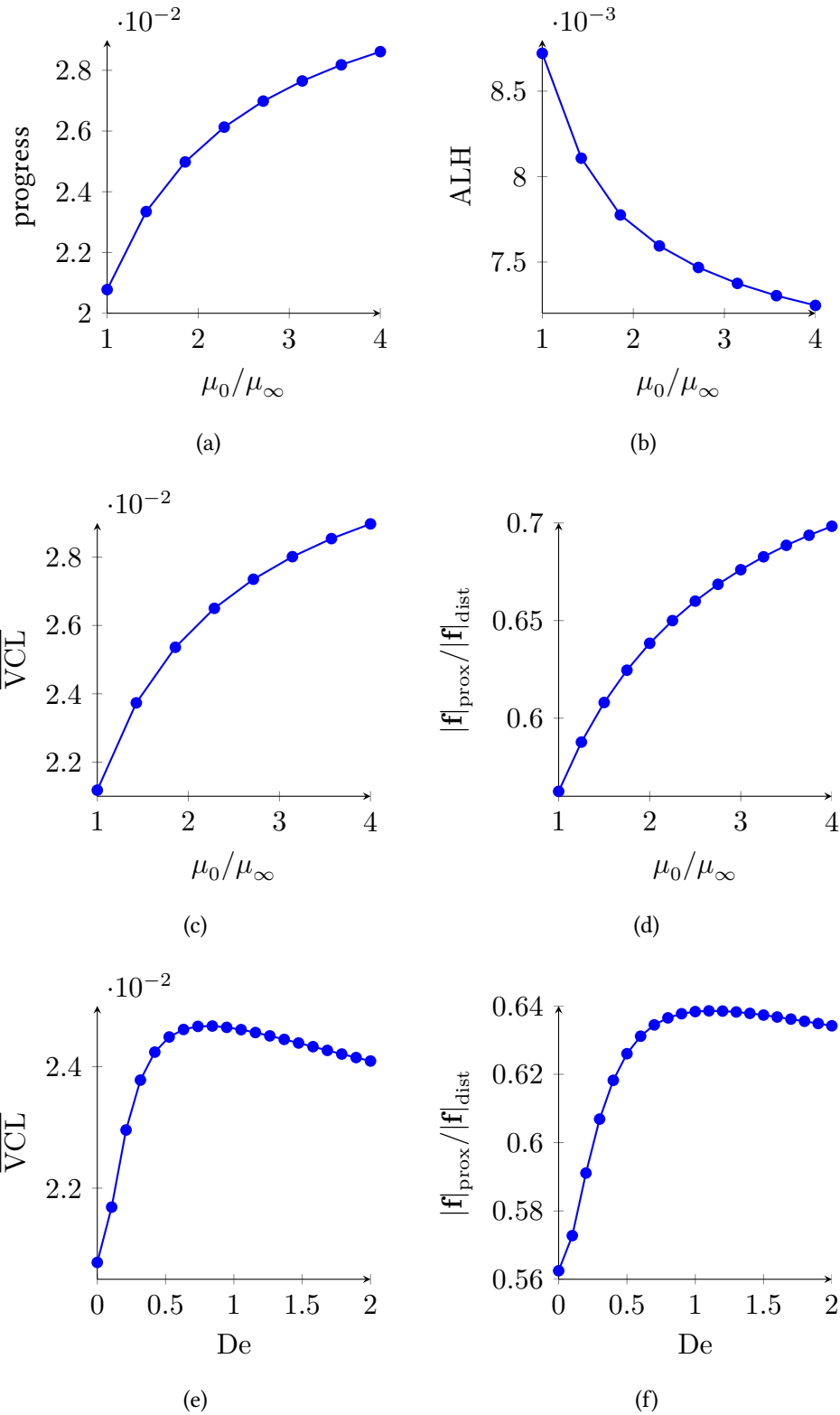


Figure 3.17: Simulation results for the two dimensional sperm like swimmer in Carreau fluid with shear angle prescribed by equation (3.12) for $k = 2.5$ and $A = 0.45\pi$. (a) The progress and (b) the ALH of a two dimensional sperm-like swimmer as a function of the viscosity ratio μ_0/μ_∞ , for $n = 0.5$ and $De = 1$, (c) \overline{VCL} and (d) the ratio of the forces in the proximal and distal portions of the tail at the instant $t = 0$ as a function of μ_0/μ_∞ and (e) \overline{VCL} and (f) the ratio of the forces in the proximal and distal portions of the tail at the instant $t = 0$ as a function of the Deborah number, De with $\mu_0/\mu_\infty = 2$ and $n = 0.5$. Stokes flow corresponds to the cases $\mu_0/\mu_\infty = 1$ and $De = 1$.

a_x	a_y	Eccentricity	Circumference
0.06	0.03	0.832	0.299
0.05	0.04	0.6	0.284
0.0447	0.0447	0	0.281
0.04	0.05	0.6	0.284
0.03	0.06	0.832	0.299

Table 3.2: Elliptical head morphologies of constant area but different eccentricity, corresponding to the data in figure 3.18. The case corresponding to the sperm-like swimmer we first considered is second from the top. These morphologies from top to bottom correspond with dark to light plots.

3.4.2 Effects of changing morphology and kinematics

We will now examine how robust these effects are to changes in cell morphology and kinematics. For all the swimmers we will consider, the case corresponding to the swimmer analysed above will be marked with a dashed line. We will begin by varying the eccentricity of the elliptical head, whilst maintaining its area. We will then consider heads with fixed eccentricity and different area, before varying the wavenumber of the flagellar bending wave. We will consider the trajectories of these swimmers as functions of changing viscosity ratio.

The head shapes we will first consider are given, from elongated in the direction of the flagellum to ‘hammerhead’, in table 3.2. These morphologies are shown, from dark to light, in figure 3.18a. The data presented in the other panels of figure 3.18 are colour matched with the morphology to which they belong. For this set of data, the wavenumber of the flagellar waveform $k = 2.5$, and the area of the head is 0.002π .

The trajectories that these swimmers follow in Stokes flow are shown in figure 3.18b. These show that the principal effect of head elongation is a flattening of the trajectory, which is quantified as a decrease in ALH in figure 3.18d. This leads to a small increase in progress, shown in figure 3.18c. However, it also leads to a decrease in the path length PL of the trajectory, as shown in figure 3.18e. Thus, hammerhead cells swim a greater distance, but for less overall

progress. This is quantified in figure 3.18f, which shows the path straightness STR of the different morphologies. It is interesting to note that, though the morphology of mammalian sperm varies widely across species, hammerhead sperm do not tend to appear in nature; the reduction in STR that this morphology entails may be a reason for this.

Figures 3.18c,d,e,f are plotted as a function of the viscosity ratio μ_0/μ_∞ . This shows that the effect of shear-thinning on these cells is robust to this particular morphological change, within the range of parameters we have considered. The exception is the path length PL, shown in figure 3.18e. For any given morphology, shear-thinning leads to monotonic increases in PL. However, for the most eccentric hammerhead cell ($a_x = 0.03, a_y = 0.06$), these increases are substantially less than occur for the other cells. This is reflected in figure 3.18e, which shows that the path length of this cell's trajectory is exceeded by the less eccentric head with $a_x = 0.04, a_y = 0.05$ for $\mu_0/\mu_\infty > 2$ and by the circular head for $\mu_0/\mu_\infty > 3.5$. This may be due to the increased drag from the larger cell circumference being further enhanced by shear-thinning for hammerhead cells. If this were the case, one might expect that firstly, the cell with ($a_x = 0.04, a_y = 0.05$) would exhibit the same effect and secondly, the elongated cells would exhibit the opposite behaviour. Whilst no further intersections occur in figure 3.18e, it is certainly true that the range of values of the path lengths is smaller for $\mu_0/\mu_\infty = 4$ than for Stokes flow, which lends support to this theory.

We will now consider the effects of varying head size for fixed eccentricity. The head morphologies we will examine are given in table 3.3. The data presented in figure 3.19 are colour matched from dark to light with the smallest to largest head respectively. For this set of data, the wavenumber of the flagellar waveform is $k = 2.5$.

The trajectories that these swimmers follow in Stokes flow are shown in figure 3.19a. This shows that the effects of increasing the area of the head are a decrease in cell progress (figure 3.19b), and a decrease in ALH (figure 3.19c). Thus, the ratio of the cell's forward to side-to-side motion STR is increased (figure 3.19e). This is because the drag on a translating body in two

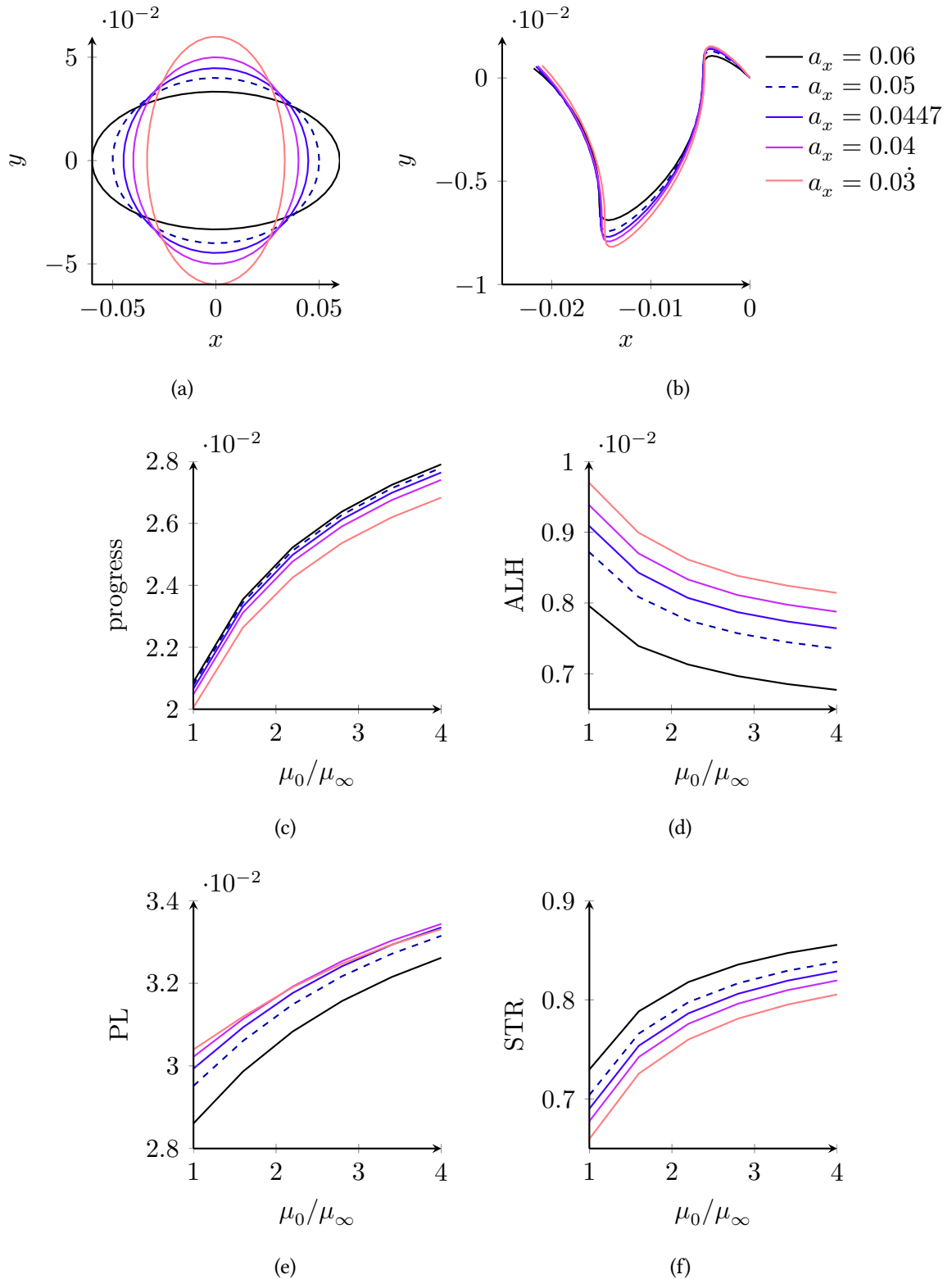


Figure 3.18: (a) The head morphologies listed in table 3.2. Throughout this figure, data are colour matched to correspond with these morphologies, with the case corresponding to the sperm-like swimmer we first considered given by the dashed line. (b) Trajectories of cells with varying head eccentricity through Stokes flow, plotted with equal axis scaling. For $n = 0.5$ and $De = 1$, the effect of varying the viscosity ratio μ_0/μ_∞ on (c) the swimmers' progress, (d) the amplitude of the swimmers' lateral head displacement, (e) the path length of the swimmers' trajectories and (f) the swimmers' path straightness.

a_x	a_y	Area	Circumference
0.045	0.036	0.0016π	0.255
0.05	0.04	0.002π	0.284
0.055	0.044	0.0024π	0.312

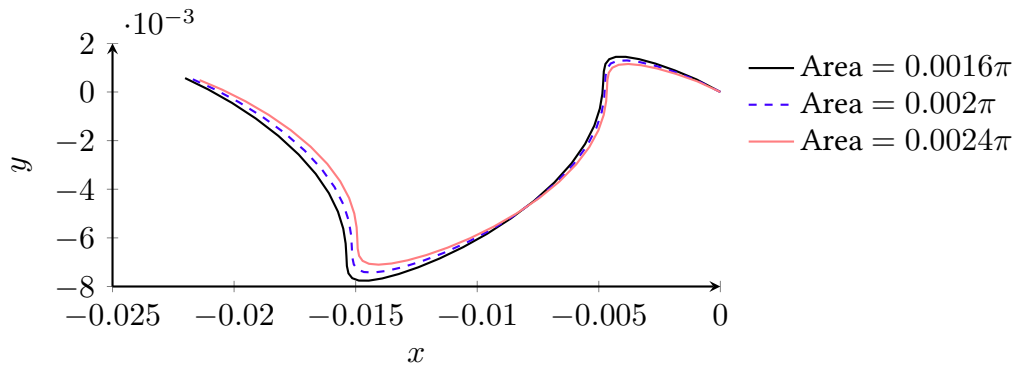
Table 3.3: Elliptical head morphologies of constant eccentricity, but different area, corresponding to the data in figure 3.19. The case corresponding to the sperm-like swimmer we first considered is given by the middle entry. These morphologies, from top to bottom correspond with dark to light plots.

dimensional viscous flow is an increasing function of its circumference. Thus, the larger the head, the more drag on the cell and the more resistance to motion. The decrease in ALH is not sufficient to fully counter the additional resistance to forward motion, and the net result is a decrease in progress as well as path length (figure 3.19d), though this may not be true for morphologies with greater head eccentricity.

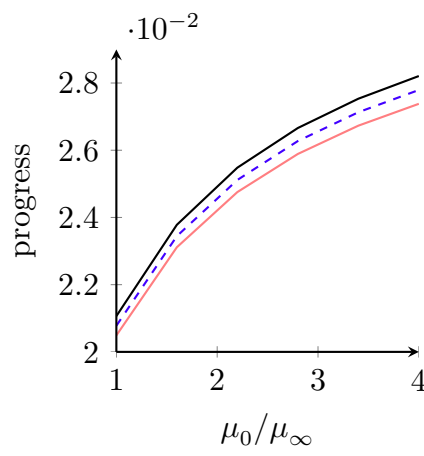
For the morphologies considered, these effects are approximately proportional to the circumference of the cell head for all values of the viscosity ratio. As we observed for varying head eccentricity, shear-thinning improves the swimmer's progress (figure 3.19b) by reducing ALH (figure 3.19c) and increasing VCL, as reflected by increased path length PL (figure 3.19d). This increases the swimmer's path straightness, shown in figure 3.19e.

We will conclude by examining the robustness of the effects of shear-thinning rheology with respect to changes in the wavenumber of the flagellar waveform. The wavenumbers that we will consider are listed, along with an image of the corresponding swimmer, in table 3.4. The data presented in figure 3.20 are colour matched with the swimmer to which they belong. For this set of data, the semi-axes of the cell head are given by $a_x = 0.05$ and $a_y = 0.04$.

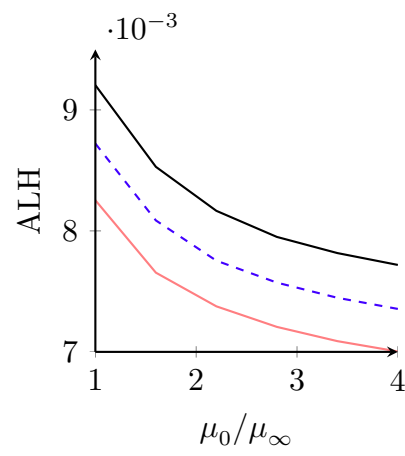
The trajectories that these swimmers follow is shown for the case of Carreau flow with $n = 0.5$, $\mu_0/\mu_\infty = 4$ and $De = 1$ in figure 3.20a. The shapes of the trajectories for $k = 2$ (black) and $k = 3$ (orange) are remarkably similar, though the progress of the swimmer



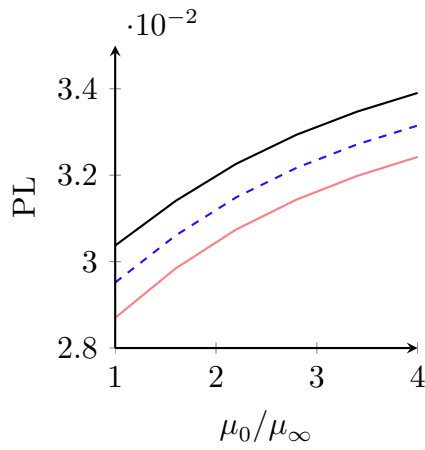
(a)



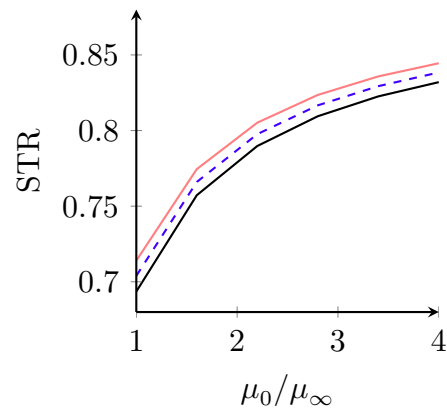
(b)



(c)



(d)



(e)

Figure 3.19: (a) Trajectories of the cells with head morphologies given in table 3.3, swimming in Stokes flow with $n = 0.5$, $\mu_0/\mu_\infty = 4$ and $De = 1$. For $n = 0.5$ and $De = 1$, the effect of varying the viscosity ratio μ_0/μ_∞ on (b) the swimmers' progress, (c) the amplitude of the swimmers' lateral head displacement, (d) the path length of the swimmers' trajectories and (e) the swimmers' path straightness. The case corresponding to the sperm-like swimmer we first considered is given by the dashed line.






Wavenumber	Beat pattern
$k = 2$	
$k = 2.25$	
$k = 2.5$	
$k = 2.75$	
$k = 3$	

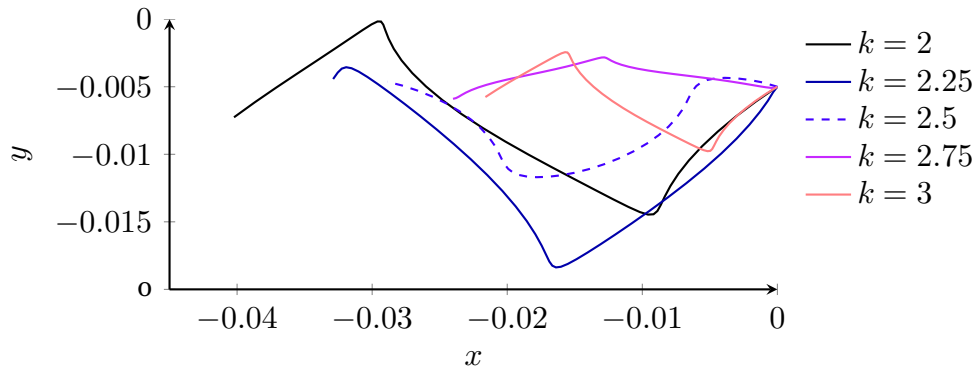
Table 3.4: The wavenumbers and their corresponding beat patterns used to examine the robustness of the effects of shear-thinning to cell kinematics. Data in figure 3.20 are colour matched to their corresponding waveform, with the sperm-like swimmer we first considered, $k = 2.5$, here marked in red, given by the dashed lines. The waveforms are shown in a time-lapse fashion over the same period.

decreases substantially as a function of k as shown in figure 3.20b. Upon examining further wavenumbers, the shape of the trajectory is dependent upon the fractional part of the wavenumber k . The similarity of the trajectories for $k = 2, 3$ is made apparent in figure 3.20e, which shows that the path straightness STR of these waveforms is approximately equal for all values of the viscosity ratio μ_0/μ_∞ considered. The variation in these trajectories demonstrates the profound effect that apparently small changes in cell kinematics can have upon its ability to swim. Although cell progress seems to decrease monotonically as a function of wavenumber, this is not true of ALH, PL or STR.

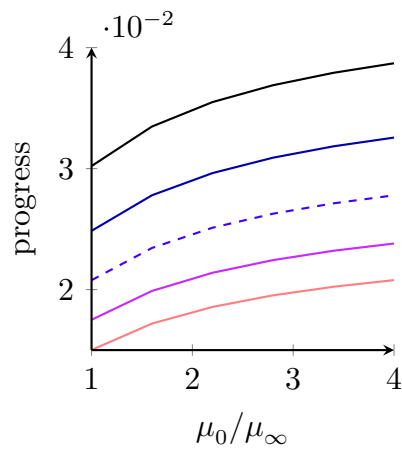
However, the effect of shear-thinning on these trajectories remains consistent. For all waveforms, shear-thinning once more improves progress (figure 3.20b) by reducing side-to-side motion (figure 3.20c) and increasing instantaneous speed VCL, as reflected by increased path length PL (figure 3.20d). This has the effect of increasing the swimmer's path straightness, as quantified in figure 3.20e. However, the extent to which this occurs is a function of the complex interactions between flagellum and fluid, and the gradients of thick to thin fluid that are generated.

In summary, we have shown that for a model of human sperm swimming, the flagellar waveform induces a gradient of thick to thin fluid along the flagellum. This aids progress by flattening the cell's trajectory due to a relative increase in resistance to side-to-side motion of the cell, and by increasing the net propulsive force generated by the flagellum. Thicker fluid in the proximal portion of the flagellum increases the propulsion it generates without appreciably increasing drag, whilst the drag in the distal portion of the tail is reduced by the thinner fluid surrounding it. These effects are robust to reasonable changes in cell morphology and kinematics, though certain morphologies are better able to exploit them.

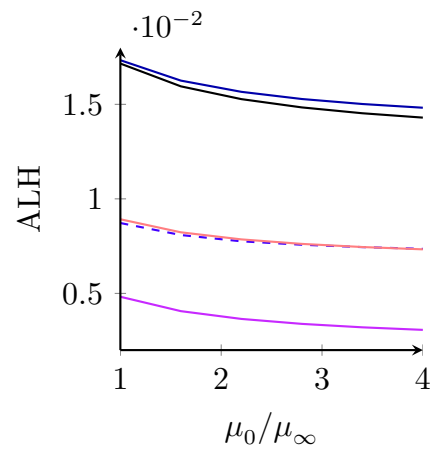
Having examined the effects of shear-thinning rheology on a number of model swimmers, we will now conclude the thesis with a summary of this work and an outline of possible future directions.



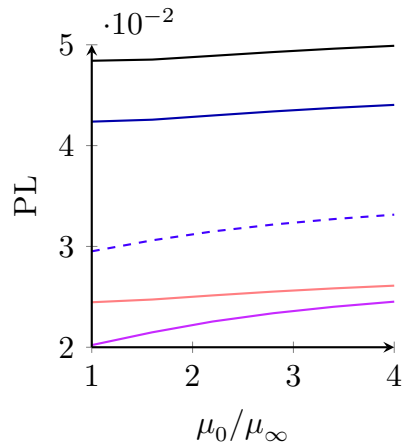
(a)



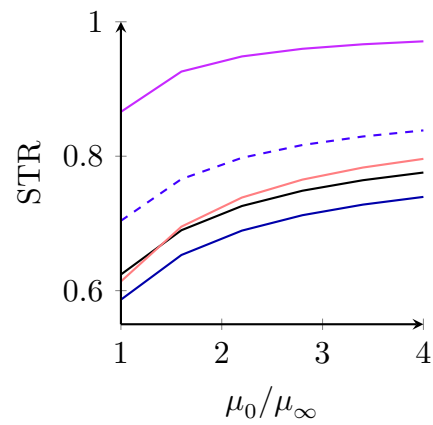
(b)



(c)



(d)



(e)

Figure 3.20: (a) Colour matched trajectories of the cells with waveforms shown in table 3.4, swimming in Carreau flow with $n = 0.5$, $\mu_0/\mu_\infty = 4$ and $De = 1$. For $n = 0.5$ and $De = 1$, the effect of varying the viscosity ratio μ_0/μ_∞ on (b) the swimmers' progress, (c) the amplitude of the swimmers' lateral head displacement, (d) the path length of the swimmers' trajectories and (e) the swimmers' path straightness. The case corresponding to the sperm-like swimmer we first considered is given by the dashed line.

Chapter 4

Conclusions and Future Work

4.1 Summary of methodology

Microscopic swimming has been rich problem in applied mathematics for the last 60 years, leading to the development of numerous techniques for modelling Newtonian and non-Newtonian flows alike. Of recent interest are swimming problems in non-Newtonian fluids, motivated by the complex rheological properties of many biological fluids, such as mucus. These are particularly important in the field of medicine, for instance in fertility research, mucociliary clearance and examining barrier properties of mucus against invasive bacteria. However, nonlinearities in the equations governing non-Newtonian viscous flow make their solution problematic, often requiring linearisation of the equations or the assumption that flagellar beating is small amplitude. While the latter has provided a great number of insights, swimmers exhibiting large amplitude flagellar beating can experience additional effects which change the impact of fluid rheology upon them (Teran et al., 2010). While much recent study has been given to understanding swimmers in viscoelastic fluids, relatively less study has been given to understanding swimmers in shear-thinning fluids, which is a property of human cervical mucus.

Thus, we developed a method for simulating microscopic swimming in nonlinear fluids with shear dependent viscosity for large amplitude swimmer kinematics. Inspired by the method of regularised stokeslets and IBM, the method of femlets utilises a description of the

swimmer as a set of immersed, regularised forces that drive the fluid flow. The finite element projection of the governing fluid equations and the femlet representation of the swimmer is taken, and the flow, the forces that the swimmer exert on the fluid, and the swimming velocities are solved simultaneously. A prescribed function of the swimmer's configuration as a function of time has been used, giving the body frame velocity of the swimmer at the locations of the femlets which are used as constraints for the unknown forces. These conditions are transformed into the lab frame using the a priori unknown swimming translational and angular velocities, which are constrained by the conditions that zero net force and torque act upon the swimmer. The method is now being used in a collaboration with Profs. Kees Weijer and Timothy Newmann at the University of Dundee to examine the force distribution in the developing chick embryo during gastrulation.

A number of extensions to this method that are yet to be completed are possible. Firstly, the method is generalisable to three dimensions by considering a representation of the swimmer by three dimensional immersed forces. This would present a number of technical difficulties. Firstly, a three dimensional description of the geometry and the configuration of the swimmer would be required in order to mesh the domain with DistMesh. Generating this mesh would entail greater numerical cost than the two dimensional case. Additionally, it would be desirable to model flagellated swimmers with two types of femlet; a discretisation of the cell body with regularised disc and of the flagellum with regularised rod cut-off functions, though this would only require an adjustment to the imposition of the zero net force and torque conditions. Finally, there is the numerical cost entailed with solving a larger matrix system, which would necessitate an iterative, perhaps parallelised, solver, such as GMRES. However, these difficulties are all resolvable, and a three dimensional version of the code is currently in development.

A simple extension to the work would be to prescribe beat kinematics with waveforms that have been extracted from high-speed imaging of live cells. Together with rheological

parameters extracted from the medium in which the cell is observed, the method could be used in conjunction with a structural model of the flagellum with external drag prescribed by the femlet forces, to provide data on force generation and efficiency of the flagellum. It would also be desirable to extend the method to allow a description of the swimmer kinematics in terms of prescribed forces, rather than a prescribed configuration. Since the method of femlets simultaneously calculates the fluid force on the swimmer at the location of the femlets along with non-local flow, a discretisation of the solid domain along with boundary conditions is already supplied. Inspired by IBM, a coupled model of the Najafi-Golestanian swimmer where the spheres are linked by Hookean springs and driven by a prescribed oscillatory force is also being developed. This framework could then be extended to incorporate beam mechanics models of the flagellum similar to those summarised in section 1.3.2. Finally, the method may be formulated for viscoelastic fluids, though this has yet to be attempted.

4.2 Summary of findings

The method of femlets was used to analyse the effects of shear-thinning rheology on three qualitatively different swimmers in Carreau fluids. For each swimmer, the impact on swimming speed and trajectory of varying three dimensionless rheological parameters, the viscosity ratio, the power law index, and the Deborah number was examined. It was found that for all swimmers, the effects of shear-thinning rheology may be understood by splitting the swimmer at any time into propulsive and drag-inducing elements, and examining the difference in fluid viscosity surrounding these elements. At any instant, propulsive elements are those which generate a force on the fluid opposite to the direction of instantaneous travel, whereas drag-inducing elements are those which generate force in the direction of instantaneous travel. In general, fluid surrounding propulsive elements is thinner than that surrounding drag-inducing elements, which decreases the magnitude of the propulsive force relative to the drag force,

slowing the swimmer. However, different swimmers through their beat kinematics were able to utilise this phenomenon in order to increase their progress over a full stroke.

The first such swimmers we examined were the class of Najafi-Golestanian swimmers. For the discrete time version of the swimmer, the kinematics was divided into two effective strokes, where the swimmer was travelling in the direction of overall progress, and two recovery strokes, where the swimmer was travelling in the opposite direction in order to readjust its configuration to begin an effective stroke. Over each portion of the stroke, the instantaneous velocity of the swimmer was reduced. However, the velocity was reduced by a greater amount during the recovery strokes, leading to an overall gain in progress. The swimmer operates under the principle that the drag of two spheres in each others' slip stream is less than that of two moving far apart, and shear-thinning enhances this effect. An approximately linear relationship between cell progress and the difference in the average velocity on the surface of the propulsive and drag inducing spheres was found. The apparent linear relationship between the progress of the smooth time version and the logarithm of the viscosity ratio suggests that, for a sphere translating in Carreau fluid, the effective viscosity on the sphere surface might be logarithmically dependent on the viscosity ratio. A generalisation of the Najafi-Golestanian swimmer to N spheres propagating a compressional wave was proposed that utilised the same underlying fluid mechanical phenomena in order to swim. Such swimmers were shown to swim in the direction of the wave they propagate, in contradistinction to monoflagellate pushers. For $N = 5$, this swimmer better exploited shear thinning rheology than for $N = 3$.

For slip-velocity squirmers, both time averaged and travelling wave models were considered. The envelope of thinned fluid surrounding the squirmer was shown to reduce the swimmer's instantaneous velocity. This may be true for any free rigid body exhibiting a slip velocity in shear-thinning fluid. This reduction was associated with enhanced flow decay within the thinned envelope. However, the envelope approach of time-averaging the coordinated action

of many cilia into a surface slip velocity might neglect rheological interactions that occur on the scale of each cilium, and thus it may be desirable in the future to consider squirming models exhibiting small surface deformations, or models incorporating discrete cilia.

Finally, we examined a two dimensional model of human sperm as an archetypal monoflagellate pusher. We found that when exhibiting a beat pattern typical of swimming observed in high viscosity fluids akin to mucus, the flagellar waveform induced a gradient of thick to thin fluid along the flagellum. This aided the cell's progress in two distinct ways. Firstly, the enhanced drag on the cell head reduced the lateral head displacement, flattening the cell's trajectory. Secondly, the thicker fluid in the proximal portion of the flagellum increased the propulsion it generated, without appreciably increasing drag, whilst the drag in the distal portion of the tail was reduced by a similar amount to the propulsion it generated. This led to an overall increase in the propulsion generated by the flagellum, increasing the cell's instantaneous velocity and thereby its total progress. These two effects combined to increase the cells progress, which could be very pronounced for the range of rheological parameters considered, and was found to be robust to reasonable changes in cell morphology and kinematics.

It is important to note that whilst shear-thinning is a property of cervical mucus, it also exhibits elastic properties. Thus, extending the method to incorporate a wider range of rheological behaviours is desirable before extrapolating these conclusions to a physiological setting, for which a full rheological characterisation of human cervical mucus would also be required. An ultimate goal of the research is to couple the method with a one dimensional beam mechanics model of the flagellum. Waveforms extracted from high-speed images of live cells would prescribe the deformation of the swimmer in this model, and calculation of the biologically realistic fluid flow would give the external forces on the cell which, when inputted into an accurate mechanical model of the flagellum, would yield information about force generation, energy transport and power efficiency within the flagellum itself. With better information about the mechanics underlying flagellar motility, treatments such as IVF may one day be

further improved. by providing better sperm selection criteria and insight into normal physiology.

Appendix A

Summary of published and submitted work

A.1 Published work

Montenegro-Johnson, T.D., Smith, A.A., Smith, D.J., Loghin, D. and Blake, J.R (2012). **Modelling the Fluid Mechanics of Cilia and Flagella in Reproduction and Development.** *Eur. Phys. J. E*, 35(10):111

This paper begins with a review on the mechanics of microscopic flow, including several well-established phenomena such as time-reversal symmetry, drag anisotropy of slender bodies, and wall effects, covering some common material with sections 1.1 and 1.2. It then examines two specific problems, symmetry breaking in the mouse embryo and swimming in shear-thinning fluids, in more detail. My contribution entailed writing sections 1,2,4 and 5, and the research comprising section 4.

This section introduced the method of femlets, and used them to examine the effects of shear-thinning rheology on the smooth time Najafi-Golestanian swimmer with which we began section 3.2, and the sperm model for a single set of morphological parameters and a single wavenumber.

Smith, A.A., Montenegro-Johnson, T.D., Smith, D.J., Loghin, D. and Blake, J.R (2012). Symmetry breaking cilia-driven flow in the zebrafish embryo. *J. Fluid Mech.*, 705:26–45.

This paper modelled symmetry breaking flow that arises in a structure known as Kupffer’s vesicle on the developing zebrafish embryo. My contribution to the work was to create a meshing program capable of capturing the complex geometry of Kupffer’s vesicle into a format that could be read by our group’s boundary element code. This involved overcoming several interesting geometrical and topological challenges.

Kupffer’s vesicle may be approximated by a scalene ellipsoid, filled with fluid, into which cilia protrude, driving the flow. I created a program that could distribute cells across the surface at random positions, but with specified cell density which was important to test existing experimental hypotheses. These cells formed a quadratic approximation of the ellipsoid, tessellating it completely. Cilia protruded smoothly from each cell, tilted locally along lines of latitude. These cilia performed a whirling beat, which drove the fluid flow.

We found that a possible mechanism capable of producing the flow field with qualitative and quantitative features closest to those observed experimentally is a combination of posteriorly tilted roof and floor cilia, and dorsally tilted equatorial cilia. This work has subsequently sparked an international collaboration between our group, Dr Susana Lopes and Dr Julyan Cartwright in Lisbon and Granada respectively, resulting in a paper that is to be submitted shortly.

A.2 Unpublished work

Montenegro-Johnson, T.D., Smith, D.J. and Loghin, D. (accepted to *Physics of Fluids*). *Physics of Rheologically-Enhanced Propulsion: Different strokes in General-*

ized Stokes.

In this paper, we present the findings of chapter 3 of this thesis, summarising the observed effects of shear-thinning fluid on the prescribed kinematics model swimmers herein considered. The mechanisms underlying these effects that have been proposed in this thesis are also summarised.

Rua, R.R., Guerrero, A., Sampaio, P., Pintado, P., Smith, A.A., Montenegro-Johnson, T.D., Smith, D.J. and Lopes, S.S. (In preparation).

In this paper, we report the existence of two distinct populations of cilium kinematics in Kupffer's vesicle. Apart from cilia beating at a single frequency, a new type of wobbling kinematics was observed. These different cilium populations are incorporated into our existing computational model of Kupffer's Vesicle and simulations show agreement with flow fields extracted from live imaging.

Bibliography

- Afzelius, B. (1959). Electron microscopy of the sperm tail results obtained with a new fixative. *J. Biophys. Biochem. Cytol.*, 5(2):269–278.
- Ainley, J., Durkin, S., Embid, R., Boindala, P., and Cortez, R. (2008). The method of images for regularized Stokeslets. *J. Comp. Phys.*, 227(9):4600–4616.
- Allgower, E. and Georg, K. (1990). *Numerical continuation methods*, volume 33. Springer-Verlag Berlin.
- Ballowitz, E. (1888). Untersuchungen über die Struktur der Spermatozoen, zugleich ein Beitrag zur Lehre vom feineren Bau der kontraktilen Elemente, Theil 1. Die Spermatozoen der Vöge. *Arch. Mikrosk. Anat.*, 32:401–473.
- Balmforth, N., Coombs, D., and Pachmann, S. (2010). Microelastohydrodynamics of swimming organisms near solid boundaries in complex fluids. *Quart. J. Mech. App. Math.*, 63(3):267–294.
- Baranger, J. and Najib, K. (1990). Analyse numérique des écoulements quasi-Newtoniens dont la viscosité obéit à la loi puissance ou la loi de Carreau. *Numer. Math.*, 58:35–49.
- Bashforth, F. and Adams, J. (1883). *An attempt to test the theories of capillary action: by comparing the theoretical and measured forms of drops of fluid*. Cambridge Univ. Pr.
- Batchelor, G. (1967). *An introduction to fluid mechanics*. Cambridge Univ. Pr.
- Becker, L., Koehler, S., and Stone, H. (2003). On self-propulsion of micro-machines at low Reynolds number: Purcell’s three-link swimmer. *J. Fluid Mech.*, 490(1):15–35.
- Bercovier, M. and Pironneau, O. (1979). Error estimates for finite element method solution of the Stokes problem in the primitive variables. *Numer. Math.*, 33(2):211–224.
- Bird, R. (2002). Transport phenomena. *Appl. Mech. Rev.*, 55:R1.
- Blake, J. and Sleigh, M. (1974). Mechanics of ciliary locomotion. *Biol. Rev.*, 49:85–125.
- Blake, J. R. (1971a). A note on the image system for a Stokeslet in a no-slip boundary. *Proc. Camb. Phil. Soc.*, 70:303–310.

- Blake, J. R. (1971b). A spherical envelope approach to ciliary propulsion. *J. Fluid Mech.*, 46:199–208.
- Böhme, G. and Rubart, L. (1989). Non-Newtonian flow analysis by finite elements. *Fluid Dyn. Res.*, 5(3):147–158.
- Braess, D. (2007). *Finite elements: theory, fast solvers, and applications in solid mechanics*. Cambridge Univ. Pr.
- Brennen, C. and Winet, H. (1977). Fluid mechanics of propulsion by cilia and flagella. *Annu. Rev. Fluid Mech.*, 9:339–398.
- Brokaw, C. (1966). Effects of increased viscosity on the movements of some invertebrate spermatozoa. *J. Exp. Biol.*, 45(1):113.
- Brokaw, C. (1971). Bend propagation by a sliding filament model for flagella. *J. Exp. Biol.*, 55(2):289–304.
- Brokaw, C. (1972). Computer simulation of flagellar movement: I. Demonstration of stable bend propagation and bend initiation by the sliding filament model. *Biophys. J.*, 12(5):564–586.
- Brokaw, C. (1984). Automated methods for estimation of sperm flagellar bending parameters. *Cell Motil.*, 4(6):417–430.
- Brokaw, C. (1994). Control of flagellar bending: a new agenda based on dynein diversity. *Cell Motil. Cyt.*, 28(3):199–204.
- Brokaw, C. (1999). Computer simulation of flagellar movement: Vii. Conventional but functionally different cross-bridge models for inner and outer arm dyneins can explain the effects of outer arm dynein removal. *Cell Motil. Cyt.*, 42(2):134–148.
- Brokaw, C. (2002). Computer simulation of flagellar movement: Viii. Coordination of dynein by local curvature control can generate helical bending waves. *Cell Motil. Cyt.*, 53(2):103–124.
- Brokaw, C. (2009). Simulation of cyclic dynein-driven sliding, splitting, and reassociation in an outer doublet pair. *Biophys. J.*, 97(11):2939–2947.
- Camalet, S. and Jülicher, F. (2000). Generic aspects of axonemal beating. *New J. Phys.*, 2:24.
- Carreau, P. (1968). *Rheological equations from molecular network theories*. Univ. Wisconsin–Madison.
- Childress, S. (1981). *Mechanics of swimming and flying*. Cambridge Univ. Pr.
- Chorin, A. (1968). Numerical solution of the Navier-Stokes equations. *Math. Comp.*, 22(104):745–762.

- Chwang, A. and Wu, T. (1971). A note on the helical movement of micro-organisms. *Proc. Roy. Soc. Lond. B*, 178:327–346.
- Chwang, A. and Wu, T. (1975). Hydromechanics of low-Reynolds-number flow. Part 2. Singularity method for Stokes flows. *J. Fluid Mech.*, 67:787.
- Ciarlet, P. (1978). *The finite element method for elliptic problems*, volume 4. North Holland.
- Cisneros, L., Cortez, R., Dombrowski, C., Goldstein, R., and Kessler, J. (2007). Fluid dynamics of self-propelled microorganisms, from individuals to concentrated populations. *Exp. Fluids*, 43(5):737–753.
- Clift, A. (1945). Observations on certain rheological properties of human cervical secretion. *Proc. Royal Soc. Med.*, 39(1):1.
- Corless, R., Gonnet, G., Hare, D., Jeffrey, D., and Knuth, D. (1996). On the Lambert W function. *Adv. Comp. Math.*, 5(1):329–359.
- Cortez, R. (2001). The method of regularized Stokeslets. *SIAM J. Sci. Comput.*, 23:1204–1225.
- Crouzeix, M. and Raviart, P. (1973). Conforming and nonconforming finite element methods for solving the stationary stokes equations. *Revue française d'automatique, informatique, recherche opérationnelle*.
- Crowdy, D. (2011). Treadmilling swimmers near a no-slip wall at low reynolds number. *Int. J. Non-Lin. Mech.*, 46:577–585.
- Cywiak, M., Servín, M., and Mendoza Santoyo, F. (2001). Wave-front propagation by Gaussian superposition. *Optics Comm.*, 195(5):351–359.
- Davis, A. and Crowdy, D. (2012). Stresslet asymptotics for a treadmilling swimmer near a two-dimensional corner: hydrodynamic bound states. *Proc. Roy. Soc. Lond. A*.
- De Vries, G. and Norrie, D. (1971). The application of the finite-element technique to potential flow problems. *J. App. Mech.*, 38:798.
- Delaunay, B. (1934). Sur la sphere vide. *Izv. Akad. Nauk SSSR, Otdelenie Matematicheskii i Estestvennyka Nauk*, 7:793–800.
- Denissenko, P., Kantsler, V., Smith, D., and Kirkman-Brown, J. (2012). Human spermatozoa migration in microchannels reveals boundary-following navigation. *Proc. Natl Acad. Sci.*, 109(21):8007–8010.
- Dentler, W. (1987). Cilia and flagella. *Int. Rev. Cytol. Suppl*, 17:391–456.
- Dillon, R. and Fauci, L. (2000). An integrative model of internal axoneme mechanics and external fluid dynamics in ciliary beating. *J. Theor. Biol.*, 207:415–430.

- Dillon, R., Fauci, L., Omoto, C., and Yang, X. (2007). Fluid dynamic models of flagellar and ciliary beating. *Ann. New York Acad. Sci.*, 1101:494–505.
- Drescher, K., Dunkel, J., Cisneros, L. H., Ganguly, S., and Goldstein, R. E. (2011). Fluid dynamics and noise in bacterial cell-cell and cell-surface scattering. *Proc. Natl. Acad. Sci. USA*, 108(27):10940–10945.
- Drescher, K., Goldstein, R. E., Michel, N., Polin, M., and Tuval, I. (2010). Direct measurement of the flow field around swimming microorganisms. *Phys. Rev. Lett.*, 105(16):168101.
- Dresdner, R. D. and Katz, D. F. (1981). Relationships of mammalian sperm motility and morphology to hydrodynamic aspects of cell function. *Biol. Reprod.*, 25(5):920.
- Elias, R., Coutinho, A., and Martins, M. (2006). Inexact Newton-type methods for the solution of steady incompressible viscoplastic flows with the SUPG/PSPG finite element formulation. *Comp. Meth. App. Mech. Eng.*, 195(23-24):3145–3167.
- Ellwood, K., Georgiou, G., Papanastasiou, T., and Wilkes, J. (1990). Laminar jets of bingham-plastic liquids. *J. Rheol.*, 34(6):787–812.
- Engelmann, W. (1868). *Über die flimmerbewegung*. Engelmann.
- Ewoldt, R., Hosoi, A., and McKinley, G. (2008). New measures for characterizing nonlinear viscoelasticity in large amplitude oscillatory shear. *J. Rheol.*, 52(6):1427–1458.
- Fauci, L. (1990). Interaction of oscillating filaments: a computational study. *J. Comp. Phys.*, 86(2):294–313.
- Fauci, L. (1996). A computational model of the fluid dynamics of undulatory and flagellar swimming. *Amer. Zool.*, 36(6):599–607.
- Fauci, L. and Dillon, R. (2006). Biofluidmechanics of reproduction. *Annu. Rev. Fluid Mech.*, 38:371–394.
- Fauci, L. and McDonald, A. (1995). Sperm motility in the presence of boundaries. *Bull. Math. Biol.*, 57:679–699.
- Fauci, L. and Peskin, C. (1988). A computational model of aquatic animal locomotion. *J. Comp. Phys.*, 77:85–108.
- Fawcett, D. (1975). The mammalian spermatozoon. *Dev. Biol.*, 44(2):394.
- Fawcett, D. W. (1954). The study of epithelial cilia and sperm flagella with the electron microscope. *The Laryngoscope*, 64(7):557–567.
- Ford, W. (2006). Glycolysis and sperm motility: does a spoonful of sugar help the flagellum go round? *Human Reprod. Upd.*, 12(3):269–274.

- Fortin, M. (1975). Utilisation de la méthode des éléments finis en mécanique des fluides, I. *Calcolo*, 12(4):405–441.
- Fortin, M. and Thomasset, F. (1979). Mixed finite-element methods for incompressible flow problems. *J. Comp. Phys.*, 31(1):113 – 145.
- Friedrich, B., Riedel-Kruse, I., Howard, J., and Jülicher, F. (2010). High-precision tracking of sperm swimming fine structure provides strong test of Resistive Force Theory. *J. Exp. Biol.*, 213(8):1226–1234.
- Frigaard, I., Howison, S., and Sobey, I. (1994). On the stability of Poiseuille flow of a Bingham fluid. *J. Fluid Mech.*, 263:133–150.
- Fu, H., Wolgemuth, C., and Powers, T. (2009). Swimming speeds of filaments in nonlinearly viscoelastic fluids. *Phys. Fluids*, 21:033102–033112.
- Fulford, G., Katz, D., and Powell, R. (1998). Swimming of spermatozoa in a linear viscoelastic fluid. *Biorheol.*, 35:295–310.
- Fung, Y. and Tong, P. (2001). *Classical and computational solid mechanics*, volume 1. World Scientific Pub Co Inc.
- Gadêlha, H., Gaffney, E., Smith, D., and Kirkman-Brown, J. (2010). Nonlinear instability in flagellar dynamics: a novel modulation mechanism in sperm migration? *J. R. Soc. Interface*, 7:1689–1697.
- Gaffney, E., Gadêlha, H., Smith, D., Blake, J., and Kirkman-Brown, J. (2011). Mammalian sperm motility: observation and theory. *Annu. Rev. Fluid Mech.*, 43:501–528.
- Gibbons, I. (1981). Cilia and flagella of eukaryotes. *J. Cell Biol.*, 91(3):107s–124s.
- Gillies, E., Cannon, R., Green, R., and Pacey, A. (2009). Hydrodynamic propulsion of human sperm. *J. Fluid Mech.*, 625:444–473.
- Goldstein, R., Powers, T., and Wiggins, C. (1998). Viscous nonlinear dynamics of twist and writhe. *Phys. Rev. Lett.*, 80(23):5232–5235.
- Gray, J. (1928). *Ciliary movement*. Cambridge Comparative Physiology. Cambridge Univ. Pr.
- Gray, J. and Hancock, G. J. (1955). The propulsion of sea-urchin spermatozoa. *J. Exp. Biol.*, 32:802–814.
- Gueron, S., Levit-Gurevich, K., Liron, N., and Blum, J. (1997). Cilia internal mechanism and metachronal coordination as the result of hydrodynamical coupling. *Proc. Natl. Acad. Sci.*, 94(12):6001.
- Hancock, G. J. (1953). The self-propulsion of microscopic organisms through liquids. *Proc. Roy. Soc. Lond. A*, 217:96–121.

- Higdon, J. J. L. (1979). A hydrodynamic analysis of flagellar propulsion. *J. Fluid Mech.*, 90:685–711.
- Hilfinger, A., Chattopadhyay, A., and Jülicher, F. (2009). Nonlinear dynamics of cilia and flagella. *Phys. Rev. E*, 79(5):051918.
- Hines, M. and Blum, J. (1978). Bend propagation in flagella. I. Derivation of equations of motion and their simulation. *Biophys. J.*, 23(1):41–57.
- Hines, M. and Blum, J. (1979). Bend propagation in flagella. II. Incorporation of dynein cross-bridge kinetics into the equations of motion. *Biophys. J.*, 25(3):421–441.
- Ho-Le, K. (1988). Finite element mesh generation methods: a review and classification. *Comp. Aid. Des.*, 20(1):27–38.
- Hosoi, A. and Lauga, E. (2010). Mechanical aspects of biological locomotion. *Exp. Mech.*, 50(9):1259–1261.
- Human Fertilisation and Embryology Authority (2011). Fertility treatment in 2010-trends and figures.
- Iserles, A. (2009). *A first course in the numerical analysis of differential equations*, volume 44. Cambridge Univ. Press.
- Ishikawa, T., Simmonds, M., and Pedley, T. (2006). Hydrodynamic interaction of two swimming model micro-organisms. *J. Fluid Mech.*, 568:119–160.
- Ishimoto, K. and Yamada, M. (2011). A rigorous proof of the scallop theorem and a finite mass effect of a microswimmer. *Arxiv preprint arXiv:1107.5938*.
- Johnson, R. (1980). An improved Slender-Body Theory for Stokes flow. *J. Fluid Mech.*, 99(2):411–431.
- Johnson, R. and Brokaw, C. (1979). Flagellar hydrodynamics. A comparison between Resistive-Force Theory and Slender-Body Theory. *Biophys. J.*, 25(1):113–127.
- Karagiannis, A., Mavridis, H., Hrymak, A., and Vlachopoulos, J. (2005). A finite element convergence study for shear-thinning flow problems. *Intl. J. Num. Meth. Fluids*, 8(2):123–138.
- Katz, D., Drobnis, E., and Overstreet, J. (1989). Factors regulating mammalian sperm migration through the female reproductive tract and oocyte vestments. *Gamete Res.*, 22(4):443–469.
- Katz, D., Mills, R., and Pritchett, T. (1978). The movement of human spermatozoa in cervical mucus. *J. Reprod. Fert.*, 53(2):259.
- Katz, D., Overstreet, J., and Hanson, F. (1980). A new quantitative test for sperm penetration into cervical mucus. *Fertil. Steril.*, 33:179.

- Lai, S., O’Hanlon, D., Harrold, S., Man, S., Wang, Y., Cone, R., and Hanes, J. (2007). Rapid transport of large polymeric nanoparticles in fresh undiluted human mucus. *Proc. Natl. Acad. Sci.*, 104(5):1482.
- Lai, S., Wang, Y., Wirtz, D., and Hanes, J. (2009). Micro-and macrorheology of mucus. *Adv Drug Del. Rev.*, 61(2):86–100.
- Lauga, E. (2007a). Continuous breakdown of Purcell’s scallop theorem with inertia. *Phys. Fluids*, 19:061703.
- Lauga, E. (2007b). Propulsion in a viscoelastic fluid. *Phys. Fluids*, 19:083104–083117.
- Lauga, E. (2009). Life at high Deborah number. *Europhys. Lett.*, 86:64001.
- Lauga, E. (2011). Life around the Scallop theorem. *Soft Matter*, 7(7):3060–3065.
- Lauga, E., DiLuzio, W., Whitesides, G., and Stone, H. (2006). Swimming in circles: motion of bacteria near solid boundaries. *Biophys. J.*, 90(2):400–412.
- Lighthill, M. (1952). On the squirming motion of nearly spherical deformable bodies through liquids at very small Reynolds numbers. *Commun. Pure Appl. Math.*, 5:109–118.
- Lighthill, M. (1975). *Mathematical biofluidynamics*. Regional conference series in applied mathematics. Society for Industrial and Applied Mathematics.
- Lighthill, M. (1976). Flagellar hydrodynamics: the John von Neumann lecture, 1975. *SIAM Rev.*, pages 161–230.
- Lin, Z., Thiffeault, J., and Childress, S. (2011). Stirring by squirmers. *J. Fluid Mech.*, 669:167–177.
- Lindemann, C. (1994a). A “geometric clutch” hypothesis to explain oscillations of the axoneme of cilia and flagella. *J. Theor. Biol.*, 168(2):175–190.
- Lindemann, C. (1994b). A model of flagellar and ciliary functioning which uses the forces transverse to the axoneme as the regulator of dynein activation. *Cell Motil. Cyt.*, 29(2):141–154.
- Lindemann, C. (1996). Functional significance of the outer dense fibers of mammalian sperm examined by computer simulations with the geometric clutch model. *Cell Motil. Cyt.*, 34(4):258–270.
- Lindemann, C. (2002). Geometric clutch model version 3: The role of the inner and outer arm dyneins in the ciliary beat. *Cell Motil. Cyt.*, 52(4):242–254.
- Lindemann, C. (2004). Testing the geometric clutch hypothesis. *Biol. Cell*, 96(9):681–690.
- Lindemann, C. (2009). Heart of the beat (the flagellar beat, that is). *Biophys. J.*, 97(11):2865.
- Liron, N. and Mochon, S. (1976). Stokes flow for a stokeslet between two parallel flat plates. *J. Eng. Math.*, 10(4):287–303.

- Machin, K. (1958). Wave propagation along flagella. *J. Exp. Biol.*, 35(4):796–806.
- Manton, I. and Clarke, B. (1952). An electron microscope study of the spermatozoid of sphagnum. *J. Exp. Biol.*, 3(3):265–275.
- Michelin, S. and Lauga, E. (2011). Optimal feeding is optimal swimming for all Péclet numbers. *Phys. Fluids*, 23:101901–101914.
- Mills, R. and Katz, D. (1978). A flat capillary tube system for assessment of sperm movement in cervical mucus. *Fertil. Steril.*, 29:43–47.
- Mitsoulis, E. (2007). Flows of viscoplastic materials: models and computations. *Rheol. Rev.*, 135:178.
- Mittal, R. and Iaccarino, G. (2005). Immersed boundary methods. *Annu. Rev. Fluid Mech.*, 37:239–261.
- Montenegro-Johnson, T., Smith, A., Smith, D., Loghin, D., and Blake, J. (2012). Modelling the fluid mechanics of cilia and flagella in reproduction and development. *Eur. Phys. J. E*, 35(10):111.
- Montenegro-Johnson, T., Smith, D., and Loghin, D. (2013). Different strokes in generalised Stokes. *In preparation*.
- Mortimer, S. (1997). A critical review of the physiological importance and analysis of sperm movement in mammals. *Human Reprod. Upd.*, 3:403–439.
- Najafi, A. and Golestanian, R. (2004). Simple swimmer at low Reynolds number: three linked spheres. *Phys. Rev. E*, 69:062901.
- Nicastro, D., Schwartz, C., Pierson, J., Gaudette, R., Porter, M., and McIntosh, J. (2006). The molecular architecture of axonemes revealed by cryoelectron tomography. *Science*, 313(5789):944.
- Nonaka, S., Tanaka, Y., Okada, Y., Takeda, S., Harada, A., Kanai, Y., Kido, M., and Hirokawa, N. (1998). Randomization of left-right asymmetry due to loss of nodal cilia generating leftward flow of extraembryonic fluid in mice lacking KIF3B motor protein. *Cell*, 95(6):829–837.
- Oden, J. (1973). The finite element method in fluid mechanics. *Lectures on finite element methods in continuum mechanics*, pages 151–186.
- Oldroyd, J. (1958). Non-Newtonian effects in steady motion of some idealized elastico-viscous liquids. *Proc. Roy. Soc. Lond. A*, 245(1241):278–297.
- Olmsted, S., Meyn, L., Rohan, L., and Hillier, S. (2003). Glycosidase and proteinase activity of anaerobic gram-negative bacteria isolated from women with bacterial vaginosis. *Sex. Trans. Dis.*, 30(3):257–261.

- Olmsted, S., Padgett, J., Yudin, A., Whaley, K., Moench, T., and Cone, R. (2001). Diffusion of macromolecules and virus-like particles in human cervical mucus. *Biophys J.*, 81(4):1930–1937.
- O'Malley, S. and Bees, M. (2012). The Orientation of Swimming Biflagellates in Shear Flows. *Bull. Math. Biol.*, 74(1):232–255.
- Pak, O. S. and Lauga, E. (2011). Extensibility enables locomotion under isotropic drag. *Phys. Fluids*, 23:081702–081706.
- Papanastasiou, T. (1987). Flows of materials with yield. *J. Rheol.*, 31:385.
- Parker, G. H. (1905). The movements of the swimming-plates in Ctenophores, with reference to the theories of ciliary metachronism. *J. Exp. Zool.*, 2(3):407–423.
- Persson, P. and Strang, G. (2004). A simple mesh generator in Matlab. *SIAM Rev.*, 46(2):329–345.
- Peskin, C. (1972). Flow patterns around heart valves: a numerical method. *J. Comp. Phys.*, 10:252–271.
- Peskin, C. (1977). Numerical analysis of blood flow in the heart. *J. Comp. Phys.*, 25(3):220–252.
- Phan-Thien, N. (2002). *Understanding viscoelasticity: basics of rheology*. Springer Verlag.
- Phan-Thien, N., Tran-Cong, T., and Ramia, M. (1987). A boundary-element analysis of flagellar propulsion. *J. Fluid Mech.*, 184:533–549.
- Phillips, D. (1970). Insect sperm: their structure and morphogenesis. *J. Cell Biol.*, 44(2):243.
- Purcell, E. (1977). Life at low Reynolds number. *Amer. J. Phys.*, 45:3–11.
- Ramia, M., Tullock, D., and Phan-Thien, N. (1993). The role of hydrodynamic interaction in the locomotion of microorganisms. *Biophys. J.*, 65(2):755–778.
- Riedel-Kruse, I., Hilfinger, A., Howard, J., and Jülicher, F. (2007). How molecular motors shape the flagellar beat. *HFSP Journal*, 1:192–208.
- Rothschild, L. (1963). Non-random distribution of bull spermatozoa in a drop of sperm suspension. *Nature*, 198:1221–1222.
- Satir, P. (1965). Studies on cilia: II. Examination of the distal region of the ciliary shaft and the role of the filaments in motility. *J. Cell Biol.*, 26(3):805–834.
- Sharpey, W. (1835). *Cilia*. In: Todd R.B., editor. *Cyclopaedia of Anatomy and Physiology*. Longman, Brown, Green, Longman and Roberts, London.
- Shen, X. and Arratia, P. (2011). Undulatory swimming in viscoelastic fluids. *Phys. Rev. Lett.*, 106(20):208101.

- Shen, X., Gagnon, D., and Arratia, P. (2012). Undulatory swimming in shear-thinning fluids. *Bull. Amer. Phys. Soc.*, 57.
- Shum, H., Gaffney, E., and Smith, D. (2010). Modelling bacterial behaviour close to a no-slip plane boundary: the influence of bacterial geometry. *Proc. Roy. Soc. Lond. A*, 466(2118):1725.
- Sleigh, M. A., Blake, J. R., and Liron, N. (1988). The propulsion of mucus by cilia. *Amer. Rev. Respir. Dis.*, 137(3):726–741.
- Smith, A. A., Johnson, T. D., J., S. D., and Blake, J. R. (2012). Symmetry-breaking cilia-driven flow in the zebrafish embryo. *J. Fluid Mech.*, 705:26–45.
- Smith, D., Gaffney, E., and Blake, J. (2009a). Mathematical modelling of cilia-driven transport of biological fluids. *Proc. Roy. Soc. Lond. A*, 465:2417–2439.
- Smith, D., Smith, A., and Blake, J. (2011). Mathematical embryology: the fluid mechanics of nodal cilia. *J. Eng. Math.*, 70(1):255–279.
- Smith, D. J. and Blake, J. R. (2009). Surface accumulation of spermatozoa: A fluid dynamic phenomenon. *Math. Sci.*, 34(2):74–87.
- Smith, D. J., Gaffney, E. A., and Blake, J. R. (2007). Discrete cilia modelling with singularity distributions: application to the embryonic node and the airway surface liquid. *Bull. Math. Biol.*, 69(5):1477–1510.
- Smith, D. J., Gaffney, E. A., Blake, J. R., and Kirkman-Brown, J. C. (2009b). Human sperm accumulation near surfaces: a simulation study. *J. Fluid Mech.*, 621:289–320.
- Smith, D. J., Gaffney, E. A., Gadêlha, H., Kapur, N., and Kirkman-Brown, J. C. (2009c). Bend propagation in the flagella of migrating human sperm, and its modulation by viscosity. *Cell Motil. Cyt.*, 66:220–236.
- Strang, G. and Fix, G. (1988). *An analysis of the finite element method*. Wellesley-Cambridge Pr.
- Suarez, S. and Ho, H. (2003). Hyperactivated motility in sperm. *Reprod. Dom. Animals*, 38(2):119–124.
- Tam, D. and Hosoi, A. (2007). Optimal stroke patterns for Purcell’s three-link swimmer. *Phys. Rev. Lett.*, 98(6):68105.
- Taylor, C. and Hood, P. (1973). A numerical solution of the Navier-Stokes equations using the finite element technique. *Comp. Fluids*, 1:73–100.
- Taylor, G. (1967). Film notes for low-Reynolds number flows. *National Committee for Fluid Mechanics*.

- Taylor, G. I. (1951). Analysis of the swimming of microscopic organisms. *Proc. Roy. Soc. Lond. A*, 209:447–461.
- Teran, J., Fauci, L., and Shelley, M. (2010). Viscoelastic fluid response can increase the speed and efficiency of a free swimmer. *Phys. Rev. Lett.*, 104:38101–38105.
- Tytell, E., Hsu, C., Williams, T., Cohen, A., and Fauci, L. (2010). Interactions between internal forces, body stiffness, and fluid environment in a neuromechanical model of lamprey swimming. *Proc. Natl Acad. Sci. Amer.*, 107:19832–19837.
- Vernon, G. and Woolley, D. (2004). Basal sliding and the mechanics of oscillation in a mammalian sperm flagellum. *Biophys. J.*, 87(6):3934–3944.
- Verworn, M. (1891). Studien zur physiologie der flimmerbewegung. *Pflügers Archiv Eur. J. Physiol.*, 48(1):149–180.
- Vilfan, A. and Jülicher, F. (2006). Hydrodynamic flow patterns and synchronization of beating cilia. *Phys. Rev. Lett.*, 96(5):58102.
- Vladimirov, V. (2012). On self-propulsion of n -sphere micro-robot. *arXiv preprint arXiv:1209.0171*.
- Woolley, D. and Vernon, G. (2001). A study of helical and planar waves on sea urchin sperm flagella, with a theory of how they are generated. *J. Exp. Biol.*, 204(7):1333–1345.
- Yang, X., Dillon, R., and Fauci, L. (2008). An integrative computational model of multiciliary beating. *Bull. Math. Biol.*, 70:1192–1215.
- You, Z., Huilgol, R., and Mitsoulis, E. (2008). Application of the Lambert W function to steady shearing flows of the Papanastasiou model. *Intl J. Eng. Sci.*, 46(8):799–808.
- Youngren, G. and Acrivos, A. (1975). Stokes flow past a particle of arbitrary shape: a numerical method of solution. *J. Fluid Mech.*, 69:377–403.
- Zhu, L., Lauga, E., and Brandt, L. (2012). Self-propulsion in viscoelastic fluids: Pushers vs. pullers. *Phys. Fluids*, 24(5):051902–051919.
- Zienkiewicz, O. and Cheung, Y. (1965). Finite elements in the solution of field problems. *The Engineer*, 220(5722):507–510.
- Zienkiewicz, O. and Taylor, R. (1989). The finite element method, Vol. 1. Basic Formulation and Linear Problems. 2.